



NUMERICAL STUDY OF WAVE RUN-UP ON A FIXED SURFACE-PIERCING
CYLINDER IN NON-BREAKING WAVES

Mohammad Mohseni

Tese de Doutorado apresentada ao Programa de Pós-graduação em Engenharia Oceânica, COPPE, da Universidade Federal do Rio de Janeiro, como parte dos requisitos necessários à obtenção do título de Doutor em Engenharia Oceânica.

Orientadores: Sergio Hamilton Sphaier

Paulo de Tarso Themistocles

Esperança

Rio de Janeiro

Agosto de 2018

NUMERICAL STUDY OF WAVE RUN-UP ON A FIXED SURFACE-PIERCING
CYLINDER IN NON-BREAKING WAVES

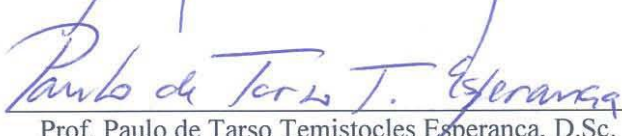
Mohammad Mohseni

TESE SUBMETIDA AO CORPO DOCENTE DO INSTITUTO ALBERTO LUIZ COIMBRA
DE PÓS-GRADUAÇÃO E PESQUISA DE ENGENHARIA (COPPE) DA UNIVERSIDADE
FEDERAL DO RIO DE JANEIRO COMO PARTE DOS REQUISITOS NECESSÁRIOS
PARA A OBTENÇÃO DO GRAU DE DOUTOR EM CIÊNCIAS EM ENGENHARIA
OCEÂNICA.

Examinada por:



Prof. Sergio Hamilton Sphaier, Dr.-Ing.



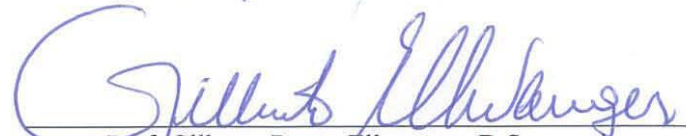
Prof. Paulo de Tarso Temistocles Esperança, D.Sc.



Prof. Carlos Antônio Levi da Conceição, Ph.D.



Prof. Afonso de Moraes Paiva, Ph.D.



Prof. Gilberto Bruno Ellwanger, D.Sc.



Prof. Aristeu da Silveira Neto, D.Sc.

RIO DE JANEIRO, RJ - BRASIL

AGOSTO DE 2018

Mohseni, Mohammad

Numerical study of wave run-up on a fixed surface-piercing cylinder in non-breaking waves/ Mohammad Mohseni. – Rio de Janeiro: UFRJ/COPPE, 2018.

XVII, 103 p.: il.; 29,7 cm.

Orientador: Sergio Hamilton Sphaier

Paulo de Tarso Themistocles Esperança

Tese (doutorado) – UFRJ/ COPPE/ Programa de Engenharia Oceânica, 2018.

Referências Bibliográficas: p. 99-103.

1. Wave run-up. 2. Nonlinear wave–structure interactions. 3. OpenFOAM. 4. Non-breaking waves. I. Sphaier, Sergio Hamilton *et al.* II. Universidade Federal do Rio de Janeiro, COPPE, Programa de Engenharia Oceânica. III. Título.

*To my dear family, who always
picked me up and encourage me
to go on every adventure,
especially this one.*

Acknowledgement

After an intense but very interesting research period at Federal University of Rio de Janeiro, it is time to finish my Ph.D. thesis. This thesis would not have been possible without some people whom I want to thank. Firstly, I would like to thank my two supervisors for their support. My respect and gratitude go to prof. Sergio Hamilton Sphaier, who is more than a supervisor and has been both a friend and a mentor. His insights in hydrodynamic and also his patience, motivation were a big help for me to bring my Ph.D. research to a higher level. Also, a big thank to my second supervisor prof. Paulo de Tarso Themistocles Esperança, for his financial support during the research in LabOceano/COPPE/UFRJ. Secondly, I'm also thankful to all my colleagues, the professors and the entire staff of the Ocean Engineering Program of the Federal University of Rio de Janeiro. I would like to acknowledge Agência Nacional de Petróleo- ANP/PRH03 and Brazilian National Council for the Improvement of Higher Education (CAPES), for all of their financial support during my Ph.D. period. I also take this opportunity to record my sincere gratitude to the support of the Advanced Nucleus of High-Performance Computing (NACAD) from COPPE, Federal University of Rio de Janeiro UFRJ, Brazil.

Mohammad Mohseni

August 2018

Resumo da Tese apresentada à COPPE/UFRJ como parte dos requisitos necessários para a obtenção do grau de Doutor em Ciências (D.Sc.)

ESTUDO NUMÉRICO DO WAVE RUN-UP EM TORNO DE UM CILINDRO FIXO QUE PERFURA A SUPERFÍCIE LIVRE EM ONDAS NÃO QUEBRADAS

Mohammad Mohseni

Agosto /2018

Orientadores: Sergio Hamilton Sphaier

Paulo de Tarso Themistocles Esperança

Programa: Engenharia Oceânica

Na interação onda-estrutura, o wave run-up é um fenômeno importante a ser considerado no projeto de estruturas offshore. Uma maior compreensão da física desse fenômeno não-linear é necessária. O presente estudo está, principalmente, focado na simulação hidrodinâmica da onda e procura avaliar a importância dos tipos de espalhamento das ondas identificados por Swan-et al. [2005], nas ondas de borda progressivas laterais e na amplificação das elevações das ondas em torno de um único cilindro circular fixo. A física do problema inclui a interação do cilindro que atravessa a superfície livre com ondas gravitacionais de superfície incidentes que estão se propagando sobre um fundo plano em um domínio ilimitado. A análise é realizada numericamente usando CFD para resolver a equação de Navier-Stokes e na teoria de escoamento potencial. Os resultados numéricos são comparados com os dados experimentais apresentados em ITTC (OEC), [2013]. Inicialmente, investiga-se a importância do espalhamento da onda incidente na forma de ondas de alta frequência e ondas de borda laterais não lineares. É explorada a influência da amplitude e do comprimento da onda incidente no espalhamento da onda e nas forças geradas sobre o cilindro. Em seguida, investiga-se a Influência dos efeitos das ondas no wave run-up assumindo que o escoamento é potencial, a influência dos efeitos viscosos e influência dos efeitos da turbulência. Posteriormente, na segunda parte da tese, estudam-se os efeitos das mudanças na geometria submersa e na seção transversal do cilindro no campo de onda em seu entorno.

Abstract of Thesis presented to COPPE/UFRJ as a partial fulfillment of the requirements for the degree of Doctor of Science (D.Sc.)

NUMERICAL STUDY OF WAVE RUN-UP ON A FIXED SURFACE-PIERCING CYLINDER IN NON-BREAKING WAVES

Mohammad Mohseni

August /2018

Advisors: Sergio Hamilton Sphaier

Paulo de Tarso Themistocles Esperança

Department: Ocean Engineering

In wave-structure interaction, wave run-up is an important phenomenon that needs to be considered in the design of offshore structures. A thorough understanding of the physics of the nonlinear flow phenomena is necessary for the better insight into the run-up phenomenon. The present work, primarily, is focused on the hydrodynamic simulation of wave run-up and mainly seeks to evaluate the importance of high-frequency wave scattering types identified by Swan-et al. [2005] and lateral progressive edge waves on nonlinear wave amplification around a single fixed cylinder. The physics of the problem involves the interaction of single surface piercing cylinder with surface gravity incident waves which are propagating over a flat bed in an unbounded domain in deep water. The analysis is performed numerically using CFD based Navier-Stokes equations and Potential-flow theory. The numerical results are compared with experimental data provided by ITTC (OEC),[2013]. Taking into account the numerical simulation of the physical mechanism of wave scattering around the cylinder, the first part of the thesis deals with the investigation of the importance of the aforementioned high-frequency wave scattering and also lateral edge waves on nonlinear wave field and also inline wave force over a range of wave steepnesses and wavelengths. Then the Influence of potential flow, viscous and turbulence effects on wave run-up is explored. Afterward, in the second part of the thesis, the effects of the change in cylinder submerged geometry and finally, change in cross-section on the wave field around the cylinder is studied.

Contents

List of Figures	x
List of Tables	xiii
Nomenclature	xiv
1 Introduction	1
1.1 Statement of problem and motivation	1
1.2 Research background	2
1.3 Research objectives	6
1.4 Outline of the thesis	6
2 Methodology	7
2.1 Navier-Stokes model	8
2.1.1 Governing equations	8
2.1.2 Discretisation schemes	11
2.1.3 Modeling the Free Surface	12
2.1.4 Velocity-Pressure coupling	14
2.1.5 Solution of the linear algebraic equations	15
2.1.6 Wave generation and absorption	15
2.1.7 Boundary and initial conditions	17
2.1.8 Solver settings	18
2.1.9 Numerical calculation of wave forces on the cylinder	19
2.2 Potential flow Model	20
2.2.1 Governing Equation	20

2.2.2	Boundary conditions	21
2.2.3	Solving boundary value problem	22
3	Grid refinement study and Validation	30
3.1	Dimensionless parameters and wave conditions	30
3.2	Convergence study of the wave interaction with a single cylinder by Navier- stokes model	34
3.3	Convergence study of the wave interaction with a cylinder by Potential flow model	41
3.4	Comparisons with experimental data	44
3.4.1	Wave elevation around the cylinder	44
3.4.2	Wave forces on the cylinder.	47
4	Wave run-up on a vertical surface-piercing cylinder	52
4.1	The physical mechanism of wave scattering	52
4.2	Effect of wavelength on wave Run-Up	57
4.3	Effect of wave steepness on wave Run-Up	65
4.4	Effect of wavelength and steepness on inline wave force	67
4.5	Influence of potential flow, viscous and turbulence effects on wave Run-Up.	74
4.6	Effect of submerged geometry on wave Run-Up	78
4.7	Effect of cylinder cross-section on wave Run-Up	84
4	Conclusion Remarks and Future works	92
4.1	Conclusion	92
4.2	Future work	98
4	Bibliography	99

List of Figures

Fig 2.1. Definition sketch of BVP for a vertical cylinder in cylindrical coordinates. . . .	20
Fig 3.1. Different wave force regimes, (Chakrabarti, 1987), (left), Validity of wave theories graph, Le Méhauté (1976), (right)	33
Fig 3.2. Computational domain, geometry, and boundary conditions	36
Fig 3.3. Computational Mesh Free-surface plane and Symmetry plane and a cross-section of the refined mesh area around the free surface waves	37
Fig 3.4. Locations of wave probes around the single circular cylinder	37
Fig 3.5. Time history of normalized wave elevations at the front, shoulder, and back of the cylinder	40
Fig 3.6. Time history of normalized horizontal and vertical wave forces	40
Fig 3.7. Computational geometry and mesh for the body (left), inner free surface (middle) and outer free surface (right)	42
Fig 3.8. Normalized 1st harmonics of wave elevation around the cylinder, (vertical solid line ($r/D=0.513$) and vertical dash line ($r/D=1.0$))	48
Fig 3.9. Normalized 2nd harmonics of wave elevation around the cylinder, (vertical solid line ($r/D=0.513$) and vertical dash line ($r/D=1.0$))	49
Fig 3.10. Normalized mean value of wave elevation around the cylinder, (vertical solid line ($r/D=0.513$) and vertical dash line ($r/D=1.0$))	50
Fig 3.11. 1st and 2nd harmonics and mean value of horizontal force, under variation of wave steepness for both short and long waves	51
Fig 3.12. 1st and 2nd harmonics and mean value of vertical force, under variation of wave steepness for both short and long waves	51
Fig 4.1. Wave elevation profile and corresponding velocity components at four given wave phases interacting with cylinder front point	53
Fig 4.2. Spatial contours of the free surface elevation around the cylinder, wave condition $T=7s, H/L=1/16$	55
Fig 4.3. Continued, spatial contours of the free surface elevation around the cylinder, wave condition $T=7s, H/L=1/16$	56
Fig 4.4. Spatial contours of the free surface elevation around cylinder under variation of the wavelength for moderate steep waves, before the arrival of wave zero up crossing at back point	58
Fig 4.5. Spatial contours of the free surface elevation around cylinder under variation of the wavelength for moderate steep waves, the arrival of a wave crest at the front	59

point	
Fig 4.6. Spatial contours of the free surface elevation around cylinder under variation of wavelength for moderate steep waves ($H/L=1/16$), the arrival of wave crest at the back point	60
Fig 4.7. Comparison of normalized mean value and harmonics of wave run-up under variation of wavelength for moderate steep waves ($H/L=1/16$) (vertical solid line ($r/D=0.513$) and vertical dash line ($r/D=1.0$))	63
Fig 4.8. Normalized time history of wave elevations at given wave probes location around cylinder under variation of wavelength for moderate steep waves ($H/L=1/16$)	64
Fig 4.9. Spatial contours of the free surface elevation around cylinder under variation of wave steepness for short waves.	68
Fig 4.10. Spatial contours of the free surface elevation around cylinder under variation of wave steepness for short waves	69
Fig 4.11. Spatial contours of the free surface elevation around cylinder under variation of wave steepness for long waves	70
Fig 4.12. Spatial contours of the free surface elevation around cylinder under variation of wave steepness for long waves	71
Fig 4.13. Comparison of normalized mean value and harmonics of wave run-up under variation of wave steepness for both short and long waves (vertical solid line ($r/D=0.513$) and vertical dash line ($r/D=1.0$))	72
Fig 4.14. The inline force with free surface elevation time histories at the front and back point of the cylinder under wave condition of ($T=7s$ and $T=15s$, $H/L=1/16$)	73
Fig 4.15. The first six harmonics of inline wave force under variation of wave steepness and wavelength	74
Fig 4.16. Numerical predictions of the scattered wave-field around a cylinder with a diameter of $D = 0.1m$. Christou-[2009]	76
Fig 4.17. Qualitative comparisons of the scattered wave-field between the numerical predictions and the laboratory observations of Swan et.al [2005] with a diameter of $D = 0.1m$, Christou-[2009]	76
Fig 4.18. Vorticity magnitude contour along the centerline ($y = 0$) of the cylinder	78
Fig 4.19. The geometries related to change in vertical cylinder draft, with or without attached substructure under the wave condition of ($T=7s$, $H/L=1/16$) in deep water . .	79
Fig 4.20. Comparison of normalized mean value and harmonics of wave run-up around the vertical cylinder under wave condition of ($T=7s$, $H/L=1/16$)	82
Fig 4.21. Spatial contours of the free surface elevation around the vertical cylinder under wave condition of ($T=7s$, $H/L=1/16$), with the arrival of wave crest at the front point	83
Fig 4.22. Spatial contours of the free surface elevation around the vertical cylinder under wave condition of ($T=7s$, $H/L=1/16$), with the arrival of wave trough at front point	83
Fig 4.23. Spatial contours of the free surface elevation around the vertical cylinder under wave condition of ($T=7s$, $H/L=1/16$), with the arrival of the wave, zero up crossing at the front point	84
Fig 4.24. The geometric variation of the cross-section for truncated cylinders corresponding to five given value of corner ratio.	85

Fig 4.25. Spatial contours of the free surface elevation around the cylinder for cross-section variation under wave condition of ($T=7s$, $H/L=1/16$), with the arrival of wave crest at the front point	87
Fig 4.26. Spatial contours of the free surface elevation around the cylinder under wave condition of ($T=7s$, $H/L=1/16$), with the arrival of wave crest at the back point.	88
Fig 4.27. Spatial contours of the free surface elevation around the cylinder under wave condition of ($T=7s$, $H/L=1/16$), with the arrival of wave trough at front point.	88
Fig 4.28. Spatial contours of the free surface elevation around the cylinder under wave condition of ($T=7s$, $H/L=1/16$), with the phase between the arrival of the wave trough and zero up crossing at the front point	89
Fig 4.29. Spatial contours of the free surface elevation around the cylinder under wave condition of ($T=7s$, $H/L=1/16$), with the arrival of wave zero up crossing at the front point	90
Fig 4.30. Comparison of mean value and harmonics of wave run-up for cross-section variation under wave condition of ($T=7s$, $H/L=1/16$) (vertical solid line ($r/D=0.513$) and vertical dash line ($r/D=1.0$))	91

List of Tables

Table 2.1. The discretization of PDE terms in InterFoam v.2.2.2	12
Table 2.2. Summary of the boundary conditions implemented in NWT	18
Table 3.1. Selected incident wave conditions for Navier-Stokes Solver	33
Table 3.2. Main particulars for single cylinder	34
Table 3.3. Spatial and temporal discretization for convergence study of wave interaction with a vertical circular cylinder	38
Table 3.4. Convergence Statics for normalized 1st harmonics of wave elevation	40
Table 3.5. Convergence Statics for normalized 1st harmonics of horizontal and vertical wave forces	40
Table 3.6. Body Mesh resolution (per quadrant)	43
Table 3.7. Convergence study for the first-order solution by body mesh set-up	43
Table 3.8. Free surface mesh resolution (per quadrant)	43
Table 3.9. Convergence study for second order solution	44

Nomenclature

Abbreviations

NWT	Numerical wave tank
SWL	Still water line
OpenFOAM	Open Field Operation And Manipulation
WAMIT	WaveAnalysisMIT
2D	Two Dimensional
3D	Three Dimensional
DFT	Discrete Fourier Transform
URANS	Unsteady Reynolds Averaged Navier-Stokes
DES	Detached eddy simulation
VOF	Volume of Fluid
ITTC	International towing tank conference
OEC	Ocean engineering comitte
B.C	Boundary consition
GCI	Grid Convergence Index
FS	Safety factor
CFD	Computational fluid dynamic
FVM	Finite volume method
BEM	Boundary element method
BVP	Boundary value problem
PDE	Partial differential equation
GWK	Large Wave Flume-GWK - Hydralab+
NS3	Navier-stokes 3
DHI	Danish Hydraulic Institute
CSF	Continuum Surface Force
MULES	Multidimensional Universal Limiter for Explicit Solution
CFL	Courant–Friedrichs–Lewy
Co	Courant numbe
SIMPLE	SemiImplicit Method for Pressure-Linked Equations
PISO	Pressure Implicit with Splitting of Operators
PIMPLE	combining the methods SIMPLE and PISO
PCG	Preconditioned Conjugate Gradient
DIC	Diagonal-based Incomplete Cholesky
PBiCG	Preconditioned Bi-Conjugate Gradient
DILU	Diagonalbased Incomplete Lower-Upper

Symbols

∂	Partial derivative
t	Time
Δt	Time step
Δ	Grid spacing
Δx	Grid spacing in X-direction
Δy	Grid spacing in y-direction
Δz	Grid spacing in z-direction
Δr	Grid spacing in radial-direction
α	Water volume fraction
μ	Dynamic viscosity
μ_{eff}	Effective dynamic viscosity
ν	Kinematic viscosity
ρ	Density
g	Gravitational constant
h	Still water depth
u	Horizontal velocity component
w	Vertical velocity component
U_m	Maximum horizontal velocity of water particles
x	Horizontal axis
y	Transversal axis
z	Vertical axis
η	Surface elevation
κ	Mean curvature of the interface
σ	Water-air interface surface tension
ϕ	Wave phase, physical quantity, scalar velocity potential
θ	Phase angle
θ_0	static contact angle
ω	Wave radial frequency
f	Wave frequency
Σ	Sum
γ	Scale factor
R_u	Wave run-up height
A	Wave amplitude

H	Wave height
T	Wave period
L	Wavelength
k	Wave number
D	Characteristic horizontal length, diameter
a	Half characteristic horizontal length
r	radius
R_u/A	Relative wave run-up
ka	Wave diffraction parameter
kA	Wave steepness parameter
H/L	Wave steepness parameter
KC	Keulegan-Carpenter number
Re	Reynolds number
Fr	Froude number
kh	Relative water depth number
RAO	Response amplitude Operator
QTF	Quadratic transfer function
We	Weber number
$N_{\text{Tangential}}$	Number of cells around the cylinder
$D/\Delta r_{\text{Refinement}}$	Number of cells in the radial direction
N_R	Number of cells in the radial direction
N_z	Number of cells in the vertical direction
$T/\Delta t$	Number of time steps
ε_{21}	Change in the numerical solution between Mesh 1 and 2
ε_{32}	Change in the numerical solution between Mesh 2 and 3
R, r	Convergence ratio
p	Order-of-accuracy
F_x	Horizontal wave force
F_z	Vertical wave force
S_b	Submerged body surface
S_f	Free surface
S_∞	Infinite extension
S_s	Sea-bed
ζ	Displacement of the free-surface from its mean position

d	Water depth
∇	Three-dimensional del operator
p	Total pressure
τ	Stress tensor
F^{FS}	Volumetric surface tension force
X	Position vector
U	Velocity field
U_c	Artificial interfacecompression velocity
δ	Dirac delta function
Γ	Diffusivity
S_ϕ	Source term
C_α	Interface compression constant
Ω	Surface of the body
D/Dt	Material derivative
ε	Perturbation parameter
ϕ_I	Incident velocity potential
ϕ_s	Scattered velocity potential
ϕ_D	Diffracted velocity potential
ϕ_R	Radiated velocity potential
Q	Quadratic forcing function

Chapter 1

Introduction

1.1- Statement of problem and motivation

Offshore structures such as platforms, wind-power plants, marine renewable energy devices, have been in rapid growth in ocean regions. In recent years, the offshore industry has moved towards deeper water and harsher environments. The real sea states are three-dimensional with multi-directional nonlinear waves and the offshore structures may suffer serious damage due to the rough sea climate. Therefore, a thorough understanding of wave–structure interaction is necessary to be able to make a safe, reliable and cost-effective design. Offshore cylindrical structures are usually consisting of a superstructure supported by vertical surface-piercing circular/square cylinder column which involves some wave induced processes such as wave diffraction, reflection, transmission, and radiation as free surface hydrodynamics. The corresponding disturbances and deformation at free surface are usually associated with a considerable rapid amplification of the local free-surface elevation surrounding these columns and consequently hydrodynamic loads on them. In this instance, two principal localized free-surface effects are important to platform designers: wave run-up and air-gap. The **air-gap** is defined as the distance between the water level and the underside of the deck. The appropriate design of column-types structures requires accurate predictions of the maximum wave run-up height to maintain sufficient air-gap below the platform deck which can cause some important strongly nonlinear phenomena particularly in the harsh environment or severe storm conditions. An unnecessary increase in air gap can increase platform fabrication costs and the overall weight of the offshore structure, which can in turn, adversely affect the structure's stability, platform's performance, and general sea-keeping ability. Conversely, an under-estimation of the air gap can

imply a large amount of load to the structure and consequently ends to significant structural damage to the offshore structures.

The constructive or destructive wave-wave and wave-structure interaction of incident and scattered waves result in highly non-linear wave amplification around a partially immersed structure. This thin jet-like column of water in the upward direction is referred to **wave run-up**. Physically, there is the conversion of the kinetic energy of water particles into potential energy during the run-up on a fixed cylinder. Wave run-up may result in, wave impacts and wave slamming on the column/deck and upper structures or equipment close to deck level, green water, and ringing which are highly nonlinear by their nature. They can cause important and violent wave events and imply a large amount of load to the structure and consequently can result in significant structural damage to the offshore structures. Due to the many complicated features such as breaking, air entrainment, and turbulence, it is still not possible to describe the run-up flow exactly and present wave run-up prediction methods are inadequate and much is still not sufficiently understood. Hence, development of an effective and accurate numerical tool for the prediction of wave run-up height and loads is both necessary and inevitable for the optimal design of offshore structures.

1.2- Research background

Potential flow theory is the common numerical approach to study the wave run-up height and forces on a surface piercing bodies in the presence of progressive water. For interactions between waves and structures with simple geometries, analytical or semi-analytical solutions can be obtained. The diffraction of surface water waves around surface piercing cylinders is a classical problem, which has been investigated in a large number of studies over many decades. In the early days, Havelock [1940] and McCamy and Fuchs [1954], presented an analytic solution of diffraction for a bottom-mounted single circular cylinder in regular waves, based on linear potential theory, in water of infinite and arbitrary depth, respectively. For steep waves, however, linear diffraction theory is not sufficient for predicting wave run-up accurately, due to the highly non-linear fluid motion. In practice, it has been observed in model tests, Niedzwecki et al.[1992] and Kriebel [1992], that the linear assumption may significantly under-predict the crest elevation around columns in steep waves. Furthermore, second-order and higher-order effects were observed by Stansberg et al. [2001], Stansberg et al. [2002], and Kristiansen et al.[2004]. Based

on the benchmark study by Nielsen [2003], Stansberg et al.[2005] remarked that non-linear tools based on potential theory have some limitations due to model wave-breaking and viscous effects in simulating non-linear wave-body interaction flows. They observed poor agreement with both linear and second-order diffraction solutions, particularly in steep incident waves. Higher-order potential flow effects have been analyzed by several authors but tools are still in the developing phase. The only known instances where fully nonlinear potential based predictions of the wave run-up have been validated against model experiments are presented by Nielsen [2003]. The analysis of the results indicated that neither of the studies by these researchers presented an acceptable agreement of measured results and fully-nonlinear predictions.

Physical experimentation is one of the most common approaches for studying wave-structure interaction. The benchmark experiments of Kriebel [1990, 1992] for regular wave run-up on a circular cylinder in water of finite depth have subsequently been compared with a number of wave run-up calculation procedures. These include the linear diffraction theory approach of McCamy and Fuchs [1954], the second-order frequency domain calculation procedure presented by Kriebel [1990, 1992], Isaacson and Cheung [1994] and Buchmann et al. [1998] and second order time domain calculation approach of both Buchmann et al. [1997] and Isaacson and Cheung [1993]. In general, these researchers demonstrated that first order wave run-up predictions revealed an overall poor agreement when compared to the measured results of Kriebel [1990]. On the other hand, comparisons with second-order approaches, both frequency and time domain diffraction theory, for waves of small steepness were shown to be acceptable. Niedzwecki et al. [1992] performed a small-scale experimental study to investigate wave run-up on rigid full-length and truncated circular cylinders under regular and random sea conditions. Morris-Thomas et al. [2003,2004], conducted a series of experiment to study cross-section effects on harmonics of wave run up on the fixed vertical surface piercing cylinder using monochromatic progressive waves. They compared the experimental results with a solution of diffraction theory by WAMIT and concluded that with long wave theory, the wave run-up is well predicted. Ramirez et al. [2013] studied wave run-up of irregular waves on vertical monopiles by conducting large-scale experiments with a focus on the near breaking and breaking waves. Several numerical simulations based on diffraction theory and experimthe ent, Bai et al. [2007], Ning et al. [2009], attempted to model focused waves run-up and the nonlinear interaction with a vertical fixed cylinder. Swan et al. [2005, 2015] highlighted the importance of nonlinear wave

scattering from a slender vertical surface piercing column and also investigated the nonlinear, higher-harmonic, wave loading experimentally and characterized high-frequency wave scattering around the cylinder as Type 1&2. They also explained, why low-order diffraction solutions are inappropriate.

In the recent years, several types of research have been carried out on the study of the wave run-up on monopiles and columns of large semisubmersibles using Computational Fluid Dynamics (CFD) based Navier-Stokes equations. The conclusion of the studies indicates the importance of highly nonlinear wave-structure interaction effects as well as large distortions of the free surface motion. These effects cannot be predicted well by potential theory and it shows the need for computational efforts for accurate predictions, Danmeier [2008] and Bøckmann [2014]. A numerical wave tank model was developed by Kim et al. [2011] by matching the far-field wave solution based on the potential-flow theory and the near-field CFD solution. The developed method was applied to a truncated vertical cylinder exposed to nonlinear regular waves. Ramírez et al. [2011] presented a CFD model (NS3) with no-turbulence model, to simulate the wave run-up on a vertical circular cylinder and the numerical results were compared to the experimental data from GWK. Peng et al. [2012] studied wave run-ups on a monopile foundation in both regular and irregular waves using a 3-D ComFLOW model with no-turbulence model and reproduced experimental data measured by De Vos et al. [2007]. Alfonsi [2015] addressed the phenomenon of diffraction of linear waves impinging on large-diameter, surface-piercing, vertical circular cylinder numerically, within three different theoretical frameworks of hypotheses, Potential Theory, Euler equations and Navier-Stokes equations (with the DNS approach). In order to evaluate the capabilities of state-of-the-art CFD codes for wave run-up simulation for single/multiple surface-piercing cylinders in regular non-breaking waves, the ITTC Ocean Engineering Committee (OEC) [2013], provided a benchmark test based on experimental data measured from MOERI and MARINTEK for single (1C) and four circular cylinders (4C), respectively. Cao et al. [2017] and also Sun et al. [2016] utilizing OpenFOAM without the inclusion of any turbulence model, they conducted simulations of the wave run-up around a truncated vertical cylinder for various wave conditions. Comparing the numerical results with the aforementioned published experimental data the accuracy of the solver was validated, and then they investigated the effects of wavelength and steepness on wave amplification around the cylinder and maximum wave run-up height, as well. Yoon et al. [2016]

employing CFDShip-Iowa with no-turbulence and then the inclusion of turbulence model of blended $k-\varepsilon/k-\omega$ based isotropic and anisotropic RANS, and DES approaches with near-wall or wall functions, similarly did this investigation. They also studied the effect of wave diffraction, the interaction between four circular cylinders, statistical convergence, grid, domain and turbulence model sensitivity. Several researchers modeled focused waves interaction with a fixed and vertical surface piercing cylinder based on the CFD approach. Paulsen et al. [2013] performed numerical computations of wave loads on surface piercing circular cylinders at intermediate water depths for nonlinear regular and irregular waves, phase-focused irregular waves and multidirectional irregular waves using a fully nonlinear-coupled solver (higher-order potential flow and OpenFOAM with the no-turbulence model. Chen et al. [2014] numerically investigated the nonlinear interaction of non-breaking regular and focused waves with a vertical surface piercing cylinder for different wave conditions. They used OpenFOAM (no-turbulence model) and compared the numerical results with physical experiments performed at the Danish Hydraulic Institute (DHI). Bihs et al. [2017] simulated both non-breaking and breaking focused waves and investigated changes in kinematics and the free surface flow features during the interaction with a vertical circular cylinder under both small and high steep waves using the open-source CFD model REEF3D (no-turbulence model). Kamath et al. [2015, 2016], modeled the wave interaction with a single vertical cylinder, three cylinders placed in tandem, three cylinders placed side by side, four-cylinder group and a 3×3 square array of nine cylinders at low KC numbers to study the change in the hydrodynamics and the wave forces employing REEF3D with no-turbulence model. Lin et al. [2017], discussed the effects of wave nonlinearity and scattering on run-up heights and wave loads by comparing the wave steepness parameter and scattering parameter for three different types of wind turbine foundations. They conducted the numerical simulation, based on the commercial software FLUENT with $k-\varepsilon$ turbulence model. Devolder et al. [2017], presented a study of wave run-up around a monopile subjected to regular waves using the OpenFOAM. RANS turbulence modeling was performed by applying a buoyancy-modified $k-\omega$ SST turbulence modeling and they validated this model based on laboratory data of De Vos et al. [2007].

1.3- Research objectives

Based on the above studies, this thesis is aimed to improve the knowledge of the Wave Run-Up problem. Kriebel [1992] and Stansberg et al.[2005], illustrated the different contributions of non-linear effects to the total wave amplification around vertical, surface-piercing cylinders. Taking into account these important contributions and with regard to the benchmark experiment provided by ITTC (OEC), [2013], in the present study, the importance of high-frequency wave scattering Type 1&2 identified by Swan et al. [2015] and also lateral edge waves on nonlinear wave field and corresponding harmonics around a single cylinder and also inline wave force is numerically investigated. In the first part of the thesis, the related simulations are conducted under different wave conditions based on the parametric variation of wave diffraction, \mathbf{ka} , and wave steepness, \mathbf{kA} . Afterward, the influence of potential flow, viscous and turbulence effects on wave run-up is explored. In the second part of the thesis, the role of the aforementioned high-frequency wave scattering and also lateral edge waves on nonlinear wave field around the cylinder with the change in submerged geometry is studied. Presently, the work of Nielsen [2000], Morris-Thomas et al. [2003] and Repalle et al. [2007] are the only instances where the wave run-up on vertical cylinders with different cross-sections have been investigated. Hence, more detailed information is presented to have a deeper insight into the wave run-up phenomena due to the change in cross-section.

1.4- Outline of the Thesis

This thesis is arranged into 5 chapters which are explained in summary in the following. The motivation, background, and objectives of this study are presented in Chapter 1. The methodology of numerical approach including Navier-Stokes model and Potential flow model is described in detail in Chapter 2. Describing the dimensionless parameters that contribute to the physics of problem in Chapter 3, the selected waves conditions and the grid refinement study and comparisons with experimental data are presented. In Chapter 4, the aforementioned objectives are explored. Therefore, the Navier-Stokes model is used to perform several simulations to investigate the physical mechanism of wave scattering, the effect of wavelength and wave steepness and then the effects of the change in submerged geometry and change in cross-section on the wave field around the cylinder. Finally, the conclusions based on the present analysis and the future works are remarked in Chapter 5.

Chapter 2

Methodology

The physics of wave scattering and run-up around an isolated, vertical and surface-piercing cylinder involves high-frequency steep waves. In this thesis, these wave transformations are studied numerically using CFD based Navier–Stokes equations as the main approach and then Potential flow theory. The Navier-Stokes model is based on the fully nonlinear Navier-Stokes solver which is used for the accurate simulation of the complex free surface flows and fluid-structure interactions. Based on the aims of the present study, interFoam version 2.2.2 which is the standard multiphase/incompressible module of the open source code of OpenFOAM® has been selected to run the necessary simulations. It solves the three-dimensional Unsteady Reynolds Averaged Navier–Stokes (URANS) equations using the finite volume discretization. VOF phase-fraction based algebraic interface capturing approach is used to solve and represent the free surface. The governing equations are discretized in the fluid domain on a static and structured multi-block mesh. A potential flow model based on the linear theory is used to solve the diffraction/radiation problem. In this study, WAMIT version 6.1/6.107S is used to run the necessary simulations. WAMIT is a three-dimensional free surface, frequency domain solver that solves the velocity potential of the fluid through the Boundary Element Method (BEM).

For Navier–Stokes model, the mathematical formulation and equation discretization are explored to better understand the source code. Thus, the governing equations are explained in a mathematical model by section 2.1.1. The discretization schemes which is used to discretize the general transport equation in finite volume framework is presented in section 2.1.2. The numerical approach to model the free surface is illustrated in section 2.1.3. Afterward, the method which is used for wave generation and absorption is explained in section 2.1.4. The details of approach for velocity-pressure coupling and then solution of the linear algebraic equations are given in section 2.1.5 and 2.1.6, respectively. The initial and

boundary conditions along with necessary solver settings are explained in section 2.1.7 and 2.1.8, respectively. Finally, the wave forces calculation is given in section 2.9.1. For Potential flow model, the governing equations and boundary conditions are presented in section 2.2.1 and section 2.2.2, respectively. Then the boundary value problem including the first and the second order solution and finally the expression for the free-surface elevation of the fluid domain surrounding the body are given in section 2.2.3.

2.1- Navier–Stokes model

2.1.1- Governing equations

In this Section, a mathematical representation of the simultaneous flow of two fluids is presented. These fluids are assumed to be immiscible, incompressible, isothermal, isotropic, homogeneous Newtonian fluids, each having a constant viscosity (OpenCFD Ltd, 2012). This mathematical representation includes surface tension but neglects heat and mass transfer. Hence the conservative differential form of governing equations of continuum mechanics for mass continuity and momentum equations which link pressure and velocity in a Eulerian-Inertial frame of reference, in vector notation, is given by:

$$\nabla \cdot \mathbf{U} = 0 \quad 2.1$$

$$\frac{\partial \rho \mathbf{U}}{\partial t} + (\rho \mathbf{U} \cdot \nabla \mathbf{U}) = -\nabla p + \nabla \cdot \boldsymbol{\tau} + \rho \mathbf{f} + \mathbf{F}^{\text{st}} \quad 2.2$$

where all the bold letters indicate a vector field, $(\nabla = (\partial_x, \partial_y, \partial_z))$ is the three-dimensional del operator, (ρ) is the fluid density, (t) is the time, $(\mathbf{U} = (u, v, w))$ is the velocity field in Cartesian coordinates, (p) , is total pressure, $(\boldsymbol{\tau})$ is the stress tensor, (\mathbf{F}^{st}) represents the source of momentum due to surface tension and (\mathbf{f}) stands for the acceleration due to body forces. In this study, the only body force acting on the system is gravity, i.e. $(\mathbf{f} = \mathbf{g})$, $[0; 0; -9.81 \text{ (m/s}^2\text{)}]$. Before discretization, three terms of the momentum equations of Eqn. (2.2) are reformulated to match the OpenFOAM momentum equation form. Therefore, firstly, the modified pressure is introduced into the equation; then, the viscous stress term is expanded and finally, the term due to surface tension effect is defined.

The specification of the pressure boundary conditions is simplified if the modified pressure is used as a dependent variable. This term is advantageous for the specification of pressure at the boundaries of the space domain, Rusche [2002]. It is defined as:

$$P^* = p - \rho \mathbf{g} \cdot \mathbf{X} \quad 2.3$$

Where $(\mathbf{X} = (x, y, z))$ is the position vector and (P^*) stands for the modified pressure, which is obtained by removing the hydrostatic pressure from the total pressure, (p) . The negative gradient of the modified pressure (P^*) consists of the static pressure gradient, the body force due to gravity and an additional contribution originating from the density gradient.

$$-\nabla P^* = -\nabla p + \nabla(\rho \mathbf{g} \cdot \mathbf{X}) = -\nabla p + \rho \mathbf{g} + \mathbf{g} \cdot \mathbf{X} \nabla \rho \quad 2.4$$

Considering assumption of Newtonian fluid which means the shear stress in the fluid is proportional to the rate of strain, the viscous stress (deviatoric) term $(\nabla \cdot \boldsymbol{\tau})$ is decomposed into a more convenient form for discretization as follow:

$$\begin{aligned} \boldsymbol{\tau} &= \mu_{eff} (\nabla \mathbf{U} + (\nabla \mathbf{U})^T) \\ \nabla \cdot \boldsymbol{\tau} &= \nabla \cdot (\mu_{eff} \nabla \mathbf{U}) + (\nabla \mathbf{U}) \cdot \nabla \mu_{eff} \end{aligned} \quad 2.5$$

In Eqn. (2.5), $(\mu_{eff} = \mu + \mu_t)$ is the effective dynamic viscosity with (μ) being the molecular dynamic viscosity and (μ_t) is the turbulent viscosity where in this work the turbulent viscosity is set to zero and No-Turbulence model is considered. The surface tension at the interface between the two phases generates an additional pressure gradient resulting in external volumetric surface tension force (F^{ST}) . However, in the interface-capturing methodology (and other volume methods), the interface is not tracked explicitly and consequently, its exact shape and location are unknown, Rusche [2002]. Thus in interFoam, the **Continuum Surface Force (CSF)** model developed by Brackbill et al. [1992], is applied which overcomes this problem. This model represents the surface tension effects as a continuous volumetric force acting within the transition region. It reads:

$$\mathbf{F}^{\text{ST}} = \left(\int_{S(t)} \sigma \kappa' \mathbf{n}' \delta(\mathbf{X} - \mathbf{X}') dS \right) \approx \sigma \kappa \nabla \alpha \quad 2.6$$

Where $S(t)$ is the air-water interface, (α) phase fraction, $(\delta(\mathbf{X} - \mathbf{X}'))$ is the three-dimensional Dirac delta function, (σ) represents the surface tension coefficient at the free surface. In this CSF model, $(0 \leq \alpha \leq 1)$, is the water volume fraction in a mesh cell, the mean curvature of the free surface (κ) is formulated from local gradients in the surface normal (\mathbf{n}) at the interface, which is a function of the phase fraction $(\mathbf{n} = \nabla \alpha)$ and is given by:

$$\kappa = \nabla \cdot \hat{\mathbf{n}} = \nabla \cdot \frac{\mathbf{n}}{|\mathbf{n}|} = \nabla \cdot \left(\frac{\nabla \alpha}{|\nabla \alpha|} \right) \quad 2.7$$

Taking into account the modified pressure Eqn. (2.4), the viscous stress term Eqn. (2.5), a volumetric form of surface tension Eqn. (2.6), the final form of the momentum equation which is adapted to OpenFOAM® formulation is given by:

$$\frac{\partial \rho \mathbf{U}}{\partial t} + \rho \mathbf{U} (\nabla \cdot \mathbf{U}) = (-\nabla P^*) - ((\mathbf{g} \cdot \mathbf{X}) \nabla \rho) + ((\nabla \mathbf{U} \cdot \nabla \mu_{\text{eff}}) + \nabla \cdot (\mu_{\text{eff}} \nabla \mathbf{U})) + (\sigma \kappa \nabla \alpha) \quad 2.8$$

2.1.2- Discretisation schemes

The standard Gaussian finite volume integration method, which is based on summing values on cell faces, is usually used to get the higher accuracy of the integrations for derivative terms, The values on cell faces are interpolated from collocated cell centers where the flow field variables are stored. The governing equations Eqn. (2.1) and Eqn. (2.8) can be written as a generic standard transport equation. This partial differential equation which represents a conservation law of any physical quantity (ϕ) per unit volume is given in the form of:

$$\underbrace{\frac{\partial \rho \phi}{\partial t}}_{\text{time derivative}} + \underbrace{\nabla \cdot (\rho \mathbf{U} \phi)}_{\text{convection (advection) term}} = \underbrace{\nabla \cdot (\Gamma \nabla \phi)}_{\text{diffusion term}} + \underbrace{S_\phi(\phi)}_{\text{source term}} \quad 2.9$$

Where (Γ) is the diffusivity and $(S_\phi(\phi))$ represents a source term. The terms in the standard transport equation represent the local transient change of (ϕ) (time derivative) and

convective change due to the flux of (ϕ) (convection term), is balanced by the rate of transport due to diffusion (diffusion term) and the rate of production/destruction per unit volume (source term).

This transport equation is a second-order equation, as the diffusion term includes the second derivative of (ϕ) in space. For good accuracy, it is necessary for the order of the discretization to be equal to or higher than the order of the equation that is being discretized. The discretization practice adopted in this work is also second-order accurate in space and time and will be presented in brief in following. A Finite Volume discretization of Eqn. (2.9) is formulated by integrating over the control volume V_P and time. Thus the volume integral form, results:

$$\int_t^{t+\Delta t} \left[\frac{\partial}{\partial t} \int_{V_P} \rho \phi dV + \int_{V_P} \nabla \cdot (\rho \mathbf{U} \phi) dV \right] dt \quad 2.10$$

$$= \int_t^{t+\Delta t} \left[\int_{V_P} \nabla \cdot (\rho \Gamma_\phi \nabla \phi) dV + \int_{V_P} S_\phi(\phi) dV \right] dt$$

There are several built-in numerical schemes in OpenFOAM for the temporal and spatial discretization of the volume integral form of transport equation, Eqn. (2.10). The details on finite volume discretization can be extensively found in the bibliography (Jasak [1996], Rusche [2002] and Berberovic [2009]). An overview of the discretization schemes used in this work is given in Table 2.1.

2.1.3- Modeling the Free Surface

Accurate simulation of a moving fluid interface, particularly one which is highly distorted, is extremely challenging in CFD. The position of the interface must be calculated as part of the solution as it is not known in advance of any given time-step. In this study combination of Volume Of Fluid (VOF) technique, with bounded compression techniques is used to identify the position of the free surface location. A brief explanation of this method and its implementation in OpenFOAM is given below. For a more general approach and further details the reader is referred to Rusche [2002], Berberovic [2009].

Table 2.1. The discretization of PDE terms in InterFoam v.2.2.2		
	Term	Discretisation
Spatial domain		Finite Volume Method (FVM)
Temporal Schemes	ddtSchemes $\left(\frac{d}{dt}\right)$	Backward, Second order implicit, unbounded.
Gradient Schemes	default	cellMDLimited Gauss linear 1, Second-order, Bounded
	$(\nabla\mathbf{u}, \nabla\alpha)$	cellMDLimited Gauss linear 1, Second-order, Bounded
Divergence Schemes	$\nabla\cdot(\rho\phi\mathbf{u})$	Gauss limitedLinearV 1, Second-order, Bounded
	$\nabla\cdot(\phi\alpha)$	Gauss vanLeer01, Second-order, Bounded
	$\nabla\cdot(\rho\phi_{rb}\alpha)$	Gauss interfaceCompression, second-order
Laplacian Schemes	∇^2	Gauss linear corrected, second-order, unbounded
Interpolation Schemes	default	Linear, Second-order
Surface normal gradient Schemes	default	Corrected, Second-order

In VOF (Hirt and Nichols [1981]) which is known as a front-capturing method, each phase is described by scalar non-dimensional indicator function (α) that moves with the fluid and represents the fraction of the volume of a cell that is occupied by a given fluid, here water. In the single-field formulation, two immiscible fluids are considered as one effective fluid throughout the domain. The physical properties of which are calculated as weighted averages based on the distribution of the water phase fraction, being equal to the properties of each fluid in the regions they occupy and varying only across the interface. Therefore the local fluid properties (ρ, μ, \mathbf{U}) are weighted mixture of the physical properties of both fluids by the following constituent equations.

$$\mathbf{U} = \alpha\mathbf{U}_w + \mathbf{U}_a(1-\alpha) \quad \rho = \alpha\rho_w + \rho_a(1-\alpha) \quad \mu = \alpha\mu_w + \mu_a(1-\alpha) \quad 2.11$$

Where subscripts (a) and (w) represent air and water respectively. Once the velocity field is known, the transport of the indicator function (α) is advanced in time by a classic advection-diffusion equation which is mathematically hyperbolic, as follow:

$$\frac{\partial \alpha}{\partial t} + \nabla \cdot (\mathbf{U} \alpha) = 0 \quad 2.12$$

The important issue in numerical simulations of free-surface flows using the VOF model is the sharp resolution of the interface while preserving the boundness and conservation of the phase fraction (α) . The VOF method is numerically rather diffusive due to discretization error. Therefore, the interface region between the phases is artificially smeared due to the numerical diffusion. In the present study, the artificial bounded compression approach according to Weller [2002] is utilized to overcome such difficulties. In this method instead of applying a compressive differencing scheme, an artificial compression term $(\nabla \cdot [\mathbf{U}_c \alpha (1 - \alpha)])$ is added to the conventional transport equation Eqn. (2.12). This yields the final expression, Eqn. (2.13) which is adopted in the present study. In general, this interface compression term lacks physical meaning and it acts against the numerical diffusion, limits the amount of interface smearing and sharpens the interface between two fluids without affecting the solution. This formulation is conservative and takes non-zero values only at the interface and removes the need for specialized convection schemes as used in other codes.

$$\frac{\partial \alpha}{\partial t} + \nabla \cdot (\mathbf{U} \alpha) + \nabla \cdot [\mathbf{U}_c \alpha (1 - \alpha)] = 0 \quad 2.13$$

In which (\mathbf{U}) is the weighted average velocity and (\mathbf{U}_c) is the artificial interface-compression velocity, normal to the free surface. This velocity which its magnitude is proportional to the instantaneous velocity, in OpenFOAM® it is calculated from:

$$\mathbf{U}_c = \min \left[C_a |\mathbf{U}|, \max(|\mathbf{U}|) \right] \frac{\nabla \alpha}{|\nabla \alpha|} \quad 2.14$$

Where (C_a) is interface compression constant which is a scalar parameter controlling the extent of artificial compression velocity usually between 0 and 2 with the recommended

value of 1. If a larger value is used, the compression of the interface increases, leading to larger detrimental velocity gradients around that interface. Finite Volume Method (FVM) does not guarantee boundness of the phase fraction. Hence, OpenFOAM, independent of the numerical discretization schemes utilizes an effective interface compression method of Multidimensional Universal Limiter for Explicit Solution (MULES) which created by (OpenCFD Ltd, 2012). MULES is fundamentally an explicit second-order method that is used for temporal integration and introduces a strict CFL number limit and hence time step limit when running the solvers. Open CFD-[2012]. In newer versions from OpenFOAM-2.3.0, a new semi-implicit variant of MULES was introduced which combines operator splitting with the application of the MULES limiter to an explicit correction rather than to the complete flux. In principle, this is advantageous, as it will enhance the stability for larger Courant numbers, Open CFD [2014].

2.1.4- Velocity-Pressure coupling

It is difficult to solve the incompressible form of the Navier-Stokes equations directly, despite the determinate system of equations and unknowns. The form of the equations discretized in Eqn. (2.8) shows linear dependence and strong coupling of the velocity field on pressure and vice-versa. This inter-equation coupling requires a special treatment. Using the Segregated Approach, the equations system is solved in sequence. The SIMPLE (Semi-Implicit Method for Pressure-Linked Equations) and PISO (Pressure Implicit with Splitting of Operators) are the most popular methods of dealing with inter-equation coupling in the pressure-velocity system. The PISO (Pressure Implicit with Splitting of Operators) approach is suitable for transient simulations where it is necessary to fully solve the velocity-pressure coupling for each time step. The non-linear effects of the velocity are reduced setting small time steps characterized by Courant numbers below one. The Semi-Implicit Method for Pressure-Linked Equations (SIMPLE) algorithm is used to solve steady-state problems iteratively with under-relaxation. Therefore it is not necessary to fully resolve the linear pressure-velocity coupling (PISO algorithm). Since the effective time-step is much larger the treatment of the non-linear effects of the velocity during the resolution is more important than the precise determination of the pressure field. As each iteration is equivalent to a pseudo time step, the properties are under relaxed in order to stabilize the method and improve convergence. There is another approach which is called PIMPLE. This two-step method is the results of combining the methods SIMPLE and PISO and takes benefit of both of them. Its main structure is inherited from the original PISO, but it allows equation under-relaxation,

as in SIMPLE, to ensure the convergence of all the equations at each time step, resulting in quick and stable solutions. The models presented in this study will use the PIMPLE scheme as it is the current scheme in use within the InterFoam models.

2.1.5- Solution of the linear algebraic equations

Generally speaking, the Navier–Stokes equations are first integrated over the whole solution domain and time domain. Second, the solution and time domain is discretized into a number of cells and time steps, respectively. The discretization procedure converts every partial differential equation into a corresponding system of linear algebraic equations, with one equation for each control volume (computational cell). The systems of linear algebraic equations can be expressed in a matrix notation as $([\mathbf{A}][\phi]=[\mathbf{R}])$ where $[\mathbf{A}]$ is a sparse square matrix, $[\phi]$ is the column vector of the dependent variable (unknown) and $[\mathbf{R}]$ is the source vector. This system is solved using the iterative procedure, which starts from an initial guess and continually improves the solution in every iteration. The iteration loop is stopped when some prescribed condition is fulfilled. In order to improve the convergence rate, the equations' system can be preconditioned, i.e. multiplied by a suitable preconditioning matrix. In this study, for symmetric matrices, the Preconditioned Conjugate Gradient (PCG) solver with Diagonal-based Incomplete Cholesky (DIC) preconditioner is used. In the case of asymmetric matrices the Preconditioned Bi-Conjugate Gradient (PBiCG) with Diagonal-based Incomplete Lower-Upper (DILU) preconditioner is adopted, OpenCFD [2012].

2.1.6- Wave generation and absorption

In numerical wave tank (NWT) which is used to study wave-body interaction, the wave flows require a domain with open boundaries in order to let the incoming waves enter and the outgoing waves leave the domain undisturbed to keep accuracy and stability of simulation. The standard release of OpenFOAM® does not support wave generation. Three toolboxes for wave generation based on the interFoam solver are currently available in the literature for OpenFOAM: 1-GroovyBC, part of swak4Foam [OpenCFD 2012], 2- waves2Foam, Jacobsen et.al.[2012] and 3-IHFOAM, Higuera et.al.[2013], where the last one is adopted in this study. IHFOAM has been coded from scratch to realistically generate waves at a fixed inflow boundary of the domain by means of special Dirichlet-type (i.e. fixed value) boundary conditions, based on any wave theory formulation from potential flow solution. Wave theories provide mathematical expressions for free surface elevation, particle velocity or

pressure along the water column at the inflow boundary. Generally, free surface elevation, through the VOF function values and the 3 components of the velocity vector are specified at the inlet, while the pressure is extrapolated from the interior of the domain and it is set to zero normal gradients (*buoyantPressure*) at inlet boundary. A more detailed discussion on the numerical implementation of the selected method is referred to (Higuera et.al.[2013]).

According to Le Méhauté [1976], the moderate and high steep regular, non-breaking waves, require wave generation with the 5th-order Stokes theory. Therefore the 5th-order Stokes wave theory, presented in Skjelbreia and Hendrickson [1960], is used in all the simulations at the fixed inlet wave boundary. The two-dimensional analytical expression of the free surface elevation and velocities of incident wave water particles in x- and z- directions for the deep-water condition are given by:

$$\begin{aligned}\eta(x,t) &= \frac{1}{k} \sum_{n=1}^5 b_n \cos(n\theta) \\ u &= \sum_{n=1}^5 a_n \cosh(nkz) \cos(n\theta) \\ w &= \sum_{n=1}^5 a_n \sinh(nkz) \sin(n\theta)\end{aligned}\tag{2.15}$$

Where ($\theta = kx - \omega t$), phase angle, (n), number of frequency components, (k, ω), wave number and wave angular frequency, (t) the time, (x), the left to right Cartesian coordinate which coincides with the mean height of the wave, (z), the Cartesian coordinate in the upward vertical direction with ($z = 0$) being the still water level. The coefficients (a_n) and (b_n) are given in Skjelbreia and Hendrickson [1960].

At the outlet the energy flux, traveling with the wave, has to leave the domain undisturbed, if not, the spurious wave reflections will affect the incident wave upstream and the basic parameters of the waves, giving misleading results. IHFOAM active wave absorption is based on shallow water equation which is just capable of absorbing small amplitude waves. Consequently, in this work, a passive absorbing method of the so-called numerical beach in combination with IHFOAM active wave absorption at outlet boundary is used. This numerical beach includes a coarse mesh domain, the dissipation zone, with increasing the horizontal size of the cells in a direction to the outlet boundaries. It is applied to increase the numerical diffusion for the normal velocity components and the volume fraction. This results in strong dissipation of wave energy within the domain before they

reach the outlet boundary. It should be noted that the mesh has to be controlled to be coarse enough to damp the waves. The pressure is set to zero normal gradients (*buoyantPressure*) at the outlet boundary.

2.1.7- Boundary and initial conditions

The Numerical Wave Tank which is used to study wave-body interaction can be assumed as a closed rectangular domain with a body inside. it includes 7 boundaries that named after their physical representation as Inlet (1), Outlet (3), Bottom (1), Top (1) and Body (1). Each of the geometrical boundaries requires a set of numerical type boundary conditions to specify the boundary data for each of the flow variables including the phase fraction (α), Velocity (\mathbf{U}), and Pressure (p). The two important boundaries of the inlet and outlet have been described in section. 2.1.6. The top boundary of the computational domain is free to the atmosphere which is assumed an open surface (patch). On this boundary, a generic outflow condition of *inletOutlet* is applied to the phase fraction. In the case of velocity, the *pressureInletOutletVelocity* condition (value of zero in this study) is used on the top boundary. The *totalpressure* condition is a *fixedValue* condition which is applied to the pressure (p) on the top boundary.

In this work, bottom and body boundaries are assumed fixed solid and impermeable. Therefore they are set wall boundary by geometry. The fluid velocity at all fluid-solid boundaries are equal to the velocity of the solid boundary, consequently, as the wall boundaries are fixed, the no-slip boundary condition is used. In the case of bottom boundary condition due to deep water assumption, this boundary condition doesn't affect the wave-body interaction, therefore, slip boundary condition is applied. On the bottom and body boundaries for pressure *buoyantPressure*, and in the case of phase fraction the *zeroGradient* boundary condition is applied. The boundary conditions which are used based on OpenFOAM built-in boundary conditions for pressure, phase fraction and velocity fields, are summarized in Table 2.2. For all simulations, a zero-velocity field with no surface waves, and initial hydrostatic pressure distribution are used as an initial condition.

Table 2.2. Summary of the boundary conditions implemented in NWT

	Inlet	Outlet	Top	Bottom	Body
alpha	IH_Waves_InletAlpha	ZeroGradient	inletOutlet	ZeroGradient	ZeroGradient
p_rgh	buoyantPressure	buoyantPressure	totalPressure	buoyantPressure	buoyantPressure
U	IH_Waves_InletVelocity	IH_3D_2DAbsorption_InletVelocity	pressureInletOutletVelocity	slip	fixedValue

The interFoam solver includes modeling of surface tension and can include wall adhesion at the contact point between the interface and wall surface. Wall adhesion models can be applied through a special boundary condition on the phase fraction, (α) field, e.g. the *constantAlphaContactAngle* boundary condition, which requires the user to specify a static contact angle, (θ_0). Therefore, in this work, with regard to the assumption of the solid wall for geometrical bottom and body boundaries, the implication of *zeroGradient* boundary condition for phase fraction, (α), is equal to set the static contact angle, ($\theta_0 = 90^\circ$) which numerically ignores the surface tension effect between the wall and interface, OpenCFD [2012].

2.1.8- Solver settings

Accurate wave generation requires at least a second-order time integration method, Muzaferija and Peric, [1997]. In the case of wave-structure interaction processes, second-order methods are accurate and less diffusive but for stability, it is required that the wave propagates less than half a cell per time step which is equal to Courant number ($Co < 0.5$). In addition, the preliminary simulations in two-dimensional NWT by author with interFoam indicate that: 1-the explicit method of MULES, 2-growth of spurious velocities in low density fluid (here air) near the interface, 3-appropriate mesh refinement around both free surface and given body results in a strict Courant number limit which means very small time steps requirement. As a result in this thesis, considering a fixed time step for the entire simulation time, to assure stable and robust simulation of waves with reasonably accurate wave kinematics, constant shape during propagation along the tank without occurrence of wiggles (which in time grow and sometimes lead to breaking.) or smearing specifically at wave crest and avoid wave height damping and eventually probing the correct wave

specification, the maximum Courant number for the solver, (Co_{max}), and for the free surface, ($alphaCo$), are kept smaller than 0.2.

The flow is initialized with the theoretical solution and the wave field reaches a periodic and stationary state. Therefore a time window is used to avoid inclusion of any spurious results which could occur at the beginning of the test. Excluding the mean of the measured wave elevation time histories, the harmonics at each wave probes are calculated utilizing Fourier series over a time window of the last 10 wave periods. Throughout the simulation, data from individual wave probes are sampled at 50 Hz to ensure capturing all the wave features through propagation. In the following simulations, the surface tension coefficient is set to ($\sigma = 0.07 \text{ N/m}$), the water is assigned density ($\rho_{water} = 10^3 \text{ kg/m}^3$) and kinematic viscosity ($\nu_{water} = 10^{-6} \text{ m}^2/\text{s}$) while the air is assigned density ($\rho_{air} = 1 \text{ kg/m}^3$) and kinematic viscosity ($\nu_{air} = 1.48 \times 10^{-5} \text{ m}^2/\text{s}$). In a post-processing step, the vertical coordinates where the iso-contour of phase fraction of ($\alpha = 0.5$) is taken to be the position of the free surface interface at each time step.

2.1.9- Numerical calculation of wave forces on the cylinder

The total wave force acting on the body is calculated by integrating the pressure and the normal component of shear stress around the surface of the body as follows:

$$F = \int_{\Omega} (-\vec{n}\mathbf{P} + \vec{n} \cdot \vec{\tau}) d\Omega \quad 2.16$$

where (\vec{n}) is the unit normal vector pointing into the fluid, ($\vec{\tau}$) is the viscous stress tensor, (\mathbf{P}) is the combination of hydrostatic and dynamic pressure and (Ω) is the surface of the body. The integration is performed in a discrete manner, by using (\mathbf{P}) and ($\vec{\tau}$) for each cell surface of the body.

2.2- Potential flow Model

2.2.1- Governing Equation

The wave-body interaction is classically studied, using potential flow theory. It is developed based on the assumption that the fluid surrounding the body is inviscid, irrotational, homogeneous and incompressible and with negligible surface tension. The flow is then described by means of a scalar velocity potential ($\phi(x, y, z, t)$) that satisfies the Laplace equation, Eqn. (2.17) and boundary conditions in the fluid domain.

$$\nabla^2 \phi(x, y, z, t) = 0 \rightarrow \Omega \quad 2.17$$

The potentials are defined relative to the earth-bound coordinate system. The Cartesian coordinate system is illustrated in Fig.2.1, where the x-axis is in the negative direction of incoming waves and z-axis directed upwards from an origin at the mean water level which coincides with the axis of the cylinder.

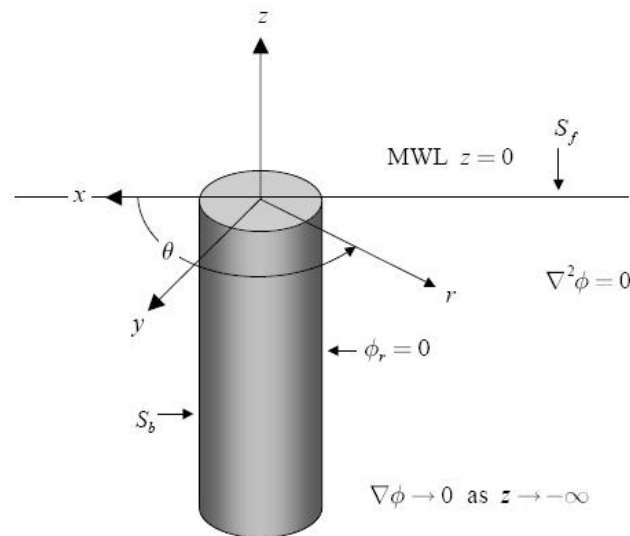


Fig 2.1. Definition sketch of BVP for a vertical cylinder in cylindrical coordinates

2.2.2- Boundary conditions

The fluid domain is bounded by:

- 1- The surface of the body (S_b)
- 2- The free surface (S_f)

3- The domain with an infinite extension (S_∞)

4- The sea-bed (S_s)

A kinematic boundary condition is applied to all solid boundaries. As there is no fluid going through the solid, it requires that the normal velocities of the fluid and solid to be equal at the boundary.

$$\underbrace{\frac{\partial \phi}{\partial n}}_{(S_B)} = 0 \quad 2.18$$

$$\underbrace{\frac{\partial \phi}{\partial Z}}_{(S_s)} = 0 \rightarrow Z = -d \quad 2.19$$

Where the normal vector \vec{n} is positive into the fluid domain and d is the water depth in the fixed coordinate system.

A far-field radiation boundary condition must be imposed on the scattered wave field to ensure that the solutions for free cylindrical waves, radiate outward away from the body and is vanished. Sommerfeld (1949) gives this condition as

$$\lim_{R \rightarrow -\infty} \sqrt{R} \left(\frac{\partial \phi}{\partial R} - i\hat{k}\phi \right) = 0 \quad 2.20$$

Where: $R = \sqrt{x^2 + y^2}$ is the radial distance from the origin of inertia frame and (\hat{k}) is the scattered wave number which may differ from that of the incident wave.

In order to derive the boundary condition at the mean free surface, with surface tension effects neglected, two principal dynamic and kinematic boundary conditions are defined. The displacement of the free-surface from its mean position is denoted by $(\zeta(x, y, t))$. In the case of the kinematic free surface boundary condition, Eqn (2.21 & 2.22), it is assumed that the velocity component of the fluid normal to the free surface is equal to the velocity of the surface in the same direction. The dynamic free surface boundary condition boundary condition, Eqn (2.22), states the (unknown) free surface is a surface of constant pressure.

$$\left. \frac{\partial \phi}{\partial z} \right|_{z=\zeta} - \frac{\partial \zeta}{\partial t} - \left. \frac{\partial \phi}{\partial x} \frac{\partial \zeta}{\partial x} \right|_{z=\zeta} = 0 \quad 2.21$$

$$\left. \frac{\partial \phi}{\partial t} \right|_{z=\zeta} + \left. \frac{1}{2} |\nabla \phi|^2 \right|_{z=\zeta} + gZ \Big|_{z=\zeta} = 0 \quad 2.22$$

Where $\left(\frac{D}{Dt} \right)$ the material derivative and p is the pressure in the fluid, relative to atmospheric pressure, defined by the Bernoulli equation. The combination of the dynamic and kinematic boundary conditions at the exact free-surface position results in the combined free-surface boundary condition, given by:

$$\left. \phi_{tt} \right|_{z=\zeta} + g \left. \phi_z \right|_{z=\zeta} = -2 \nabla \phi \cdot \nabla \left. \phi_t \right|_{z=\zeta} + \left. -\frac{1}{2} \nabla \phi \cdot \nabla (\nabla \phi)^2 \right|_{z=\zeta} \quad 2.23$$

The conditions for the free surface have nonlinear character; because the velocity potential function and its derivatives have to be evaluated at the free surface which is an unknown of the problem.

2.2.3- Solving boundary value problem

Obtaining an approximate solution of this boundary value problem, one must deal with the nonlinear free-surface boundary condition, Eqn (2.23), at the air-water interface. In the context of ocean waves in water of intermediate to large depth, the Stokes perturbation scheme coupled with a Taylor series expansion (linear theory) is commonly employed. The advantage of this scheme is to reduce the complexity of the free surface boundary conditions in the BVP. Stokes scheme is generally referred to as a small-amplitude approximation. For this purpose, all quantities such as the velocity potential, $(\phi(x, y, z, t))$, and free surface elevation, $(\zeta(x, y, t))$ and hydrodynamic forces, are assumed to vary only very slightly relative to some initial static value. They are all expanded in a convergent power series, Eqn. (2.24), with respect to the small non-dimensional perturbation parameter (ε) which denotes the order of oscillation. The parameter (ε) is commonly defined as the incident wave steepness (kA_0) , where k is the linear wave number and (A_0) is typically the first harmonic amplitude of the incident wave.

$$X = \sum \varepsilon^n X^{(n)} = X^{(0)} + \varepsilon X^{(1)} + \varepsilon^2 X^{(2)} + o(\varepsilon^3) \quad 2.24$$

Where $(X^{(0)})$ denotes the mean value, $(X^{(1)})$ and $(X^{(2)})$ indicate the linear or first and second- order, respectively.

Since the location of the water surface is unknown, with the assumption of the small displacement of the free-surface, a Taylor series expansion can be used to transfer the boundary conditions at the exact free-surface position $(z = \eta(x, y, t))$ to the undisturbed mean free-surface position $(z = 0)$.

$$f(x, y, \zeta, t) = f(x, y, 0, t) + \zeta \frac{\partial}{\partial z} f(x, y, z, t) \Big|_{z=0} + \frac{1}{2} \zeta^2 f(x, y, z, t) \Big|_{z=0} \quad 2.25$$

Considering nonlinearity until second order, the Stokes scheme leads to the decomposition of the otherwise nonlinear boundary value problem to a set of two linear boundary value problems. Both the first and the second order potentials must satisfy the Laplace equation everywhere within the fluid domain (Ω) and fulfill with appropriate boundary conditions.

Importantly, to find the solution of the second-order potential $(\phi^{(2)})$ that meets the second-order free surface boundary condition, we must first solve the first-order problem to find potential $(\phi^{(1)})$. Therefore it can be said that solving the problem of second order is forced by the linear solution. At each order, the boundary-value problem is linear and we can decompose the total first-order velocity potential $(\phi^{(1)})$ into three wave components as follows:

$$\phi^{(1)} = \phi_I^{(1)} + \phi_S^{(1)} + \phi_R^{(1)} \quad 2.26$$

where, $(\phi_I^{(1)})$, is 1st-order incident wave potential, $(\phi_S^{(1)})$, is 1st-order scattered wave potential and, $(\phi_R^{(1)})$, is 1st-order radiation wave potential. The first-order boundary value problem of wave diffraction of plane waves around large volume structures is a classical problem. It is solved numerically using the boundary element method. But in the case of the

circular cylinder there exist some analytical solution by Havelock, [1940] for deep water and then by McCamy and Fuchs,[1954] for finite water depth.

In the case of interaction of incoming waves and fixed body which is the case in this study, $(\phi_R^{(1)} = 0)$ the velocity potential is separated into the incident and scattered wave components. The superposition of these two contributions is defined as total diffraction velocity potential $(\phi_D^{(1)})$.

$$\phi_S^{(1)} = \phi_I^{(1)} + \phi_D^{(1)} \quad 2.27$$

In order to solve the second order BVP, second-order potential $(\phi^{(2)})$ and nonlinear forcing terms are necessary to be calculated. Substituting the complete first-order solution Eqn. (2.24) into the right-hand side of combined free surface boundary condition Eqn. (2.23), the free surface quadratic forcing function (\mathbf{Q}) is obtained. The second order water problem is equivalent to the problem of a forced mechanical oscillation such that two types of wave motions are expected: 1- unique forced oscillations imposed by the applied forcing and 2-free oscillations which correspond to the natural wave modes of the system, Kriebel,[1990]. All the forcing terms are periodic in time and oscillate at twice the frequency of the linear monochromatic waves $(e^{2i\omega t})$.

$$\phi_{tt}^{(2)} + g\phi_z^{(2)} = \mathbf{Q}(x, y, z=0)e^{2i\omega t} = (\mathcal{Q}_{II} + \mathcal{Q}_{SS} + (\mathcal{Q}_{IS} + \mathcal{Q}_{SI}))e^{2i\omega t} \quad 2.28$$

Where three types of forcing may be identified:

- \mathcal{Q}_{II} = due to the self-interaction of the first-order incident waves, which leads to the second-harmonic found in the usual stokes Second-order wave theory
- \mathcal{Q}_{SS} = due to self-interactions of first-order scattered waves
- $\mathcal{Q}_{IS}, \mathcal{Q}_{SI}$ = due to cross-interaction of the first order incident and scattered waves.

The details of these components are given in the following:

$$Q_{II} = i\omega \left[2(\nabla \varphi_I^{(1)})^2 - \varphi_I^{(1)} \varphi_{Izz}^{(1)} + \frac{\omega^2}{g} \varphi_I^{(1)} \varphi_{Iz}^{(1)} \right] \quad 2.29$$

$$Q_{SS} = i\omega \left[2(\nabla \varphi_S^{(1)})^2 - \varphi_S^{(1)} \varphi_{Szz}^{(1)} + \frac{\omega^2}{g} \varphi_S^{(1)} \varphi_{Sz}^{(1)} \right] \quad 2.30$$

$$Q_{IS} = i\omega \left[2(\nabla \varphi_I^{(1)})(\nabla \varphi_S^{(1)}) - \varphi_I^{(1)} \varphi_{Szz}^{(1)} + \frac{\omega^2}{g} \varphi_I^{(1)} \varphi_{Sz}^{(1)} \right] \quad 2.31$$

$$Q_{SI} = i\omega \left[2(\nabla \varphi_S^{(1)})(\nabla \varphi_I^{(1)}) - \varphi_S^{(1)} \varphi_{Izz}^{(1)} + \frac{\omega^2}{g} \varphi_S^{(1)} \varphi_{Iz}^{(1)} \right] \quad 2.32$$

In the case of the monochromatic incident wave; we separate the time dependencies explicitly and write:

$$\phi^{(2)} = \Re \left\{ \left(\varphi^{+(2)P} + \varphi^{+(2)H} \right) e^{2i\omega t} \right\} + \left(\varphi^{-(2)P} + \varphi^{-(2)H} \right) \quad 2.33$$

The homogeneous solution, $(\phi^{(2)H})$ represent free wave motions due to the interaction of the forced waves with the fixed cylinder. These solutions must satisfy the Laplace equation, the bottom boundary condition, and the non-homogeneous free surface boundary condition.

$$\frac{\partial^2 \phi_D^{(2)}}{\partial t^2} + g \frac{\partial \phi_D^{(2)}}{\partial z} = 0 \Rightarrow z = 0 \quad 2.34$$

The second order diffracted potential $(\phi_D^{(2)})$ represents the scattering of the second order incident waves in the presence of the inhomogeneous boundary condition on the free surface. These free waves must satisfy the following dispersion relationship at second order.

$$4\omega^2 = gk_2 \tanh(k_2 h) \quad 2.35$$

Where k_2 is the wave number of free waves oscillating at the frequency 2ω . Depending on water depth, k_2 varies from $2k$ (shallow) to $4k$ (deep).

As the second-order free surface boundary condition is non-homogeneous therefore the numerical discretization of the surface free is required to calculate the particular solution $(\phi^{(2)P})$. The particular solutions represent forced wave motions due to the nonlinear interactions of the first-order incident and scattered waves. Forced waves are phase-locked

and propagate at twice the angular frequency (2ω) and twice the wave number ($2k$) of the first-order carrier waves. The particular solution must satisfy the Laplace equation, the bottom boundary condition, and the non-homogeneous free surface boundary condition and may be further separated as:

$$\phi^{(2)P} = \phi_{II}^{(2)} + \phi_{DD}^{(2)} + \left(\phi_{ID}^{(2)} + \phi_{DI}^{(2)} \right) \quad 2.36$$

If the particular and homogeneous solution substitute in Eqn. (2.33) the total second-order potential $\left(\phi^{(2)} \right)$ is given by:

$$\phi^{(2)} = \phi_D^{(2)} + \left[\phi_{II}^{(2)} + \phi_{DD}^{(2)} + \left(\phi_{ID}^{(2)} + \phi_{DI}^{(2)} \right) \right] \quad 2.37$$

The sum of the last four components can be introduced as second-order pseudo-incident wave potential $\left(\phi_I^{(2)} \right)$ that is equivalent of the first-order undisturbed incoming wave potential $\left(\phi_I^{(1)} \right)$ so that we can write:

$$\phi^{(2)} = \phi_D^{(2)} + \phi_I^{(2)} \quad 2.38$$

For the purpose of this study, we will consider plane progressive waves in deep water. According to the theory of Stokes, the profile of a surface gravity wave traveling in a positive x-direction can in a second-order perturbation be formulated as

$$\zeta(x, t) = \zeta^{(1)}(x, t) + \zeta^{(2)}(x, t) + O(kA^3) \quad 2.39$$

Where

$$\zeta(x, t) = \zeta^{(1)}(x, t) + \zeta^{(2)}(x, t) \quad 2.40$$

$$\zeta^{(1)}(x, t) = A_0 \exp[j(\omega t - kx)] \quad 2.41$$

$$\zeta^{(2)}(x, t) = \frac{1}{2} k A_0^2 \exp[2j(\omega t - kx)] \quad 2.42$$

When the progressive wave described by Eqn. (2.39) approaches on a surface piercing cylinder in a fluid domain of an infinite horizontal extent, the resulting expression for the

free-surface elevation of the fluid domain surrounding the body, correct to second-order in kA for a monochromatic incident wave, is given by

$$\eta^{tot}(x, y, t) = \Re\{\eta^{(1)}(x, y, t) + \eta^{(2)}(x, y, t)\} \quad 2.43$$

$$\eta^{(2)}(x, y, t) = \eta_{21}^{(2)}(x, y, t) + \eta_{22}^{(2)}(x, y, t) = \eta^{(2+)}(x, y, t) + \eta^{(2-)}(x, y, t) \quad 2.44$$

where $\eta(x, y, t)$ the function of spatial position of time, $\eta^{(1)}$ is of $O(\varepsilon)$ while $\eta^{(2+)}$ and $\eta^{(2-)}$ are of $O(\varepsilon^2)$ and represent the mean (difference-frequency) and sum-frequency (double) harmonic components, respectively. The term $\eta^{(2-)}(x, y, t) = \bar{\eta}^{(2)}(x, y, t)$ is time independent and of second-order in origin. It is often referred to as the mean free-surface elevation or mean set-up/down, of which there are two principal contributions: the quadratic self-interaction of $\phi^{(1)}$ in the Bernoulli equation applied at the mean free-surface position; and the perturbation of $\phi^{(1)}$ and $\eta^{(1)}$ to $O(\varepsilon^2)$. The term $\eta^{(2+)}$ which oscillates at (2ω) contains contribution from these two effects and also an additional contribution from $\phi^{(2)}$. The term $\eta^{(1)}$ is the first-order free-surface elevation operating at the fundamental incident wave frequency.

Once the velocity potentials are obtained, here numerically by means of (WAMIT, 1995), then theoretical estimates of the complex, non-dimensional format of the mean value, first and second order of the disturbed elevation are defined as follow:

$$RAO(x, y) = \frac{A^{(1)}(x, y)}{A_0}, \text{1st-order} \quad 2.45$$

$$QTF^{(+)}(x, y) = \frac{A^{(2+)}(x, y) \times a}{A_0^2}, \text{2nd-order} \quad 2.46$$

$$QTF^{(-)}(x, y) = \frac{A^{(2-)}(x, y) \times a}{A_0^2}, \text{mean value} \quad 2.47$$

Where a is the radius of the column, A_0 is the first-harmonic amplitude of the incident (undisturbed) wave, $A^{(1)}$ and $A^{(2+)}$ are the first- and second harmonic amplitudes of the

disturbed elevation by the column, respectively, and $A^{(2-)}$ is the mean set-up/down. The individual terms identified in Eqn. (2.43 & 2.44) are then formulated as follow:

$$\eta^{(1)}(x, y, t) = -\frac{1}{g} [\phi_t^{(1)}] = \zeta^{(1)}(0, t) RAO(x, y) \quad 2.48$$

$$\begin{aligned} \eta_{21}^{(2)}(x, y, t) &= -\frac{1}{g} \left[\eta^{(1)} \phi_{tz}^{(1)} + \frac{1}{2} \left[(\phi_x^{(1)})^2 + (\phi_z^{(1)})^2 \right] \right] \\ &= [\zeta^{(1)}(0, t)]^2 QTF^{(+)}(x, y) \end{aligned} \quad 2.49$$

$$\eta_{22}^{(2)}(x, y, t) = -\frac{1}{g} [\phi_t^{(2)}] = A_0^2 QTF^{(-)}(x, y) \quad 2.50$$

Chapter 3

Grid refinement study and Validation

In chapter 2, it was explained that the study of wave scattering and amplification around the cylinder is carried out through a numerical approach by two numerical model based on Navier-Stokes equations and potential flow theory. Before performing the main simulation and analysis, the efficiency and accuracy of both numerical models should be assessed. In section 3.1, the dimensionless parameters that affect the wave run up around the cylinder and also the selected wave conditions for the necessary simulations in this work are presented. Then, the accuracy of the numerical model is evaluated via convergence study of wave interaction with vertical cylinder by Navier-stokes model in section 3.2. In the case of the potential-flow model, the accuracy of the numerical model considering both the body and the free surface mesh is verified through a convergence study which is given in section 3.3. Then the converged solution by both of the numerical models is validated in section 3.4 for wave elevation and wave forces during the wave-structure interaction.

3.1- Dimensionless parameters and wave conditions

In this thesis, the benchmark experiments provided by ITTC (OEC),[2013] is employed, primarily, for validation purpose, and then to investigate the importance of high-frequency wave scattering Type 1&2 and also progressive lateral edge waves on nonlinear wave field around a single cylinder. Hence, following the wave conditions and body specifications by the mentioned experiments and also correctly representing wave effects, all of the simulations in this work are performed in the model scale of ($\gamma=1/50.314$) based on the Froude similitudes with the assumption of constant gravity acceleration and also air and water fluid properties. Wave scattering and wave run-up on monopiles or columns are influenced by the structure, bed and wave characteristics. Consequently, the physics of the problem involves the interaction of single surface piercing cylinder with surface gravity incident waves which

are propagating over a flat bed in an unbounded domain. The cylinder is considered as smooth, rigid, vertical, body with a circular cross-section and the incident waves are assumed non-breaking, regular, long-crested and unidirectional fifth-order Stokes waves. Following the dimensional analysis procedure, the wave run-up height can be considered a function of the following ten physical dimensional parameters:

$$R_u = f(\rho, g, \mu, \sigma, A, L, T, U_m, h, a) \quad \text{Equation 3.1}$$

Where (R_u) , wave run-up height, (ρ) , fluid density, (μ) , dynamic viscosity, (σ) , the water-air interface surface tension, (g) , gravity acceleration, (A) , wave amplitude, (T) , wave period, (L) , wavelength, (U_m) , maximum horizontal velocity of water particles at wave crest, (h) , still water depth, (a) , the half of characteristic horizontal length normal to the incident wave direction. Dimensional analysis indicates that the wave run-up height can then be expressed as a function of totally seven effective, physically meaningful non-dimensional parameters.

$$\frac{R_u}{A} = f(ka, kA, KC, Re, Fr, kh, We) \quad \text{Equation 3.2}$$

Where (R_u/A) , relative wave run-up, $(ka=2\pi a/L)$, wave diffraction parameter, $(kA=2\pi A/L = \pi H/L)$, wave steepness parameter, $(KC=\pi A/a)$, Keulegan-Carpenter number, $(Re=2\rho U_m a/\mu)$, Reynolds number, $(Fr=U_m/\sqrt{2ga})$, Froude number, $(kh=2\pi h/L)$, relative water depth number and, $(We=U_m\sqrt{2\rho a/\sigma})$, Weber number.

In this work, with the assumption of fixed radius circular cylinder, the simulations related to study the effect of incident wavelength on wave field surrounding the cylinder for three distinct wave periods of $(T=7s, 9s \text{ and } 15s)$ are labeled as short, intermediate and long wave cases, respectively. In addition, the effect of a change in wave steepness, (kA) , on wave run-up around the cylinder is also investigated. Thus three incident wave steepness of $(H/L=1/30, \text{ small steep}), (H/L=1/16, \text{ moderate steep})$ and $(H/L=1/10, \text{ high steep})$ are considered for these simulations. Here, the validation is carried out for short and long waves with three wave steepness of $(H/L=1/30, 1/16 \text{ and } 1/10)$. For the purpose of this study, the water depth is

assumed deep and the restriction of $(kh \gg 1)$ is made. This essentially implies that finite depth effects will not interfere with the free-surface motion and therefore the wave run-up will consist purely of wave-structure interaction effects.

Table 3.1, summarizes simulations and wave conditions which are used in this study. A graphical representation of the given wave conditions based on wave force regimes and wave theories graph is also shown in Fig.3.1. Considering the same Froude number at full and model scales, the (Re) number is smaller at model scale with a factor of $(\gamma^{3/2})$. Based on Table 3, the (Re) number varies in the order of $(10^5 \text{ and } 10^7)$ for both full and scale models which indicates the flow regime for steady flow interacting a circular cylinder is already turbulent and the friction effects are negligible. For (Fr) number which varies in the range of (0.015) to (0.126) , the value is very small for steady flow which indicates that gravity effects are dominant. It also suggests that there is small free surface amplification that can be neglected. According to Fig.3.1, for each pair of (ka) and (kA) , there is a corresponding (KC) number that governs the related free surface phenomenon in oscillatory flow. Here, with regard to the given wave conditions, the (KC) number varies in the range of $(0.5-7)$. For large (KC) numbers, the water particles travel quite large distances relative to the total width of the cylinder, which leads to boundary layer separation and vortex formation. For small (KC) numbers, separation behind the cylinder doesn't occur and the inertia or diffraction effects will dominate, Sumer and Fredsøe [2006]. Since the wave flow is a non-uniform oscillatory flow with a free surface in both horizontal and vertical plane, the (KC) number governs the effect of both (Fr) and (Re) numbers on the wave field surrounding the cylinder and it is investigated in this work, as well. The (We) is sufficiently greater than unity for both full and model scale, therefore, surface tension effect cannot affect the wave run-up around the cylinder. Regarding the range of aforementioned non-dimensional parameters for both full and scale models, it can be concluded the scale effect can be neglected and Froude similitudes is appropriate with respect to the physics of the problem.

Table 3.1. Selected incident wave conditions for Navier-Stokes Solver

Case name	T [s]	H [m]	L [m]	H/L	2a/L	KC	Fr	Re	We
T7S130	7	2.548	76.44	1/30	0.210	0.5003	0.015	Full: 0.3004E+007	Full: 89.7637
				Model: 0.1841E+005				Model: 1.7841	
T7S116	7	4.777	76.44	1/16	0.210	0.9381	0.031	Full: 0.6186E+007	Full: 184.8623
				Model: 0.1733E+005				Model: 3.6742	
T7S110	7	7.644	76.44	1/10	0.210	1.5009	0.056	Full: 1.1265E+007	Full: 336.6103
				Model: 0.3156E+005				Model: 6.6902	
T9S116	9	7.91	126.36	1/16	0.13	1.5508	0.076	Full: 1.1342E+007	Full: 234.4273
				Model: 0.3178E+005				Model: 4.6593	
T15S130	15	11.700	351.00	1/30	0.046	2.2973	0.032	Full: 0.6408E+007	Full: 191.4798
				Model: 0.1795E+005				Model: 3.8057	
T15S116	15	21.938	351.00	1/16	0.046	4.3074	0.065	Full: 1.3022E+007	Full: 389.1055
				Model: 0.3648E+005				Model: 7.7335	
T15S110	15	35.100	351.00	1/10	0.046	6.8919	0.126	Full: 2.5323E+007	Full: 756.6570
				Model: 0.7095E+005				Model: 15.0387	

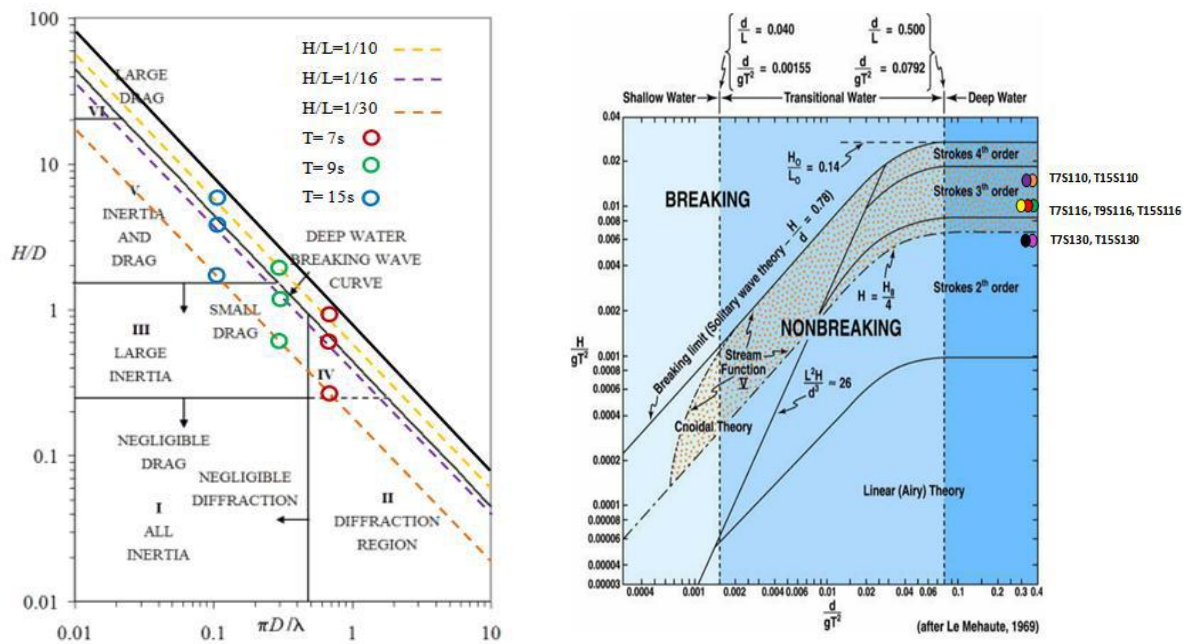


Fig 3.1. Different wave force regimes, (Chakrabarti, 1987), (left), Validity of wave theories graph, Le Méhauté (1976), (right).

3.2- Convergence study of the wave interaction with a single cylinder by Navier-stokes model

In the Navier–Stokes model, the accuracy of wave-structure interaction simulations, primarily, depending on the capability of the numerical model for the correct representation of the waves that reach the structure. Therefore having an appropriate NWT that can provide accurate wave generation and propagation with small numerical dissipation and dispersion is necessary. In this study propagation of plane progressive waves in deep water in the positive x-axis is considered. A single, truncated, vertical surface piercing cylinder with circular cross-section is used for convergence study purpose. The main particulars of the cylinder are listed in Table.3.2.

Table 3.2. Main particulars for single cylinder		
Description	Diameter (D) [m]	Draft [m]
Full scale	16	24 = (1.5D)
Model scale	0.318	0.477
Scale Ratio ($\gamma = \text{Model/Full}$)	1/50.314	

The computational domain dimensions and computational mesh with free-surface plane and symmetry plane are illustrated in Fig.3.2&3.3. Since there is no obstacle or other change in geometry along the tank, no wave transformation should take place and the wave should maintain incident wave shape and specifications during propagation along the tank. The whole computational domain is discretized by blocks of hexahedral cells (belonging to the structured mesh) using blockMesh. The steep and high-frequency waves around the body are highly deformed, and propagate in radial directions. Therefore an extra mesh refinement around the body is also necessary besides the free-surface region. The computational domain is divided into two parts, main tank to study the physics of problem and damping zone surrounding the main tank in a horizontal plane to damp these scattered waves and avoid reflections back into the computational domain. The origin of the coordinate system is defined at the bottom left of the corner at the inlet boundary, positive x-axis pointing downstream and z-axis pointing upward. In the case of the body region, the up and downstream length in the x-direction and the main domain half-width in the y-direction is 4D for all cases. The damping zone length in the y-direction is 6D and in the x-direction is 5L. In order to avoid the contamination of the inlet boundary with scattered/reflected waves propagating in the negative x-axis, the size of the wave region in the x-direction is set to 4L.

The assumption of the deep-water condition, the water depth is $1L$ and air-part has the height of $3D$ to minimize the influence of the top boundary condition on the wave.

A fine mesh resolution normal to the free surface is commonly required in regions of free-surface motion to sharply resolve the phase-interface. Thus the domain in the z -direction is divided into four regions. Two regions which include local mesh refinement, are around the free surface, in water and air phase respectively. The other two regions outside the free surface region, are coarsened toward the bottom and top boundaries to save computational effort. The height of region for local mesh refinement, below and above the still water level (STWL), is $1H$ for each region to accommodate for the free surface elevation. In order to record time histories of free surface elevation, an arrangement of wave probes is used. The top view of wave probes at 10 locations in a radial pattern in the vicinity of the cylinder is illustrated in Fig.3.4. The wave probes at distances of $(r/D = 0.513)$ are considered as on-body probes.

Discretisation error is the main source of computational errors which can arise from numerical schemes, mesh style and number used to discretize the equations, boundary conditions, etc. Hence, in this part grid-space and time-step convergence study is carried out to verify the efficiency and accuracy of the NWT and to obtain appropriate wave and body mesh resolution. The uniform and fine wave resolution for the spatial discretization of the domain at the region around the free surface is defined in terms of two parameters, a number of cells per wavelength $(L/\Delta x)$ and number of cells per wave height $(H/\Delta z)$. In the region around the body, two mesh refinement zones are defined. In the inner refinement zone close to the cylinder, where the main part of physics is solved, the body mesh is defined by a number of cells around the cylinder, $(N_{\text{Tangential}})$ and the number of cells in the radial direction $(D/\Delta r_{\text{Refinement1}})$. The outer refinement zone is defined to provide a smooth transition from a wave to the body zone, ensuring tolerable numerical errors in cell interpolations. Accordingly, this mesh is specified by $(D/\Delta r_{\text{Refinement2}} = 0.8 \times D/\Delta r_{\text{Refinement1}})$. Since the mesh is structured and it is a combination of multi-blocks, therefore the number of cells per wave height $(H/\Delta z)$ in the body zone is the same as the wave zone, to respect mesh continuity. Finally, in the rest of the domain, the mesh is coarsened toward the bottom and top boundaries to save computational effort.

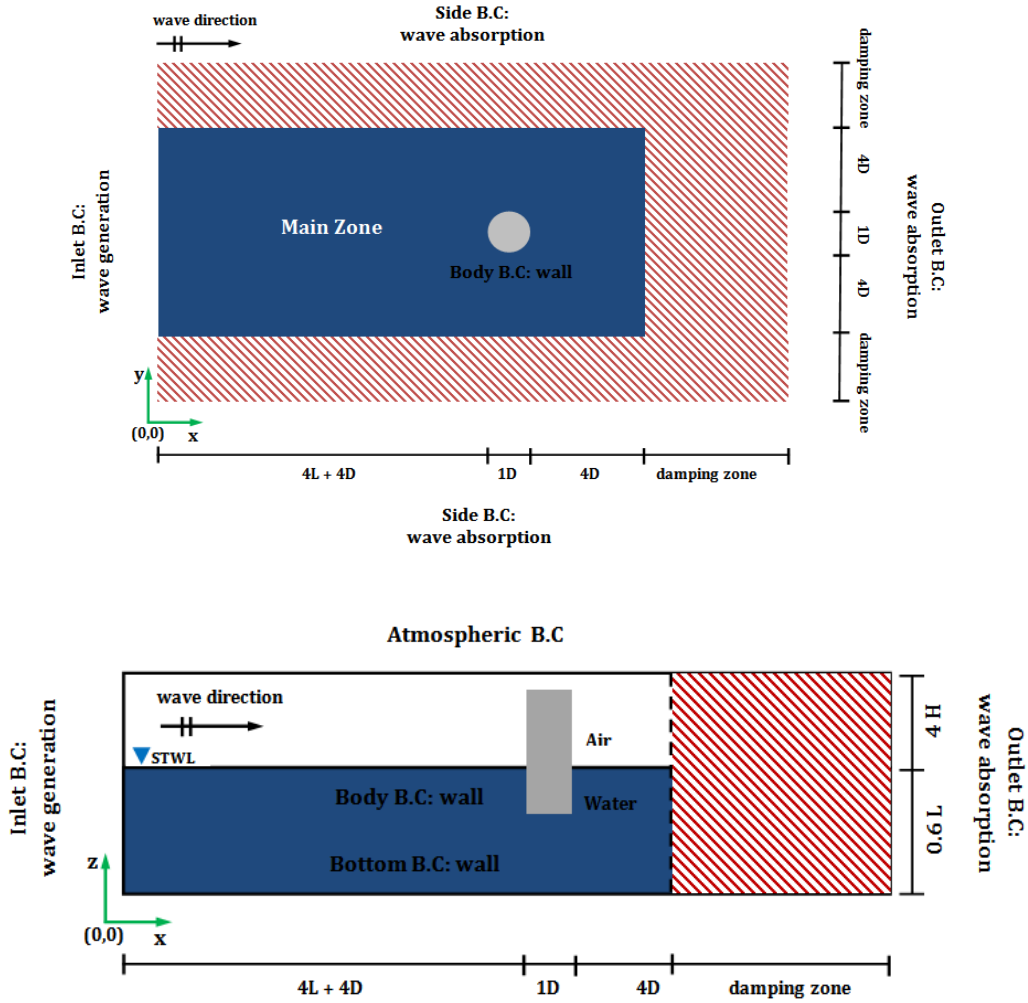


Fig 3.2. Computational domain, geometry, and boundary conditions

The convergence study is carried out for the triple solutions of **Mesh A**, **Mesh B** and **Mesh C**. The refinement factor for both spatial and temporal discretization is set to $(\sqrt{2})$. Since both temporal and spatial discretization schemes are of second order, therefore the refinement factor for time-step is also $(\sqrt{2})$. Table.3.3, summarize the detailed information on wave and body mesh resolution. A regular, fifth-order Stokes wave of the period ($T=7s$) and wave steep-nesses of ($H/L=1/16$) is selected for this study. It is expected that the numerical uncertainties for the other wave conditions are of the same order.

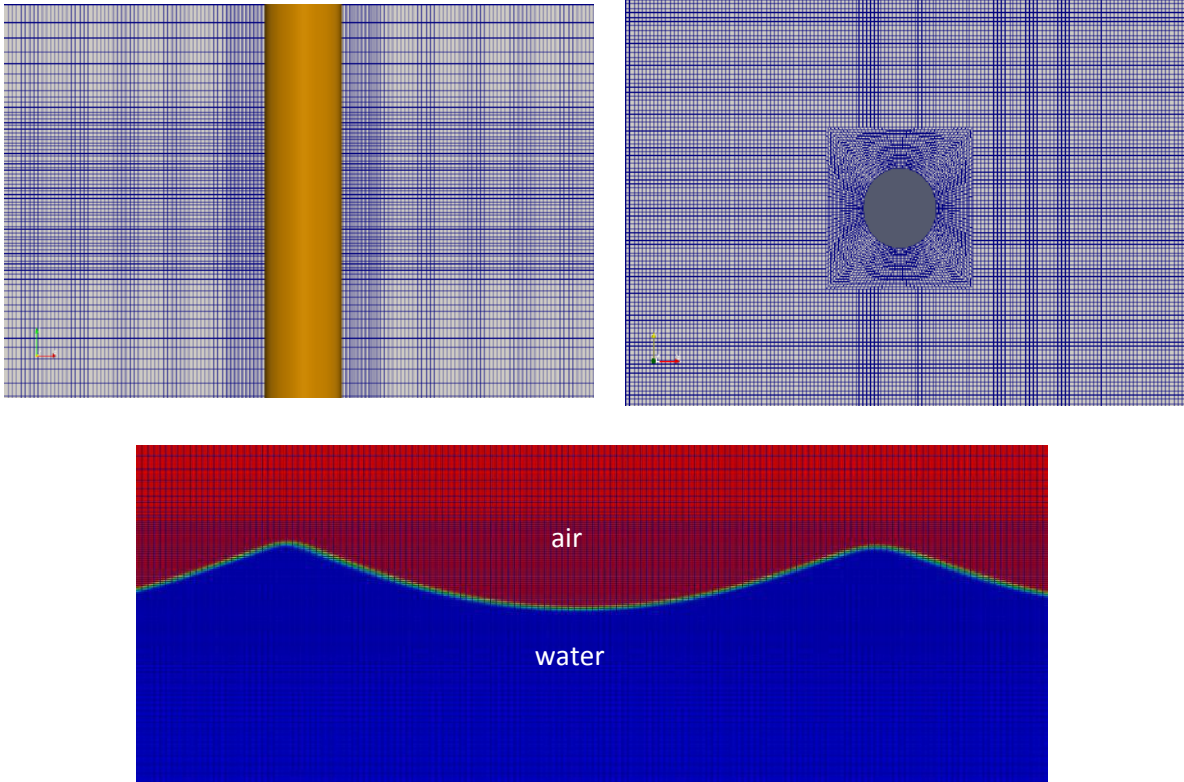


Fig 3.3 Computational Mesh Free-surface plane and Symmetry plane and a cross-section of the refined mesh area around the free surface waves

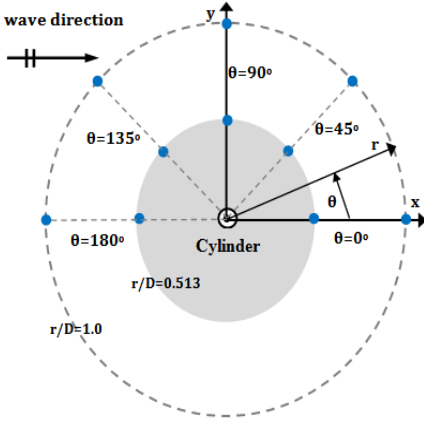


Fig 3.4. Locations of wave probes around the single circular cylinder.

Fig.3.5&3.6 shows the comparison of the normalized time histories of the wave elevation at three wave probes located at the front, shoulder, and back of the cylinder and the wave loads (horizontal and vertical). The wave elevation (η) is normalized by the first-order wave amplitude (A_1) and the simulation time (t) is normalized by the wave period (T). Refinement from Mesh B to Mesh A, the time history of wave elevation coincides with each other while coarsening from Mesh B to Mesh C the difference at both crest and trough is more apparent.

In this work, the analysis of convergence study is performed for the first harmonic of wave elevation and the first harmonic of both horizontal and vertical forces. The convergence condition is assessed through the convergence ratio (R) which is given by:

$$R = \varepsilon_{21} / \varepsilon_{32} \quad \text{Equation 3.3}$$

where the change in the numerical solution between Mesh A and B is denoted as ($\varepsilon_{21} = \varphi_2 - \varphi_1$) and the change between Mesh B and C is denoted as ($\varepsilon_{32} = \varphi_3 - \varphi_2$).

Table 3.3. Spatial and temporal discretization for convergence study of wave interaction with a vertical circular cylinder							
Parameter	$H/\Delta z$	$L/\Delta x$	$D/\Delta r_{\text{Refinement1}}$	$D/\Delta r_{\text{Refinement2}}$	$N_{\text{Tangential}}$	$T/\Delta t$	Total grid points (M)
Mesh A	42	141	72	90	226	17500	13.512
Mesh B	30	100	51	64	160	8750	9.56
Mesh C	22	71	36	46	113	7000	6.75

According to Stern et al.[2001], as the convergence ratio is ($0 < R < 1$) the model is monotonically converging, thus, the Grid Convergence Index (GCI) method is used to predict the discretization error. The details of convergence parameters are illustrated in Table.3.4&3.5, for wave elevation and force components, respectively. Following the procedure for GCI method, the order-of-accuracy (p) for a non-constant refinement ratio ($r_{21} \neq r_{32}$) and triple solutions are calculated by:

$$p = \frac{\ln\left(\frac{\varepsilon_{32}}{\varepsilon_{21}}\right)}{\ln(r_{21})} + \frac{1}{\ln(r_{21})} \left[\ln(r_{32}^p - 1) - \ln(r_{21}^p - 1) \right] \quad \text{Equation 3.4}$$

where the refinement ratio was expressed as the ratio between cell size in any x - or z -direction at the region around the free surface ($r_{21} = \Delta_2/\Delta_1, r_{32} = \Delta_3/\Delta_2$). As mentioned before, the temporal and spatial discretization schemes are of second order by accuracy to provide accurate wave propagation. Therefore the theoretical order of convergence (p) is 2. Finally, the Grid Convergence Index for both (r_{21}) and (r_{32}) is predicted by:

$$GCI^{21} = FS \frac{e_a^{21}}{r_{21} - 1} \quad GCI^{32} = FS \frac{e_a^{32}}{r_{32} - 1} \quad \text{Equation 3.5}$$

where (FS) is the safety factor of the method. The general recommendation states a factor ($FS = 1.25$) if solutions on more than two grids are available, Roache,[1998]. How much the solution of the computed value would change with further refinement can be illustrated with GCI. A small value of GCI percentage shows the computed value is approaching the asymptotic range.

The wave elevation around the cylinder as a local variable is strongly sensitive to the grid change. According to Table.3.4, the results demonstrate that the change in the magnitude is decreased considerably through refinement from a coarse grid to the fine grid. Therefore Mesh B is sufficient for the solution of wave elevation. on the other hand, the wave force as an integrated global variable is less dependent on the mesh resolution. The results for both force components, Table.3.6, reveal that the effects of the grid changes are small for the present range of grid size. This suggests that the convergence has already achieved by Mesh C for the solution of wave force. The calculated (p) values for wave elevation are higher than and for force components are less than the expected value of 2. This indicates errors other than the spatial and temporal error dominate in this numerical model. In order to provide appropriate mesh to achieve a converged solution by wave elevation and wave force, **Mesh set-up B** is selected as an appropriate resolution for all of the future wave-structure studies in this work.

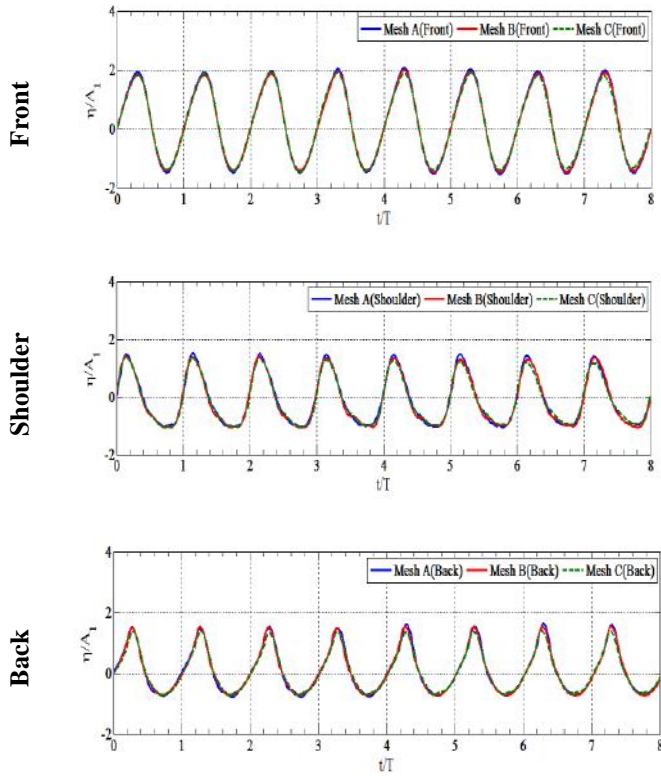


Fig 3.5. Time history of normalized wave elevations at the front, shoulder, and back of the cylinder

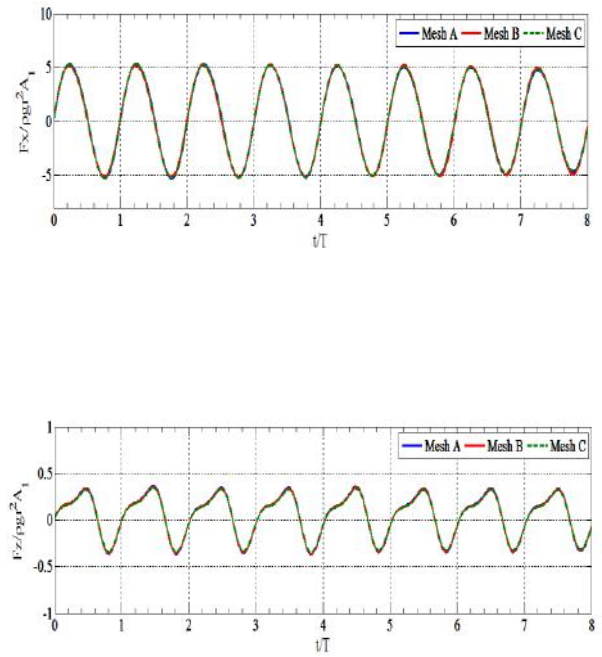


Fig 3.6. Time history of normalized horizontal and vertical wave forces

Table 3.4. Convergence Statics for normalized 1st harmonics of wave elevation

Parameter	Front	Shoulder	Back
	(η_1/A_1)		
Mesh A	1.6866	1.1613	0.9924
Mesh B	1.6643	1.1373	0.9692
Mesh C	1.6067	1.0774	0.9152
ε_{BA}	0.0223	0.0240	0.0231
ε_{CB}	0.0576	0.0599	0.0541
R	0.3871	0.4004	0.4281
P	2.7387	2.6409	2.4479
GCI _{BA} [%]	1.7609	2.0012	2.1656
GCI _{CB} [%]	4.5494	4.9979	5.0586

Table 3.5. Convergence Statics for normalized 1st harmonics of horizontal and vertical wave forces

Parameter	$(F_x^{(1)}/\rho gr^2 A_1)$	$(F_z^{(1)}/\rho gr^2 A_1)$
	Mesh A	5.1562
Mesh B	5.1476	0.2850
Mesh C	5.1335	0.2756
ε_{BA}	0.0087	0.0058
ε_{CB}	0.0141	0.0093
R	0.6156	0.6250
P	1.3999	1.3561
GCI _{BA} [%]	1.7325	1.3561
GCI _{CB} [%]	2.8144	1.9385

3.3- Convergence study of the wave interaction with a cylinder by Potential flow model

The convergence study for the potential-flow model is carried out for the same body arrangement which was used for the Navier-stokes model study. Solving the linear boundary value problem to calculate the mean and first order of wave elevation and wave forces, discretization of the submerged body surface (\mathbf{S}_b) is sufficient. However, to solve the second order problem, the discretization of the free surface (\mathbf{S}_f) is also required. In WAMIT the origin of a fixed coordinate system for one body analysis is located at the middle of the body at ($z=0$), where z-coordinate is positive upward. The free surface surrounding the body is assumed circular and the length scale is set to ($L=1m$). Since only meshes on the surface would be needed by BEM therefore flat quadrilateral panels based on low-order method is used to for discretization purpose. Fig.3.7, shows the computational geometry and mesh for both body and surrounded free surface, respectively. Two-plane of symmetry has been implemented in the numerical model to improve computational efficiency. To avoid the difficulty of calculating coefficients associated with the exterior solid angle and removing the irregular frequencies, meshes are also generated on the inner free surface inside the body.

The free surface resolution must be fine enough in order to resolve the small scales. In addition, the minimum value for the outer radius of the free surface is equal to the corresponding wavelength by half of incident wave period. In this thesis, the outer radius is set to ($2D$). As the values at on-body points are of main interest, therefore the free surface mesh is refined at a narrow region around the cylinder with a thickness of ($0.03D$). The first and second order solution are calculated for the wave probes as is illustrated in Fig.3.4.

Verification of the numerical results by the potential-flow model is performed through systematic convergence studies on the choice of the body and free surface mesh. The body mesh resolution is specified with three parameters of a number of cells around the cylinder, ($\mathbf{N}_{Tangential}$), the number of cells in the radial direction (\mathbf{N}_R) and the number of cells in the vertical direction (\mathbf{N}_z). The free surface has two mesh refinement zones. Therefore the mesh in the inner refinement zone close to the cylinder in the radial direction is defined by (\mathbf{N}_{FR1}) and the mesh in the outer refinement zone with larger extension in the radial direction is defined by (\mathbf{N}_{FR2}). This convergence study is carried out for a regular stokes wave of ($T=7s$)

and the refinement factor for spatial discretization by the body and free surface is set to $(\sqrt{2})$. At the first step, the study is performed for triple Mesh of **B1**, **B2**, and **B3** to find proper body mesh for the first order solution. Table.3.6 summarize the detailed information of these meshes. Table.3.7 illustrates the convergence analysis for the 1st harmonics of wave elevation and also horizontal/vertical wave forces. The results reveal the small change in GCI value from the finer grid (GCI_{21}) to a coarser grid(GCI_{32}). This indicates the convergence has already reached by **Mesh B3**. After the proper choice of body mesh, the convergence study is carried out the to find adequate free surface mesh resolution for a second-order solution. Hence, three mesh set-up of B3Fs1, B3Fs2, and B3Fs3 for the free surface are analyzed. The detailed information of these meshes is given in Table.3.8. The convergence analysis for the 2nd harmonics of wave elevation and also horizontal/vertical wave forces are presented in Table.3.10. The results reveal that variation of second order solution from coarser to the finer grid is small. Therefore the free surface resolution by mesh set-up of B3Fs3 seems sufficient.

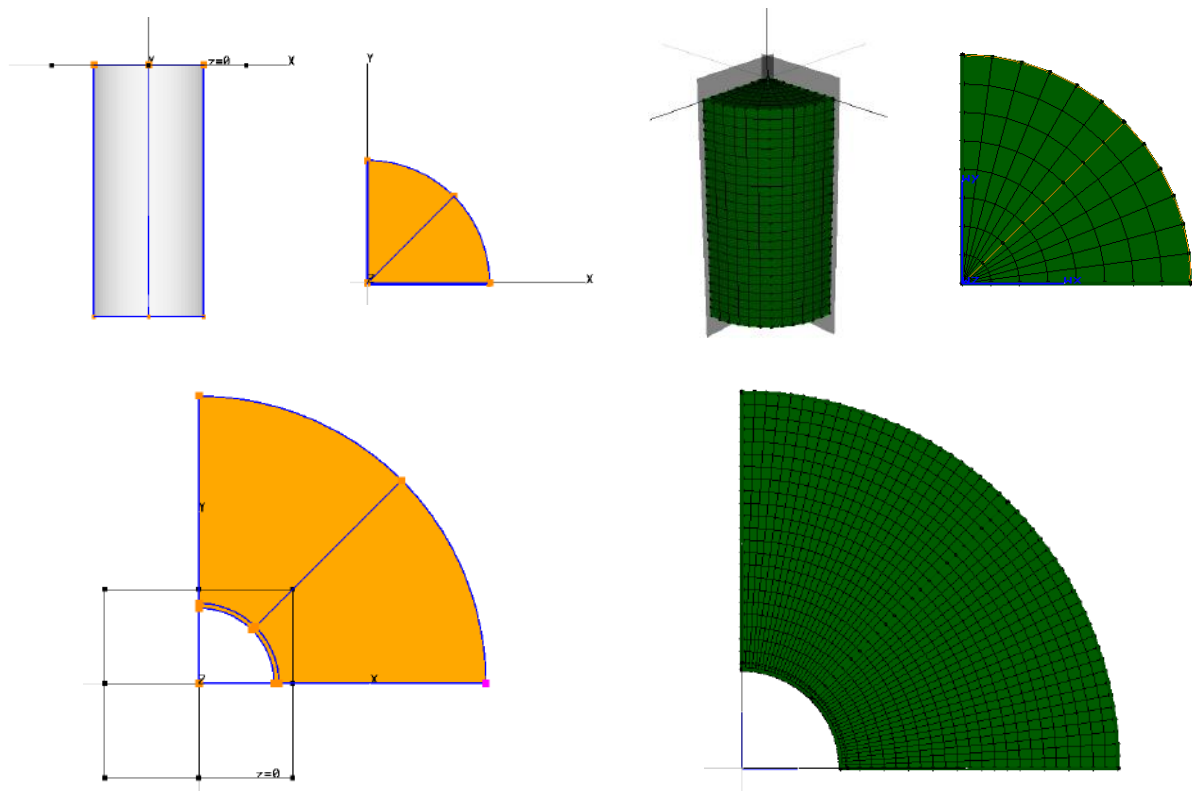


Fig 3.7. Computational geometry and mesh for the body (left), inner free surface (middle) and outer free surface (right)

Table 3.6. Body Mesh resolution (per quadrant)			
Parameter	$N_R = N_{\text{Tangential}}$	N_Z	Total number of grid
Mesh B1	20	48	1760
Mesh B2	14	34	868
Mesh B3	10	24	440

Table 3.7. Convergence study for the first-order solution by body mesh set-up					
Parameter	(η_1/A_1)			$(F_x^{(1)}/\rho g r^2 A_1)$	$(F_z^{(1)}/\rho g r^2 A_1)$
	Front	Shoulder	Back		
Mesh 1	1.6301	1.0172	0.9751	4.9364	0.2636
Mesh 2	1.6337	1.0173	0.9766	4.9345	0.2630
Mesh 3	1.6387	1.0175	0.9786	4.9319	0.2622
ε_{21}	0.0036	0.0001	0.0015	0.0019	0.0006
ε_{32}	0.005	0.000135	0.0020	0.0026	0.0008
R	0.7200	0.7407	0.7500	0.7308	0.7500
P	0.9479	0.8659	0.8301	0.9050	0.8301
GCI_{21} [%]	1.1571	0.0357	0.5625	0.6446	0.2250
GCI_{32} [%]	1.6071	0.0482	0.7500	0.8821	0.3000

Table 3.8. Free surface mesh resolution (per quadrant)				
Parameters	$N_{\text{Tangential}}$	N_{FR1}	N_{FR2}	Total number of grid
Mesh B3Fs1	10	34	127	1610
Mesh B3Fs2	10	24	90	1140
Mesh B3Fs3	10	17	64	810

Table 3.9. Convergence study for second order solution					
Parameter	(η_2/A_1)			$(F_x^{(2)}/\rho g r^2 A_1)$	$(F_z^{(2)}/\rho g r^2 A_1)$
	Front	Shoulder	Back		
Mesh B3Fs1	0.1271	0.1307	0.1117	0.0497	0.0483
Mesh B3Fs2	0.1269	0.1306	0.1116	0.0550	0.0486
Mesh B3Fs3	0.1265	0.1304	0.1114	0.0655	0.0491
ε_{21}	0.00019	0.0001	0.00011	0.0053	0.0003
ε_{32}	0.00038	0.000187	0.0002	0.0105	0.00054
R	0.5155	0.5319	0.5263	0.5048	0.5455
p	1.9121	1.8215	1.8520	1.9727	1.7489
GCI₂₁ [%]	0.0266	0.0142	0.0139	0.6752	0.0450
GCI₃₂ [%]	0.0516	0.0267	0.0264	1.3377	0.0825

3.4. Comparisons with experimental data

3.4.1. Wave elevation around the cylinder

Prior to executing our CFD modeling, the comparison between the numerical accuracy and available experimental data is necessary. Hence, in this section, the numerical results obtained from the Navier-Stokes solver are compared with the experimental data which was provided by ITTC (OEC) [2013]. The mean value, 1st and 2nd harmonics are compared for free surface elevations and horizontal/vertical wave forces. The comparison is carried out under wave conditions of (T=7s) and (T=15s) with three wave steepness of (H/L=1/30, 1/16 and 1/10). The first and second harmonics of the wave elevation are normalized by incident wave amplitude (A_1) and for wave forces, they are normalized by ($\rho g A_1$). Fig.3.8&3.9&3.10 shows the comparison of normalized 1st and 2nd harmonics and mean value of wave elevation along the center plane in terms of wave probes location (x/D).

The first harmonic is the amplitude of the wave elevation, (η_1), around the cylinder at the fundamental wave frequency (ω). According to linear diffraction theory, the 1st harmonics of wave elevation are large by value as the diffraction number increases. For long wave cases, the cylinder is transparent to the incident wave. Compared to the experimental results. Therefore, as it is expected, the 1st harmonic value is approximately one at most of wave probes location. For Navier–stokes model, compared to the experimental results, although there is a slight difference in some points, but the numerical solution shows good agreement

in value and trend for small ($H/L=1/30$) and moderate ($H/L=1/16$) steep wave cases and slight difference for high steep wave cases ($H/L=1/10$) by the 1st harmonics, see Fig.3.8. In the case of Potential flow model, the first-order potential solution is reasonably accurate at low and moderate steepness ($H/L=1/30, 1/16$) for both long and short waves. For the cases under high steepness ($H/L=1/10$), diffraction theory overestimates and underestimates the experiments for wave probes located at the front and back part of the cylinder, respectively. This deviation is possibly due to the limitations of linear diffraction theory which can only consider the contribution of the first-order term. However, terms higher than first order may produce contributions to the first harmonic in experiments by nonlinear combinations of components.

The second harmonic of wave elevation around the cylinder is the amplitude of the wave elevation, (η_2) , at double wave frequency (2ω). The nonlinear interaction is more apparent, mainly, for short wave cases at back and shoulder point and for long wave cases at front and back points. Hence, it is a challenge for the numerical model to replicate the experimental measurements at these points correctly. For Navier–stokes model, as it is seen in Fig.3.9, the numerical solution is reasonably accurate for 2nd harmonics by both small ($H/L=1/30$) and moderate ($H/L=1/16$) steep wave cases for both short and long wave cases. However, in the case of high steep waves ($H/L=1/10$), there is small underestimation for short wave case while there is a considerable discrepancy, mainly overestimation, for long wave case. In experiments, it is possible that some high steep waves break before reaching the cylinder which can affect the harmonics of wave elevation around the cylinder and leads to such inconsistency. For the potential-flow model, the second order diffraction solution follows the harmonic pattern of experiments just for short wave cases while underestimates the experiments for all cases. Increasing the wave steepness and wavelength, the deviation from experiments becomes more significant. The potential-flow model can calculate only the first and second order components. Therefore this discrepancy indicates the contribution of harmonic components higher than second order, particularly at high steep waves, in experiments via nonlinear combinations of components.

The mean value is the average of free surface elevation time history, (η_0) , at each wave probe. The magnitude of the mean value in steep waves can become significant, but smaller than the 2nd harmonics at corresponding wave probe. The mean value may be affected by the magnitude of run-up/down, sharp wave crest or flat wave trough and also the presence of

edge waves (by both value and phase). As it is seen in Fig.3.10, the mean value pattern includes two positive peak value at the front and back point and a negative peak value at shoulder point of the cylinder for most of the cases by experiment. Considering experimental data, the Navier–Stokes model, estimates experiment well for small steep waves ($H/L=1/30$) by both short and long wave cases. As the wave steepness increases, the mean value distribution pattern is maintained. In the case of the moderate steep wave, there is a slight difference, particularly at front point. Whilst for high steep waves a notable difference is observed particularly at front and shoulder point of the cylinder. For short waves by moderate steep waves ($H/L=1/16$) the mean value at the front side is over-estimated, while at high steep wave ($H/L=1/10$) it is underestimated. On the back face of the cylinder, the mean value is estimated well at all three wave steepness while the difference increases at both up and downstream due to wave breaking. For long wave case with a moderate steep wave, the numerical solution is reasonably accurate except for a discrepancy at front point. For the other cases with the wave steepness of ($H/L=1/30$ and $1/10$), there is good agreement by trend but considerable deviation by a value which is more apparent in high steep wave case by overestimation. The solution by potential-flow model, just in the case of low wave steepness, for short wave is reasonably accurate at all wave probes. For the other cases by increasing wave steepness and wavelength, the second order diffraction solution underestimates the mean value significantly at the wave probes excluding shoulder and back quarter point where there is an overestimation. The same as 2nd harmonics, this underestimation indicates that the mean value is influenced by higher than second-order terms in the experiments.

The comparison for a numerical solution based on Navier-Stokes solver and the given experimental data for both wave elevation and horizontal/vertical wave forces on the cylinder indicates that there is a reasonable agreement for small and moderate steep waves for both short and long waves. The proper treatment of sharp, steep and high-frequency air/water interface caused by strongly non-linear wave-cylinder interaction. In the present numerical model by interFoam V2.2.2, the free surface is solved by the VOF method in combination with interface compression technique of MULES. Recently Roenby. J et. al.[2016, 2017], presented the new method of IsoAdvector in interFoam and they concluded the considerable improvement in the treatment of sharp interface over MULES technique. IsoAdvector is a geometric VOF method for advection of a sharp interface between two incompressible fluids. According to Devolder et al. [2017] and the simulation of wave propagation for assessment of NWT conducted by the author, excessive wave damping along the tank was observed. This

can affect the incident wave condition characteristics and consequently the nonlinear wave-cylinder interaction. Therefore employing other methods to solve free surfaces such as a combination of VOF and Level Set methods, Dianat.[2017] or the mentioned IsoAdvector interface compression method may improve the solution and can be investigated as future work.

3.4.2. Wave forces on the cylinder

The 1st, 2nd harmonics and mean value of horizontal/vertical wave forces on the cylinder are defined as $(\mathbf{F}_{x,z}^{(1)})$, $(\mathbf{F}_{x,z}^{(2)})$ and $(\mathbf{F}_{x,z}^{(0)})$, respectively. Fig.3.11&3.12 shows the comparisons of 1st, 2nd harmonics and mean value of horizontal/vertical wave forces in terms of wave steepness. The nonlinearity of the wave field surrounding the cylinder can influence the harmonics of wave forces on the cylinder. Hence, the discrepancy of wave elevation, affecting the dynamic pressure distribution around the cylinder may result in a discrepancy for horizontal/vertical wave forces. In the general view, the numerical solution by Navier-Stokes solver underestimates the experiments slightly for horizontal/vertical forces except for the mean value by vertical forces which is overestimated with a small difference. As it is seen in Fig.3.11, increasing the wave steepness, there is a slight reduction in 1st and 2nd harmonics of horizontal force while the mean values are fairly independent of steepness. As the wave steepness increases, the energy dissipation due to local wave breaking around the cylinder is increased which may be the reason for the mentioned reduction. The long waves have lower 1st harmonics of horizontal force, but higher 2nd harmonics compared to short waves which suggest the notable nonlinearity in horizontal force for long wave cases. For vertical force, the 1st and 2nd harmonics are fairly independent of steepness. Potential-flow model, in the case of horizontal force, matches well the experiments by the 1st harmonics and mean value for long wave and 1st harmonics for short wave. However, underestimates the 2nd harmonics and mean value for short wave and 2nd harmonics for long wave cases significantly. For vertical force, there is a good agreement for 1st and 2nd harmonics with slight overestimation for mean value. The aforementioned discrepancies may be due to the higher-order contributions beyond second order and also viscous and turbulent effects.

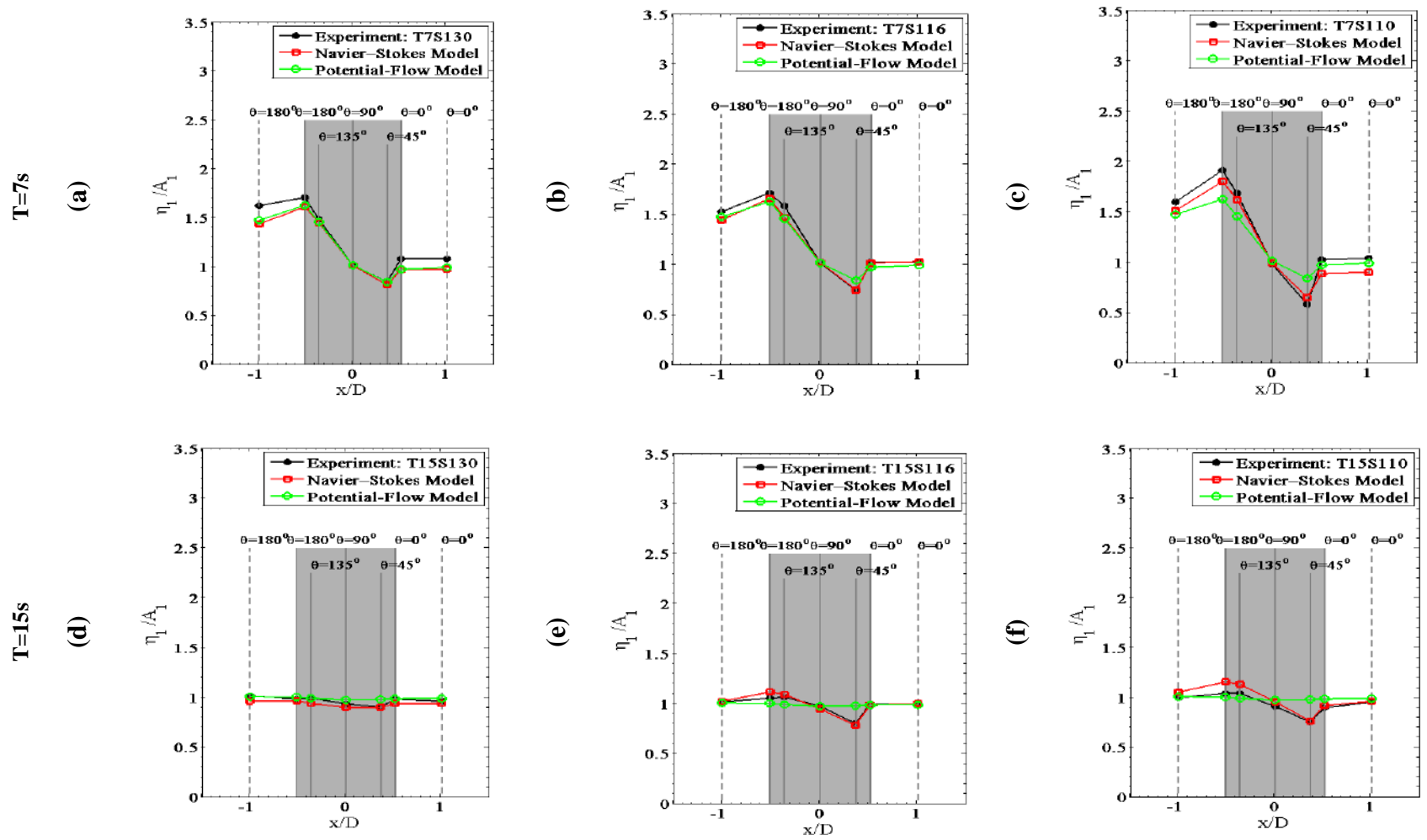


Fig 3.8. Normalized 1st harmonics of wave elevation around the cylinder, (vertical solid line ($r/D=0.513$) and vertical dash line ($r/D=1.0$))

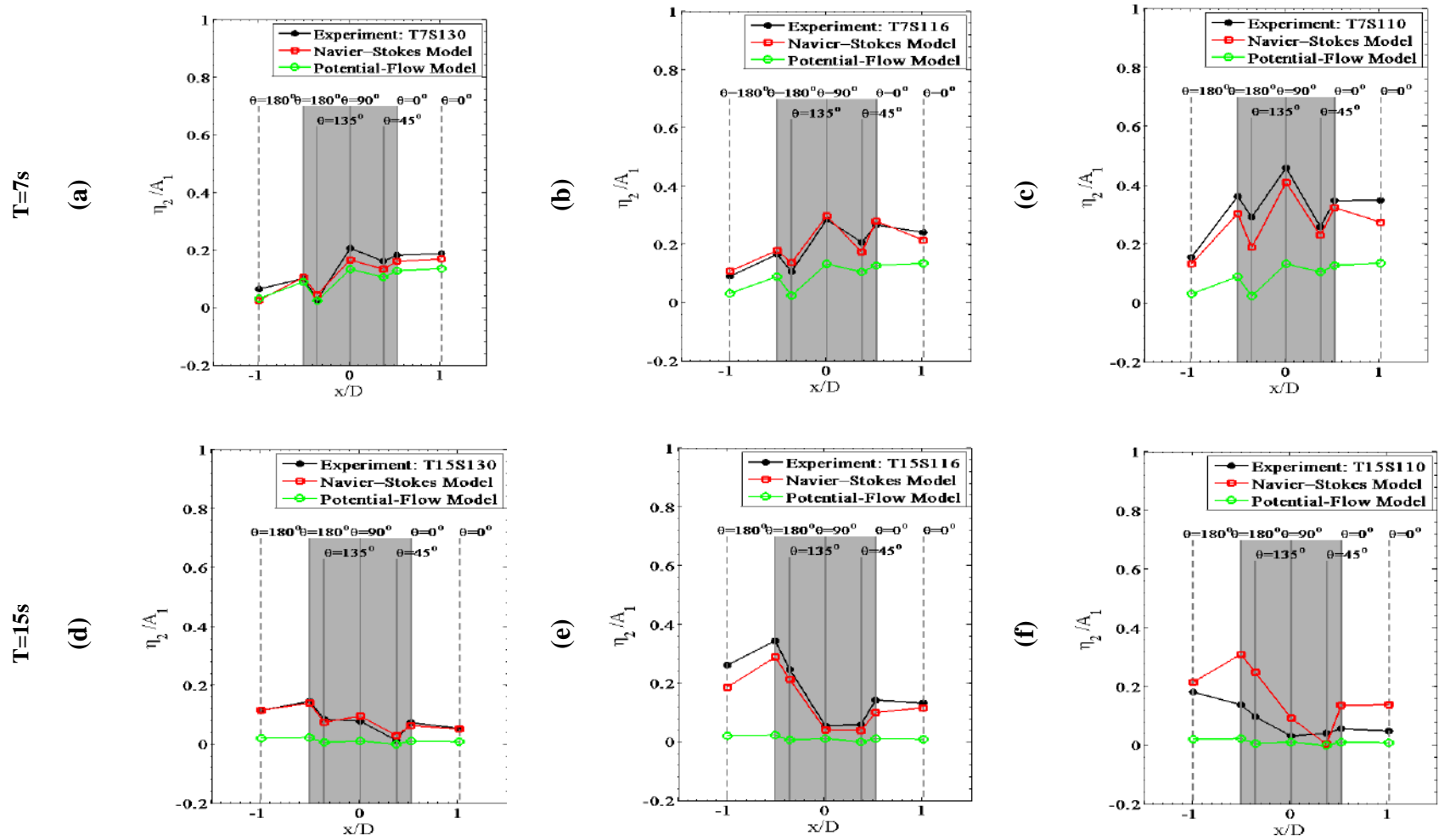


Fig 3.9. Normalized 2nd harmonics of wave elevation around the cylinder, (vertical solid line ($r/D=0.513$) and vertical dash line ($r/D=1.0$))

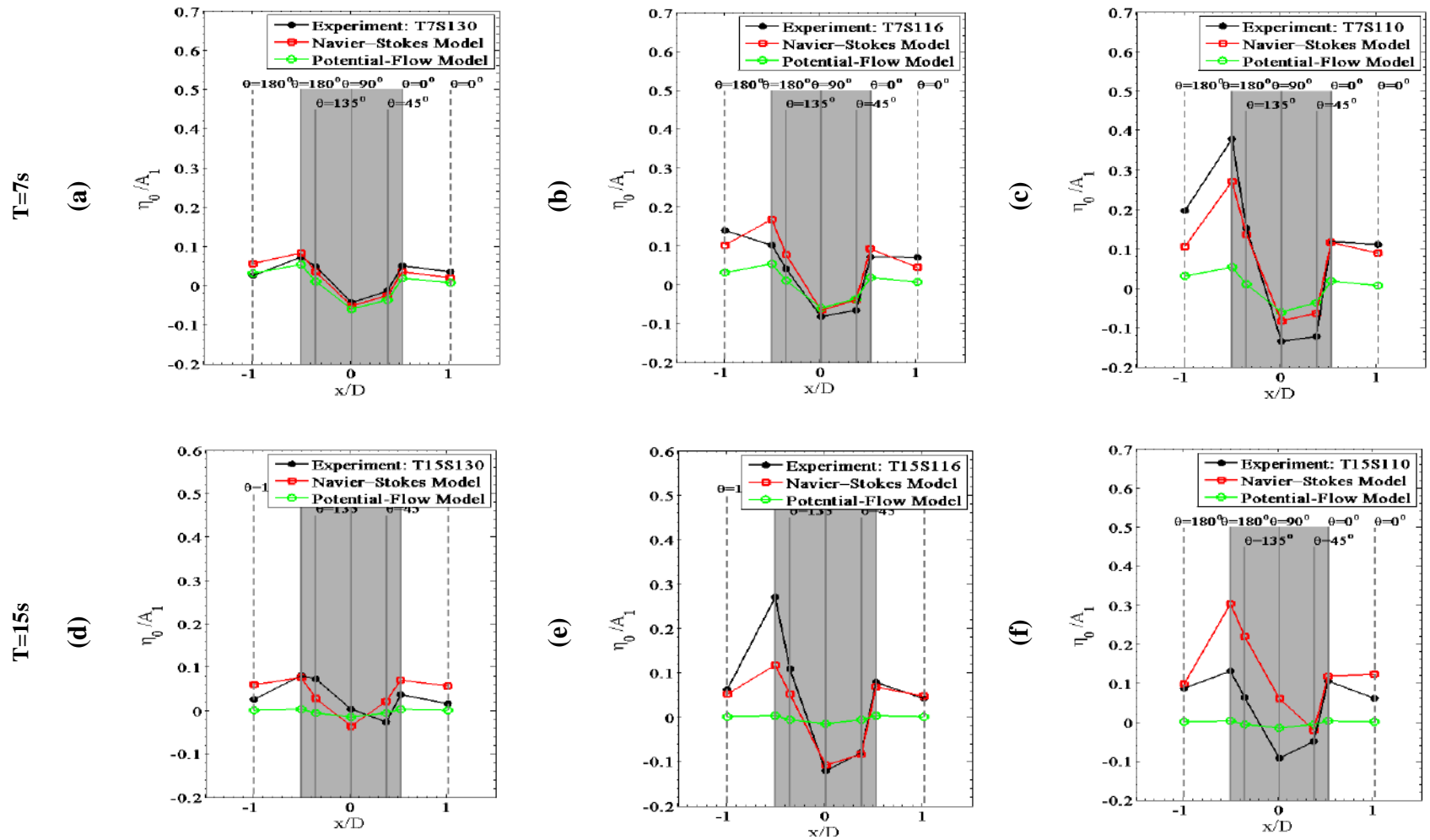


Fig 3.10. Normalized mean value of wave elevation around the cylinder, (vertical solid line ($r/D=0.513$) and vertical dash line ($r/D=1.0$))

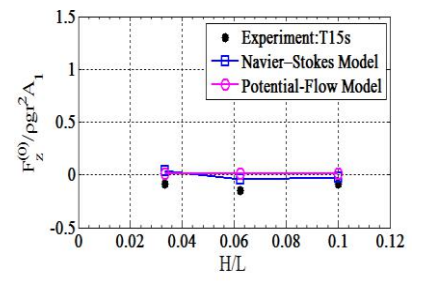
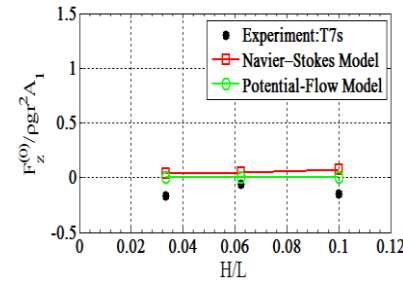
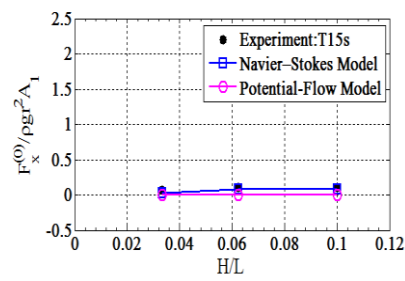
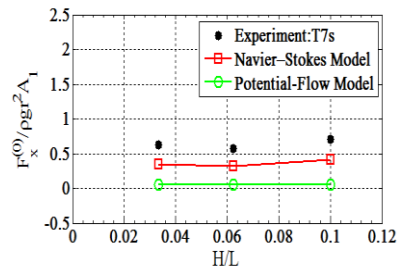
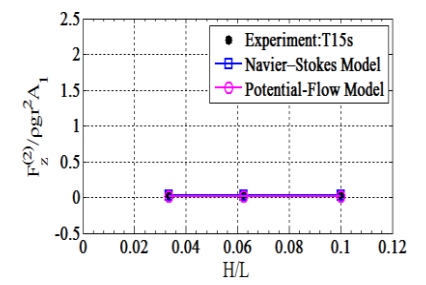
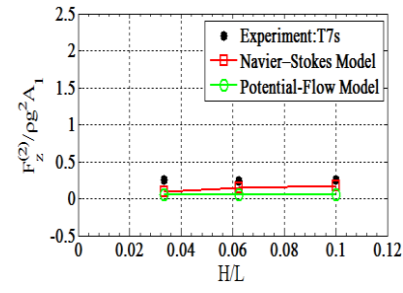
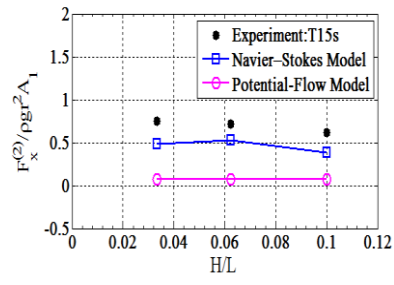
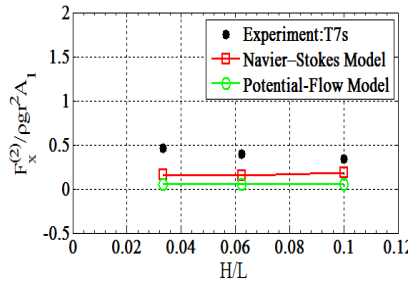
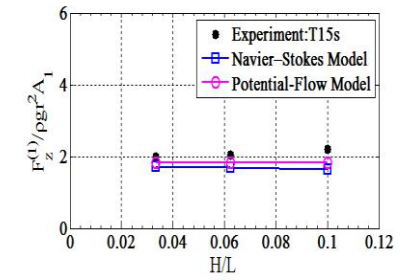
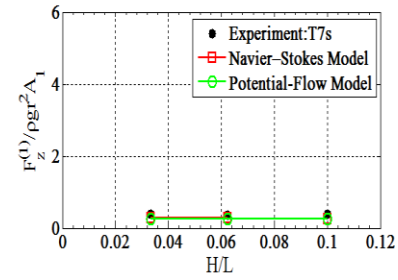
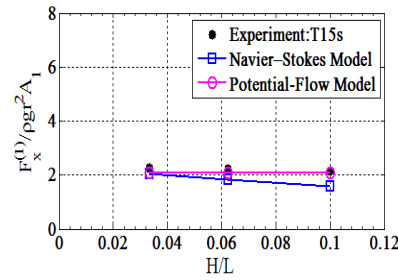
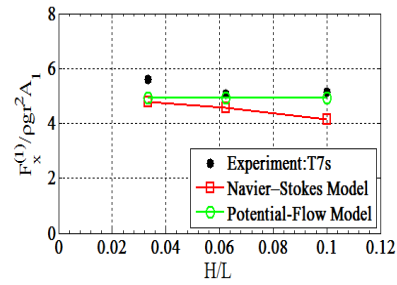


Fig 3.11. 1st and 2nd harmonics and mean value of horizontal force, under variation of wave steepness for both short and long waves

Fig 3.12. 1st and 2nd harmonics and mean value of vertical force, under variation of wave steepness for both short and long waves

Chapter 4

Wave run-up on a vertical surface-piercing cylinder

In this chapter, mainly, the role of wave scattering Type1&2 on the nonlinearity of wave field amplification around the cylinder is analyzed. With regard to the literature review, wave steepness and wave diffraction play an important role in the wave scattering and wave run-up around the cylinder. Therefore, in the following, primarily, the physical mechanism of wave scattering around the cylinder is illustrated in section 4.1. Then the effect of a change in both wavelength and wave steepness on the wave field around the cylinder and inline wave force are studied in section 4.2 and section 4.3 and section 4.4, respectively. Section 4.5, illustrates the influence of potential flow, viscous and turbulence effects on wave scattering around the cylinder. Section 4.6, presents the analyzed change in the submerged geometry and finally, the effect of cylinder cross-section on the wave field around the cylinder is investigated in section 4.7.

4.1- The physical mechanism of wave scattering

The study of the physical mechanism of wave scattering around a single cylinder involves step by step wave-cylinder interaction over a complete incident wave cycle. Consequently, four key incident wave phase angles are considered at the front stagnation point of the cylinder. With regard to the incident wave propagation from left to right, these wave phases corresponding to $(\phi = 0)$, the arrival of a wave crest, $(\phi = \pi/2)$, the arrival of a wave zero down-crossing, $(\phi = \pi)$, the arrival of a wave trough and $(\phi = 3\pi/2)$, the arrival of a wave zero up-crossing. For this study, the short wave of $(T=7s)$ and $(H/L=1/16)$ is considered as reference wave condition. The instantaneous free surface elevation and related velocity

magnitude of the aforementioned wave phases for the reference wave condition is shown in Fig.4.1.

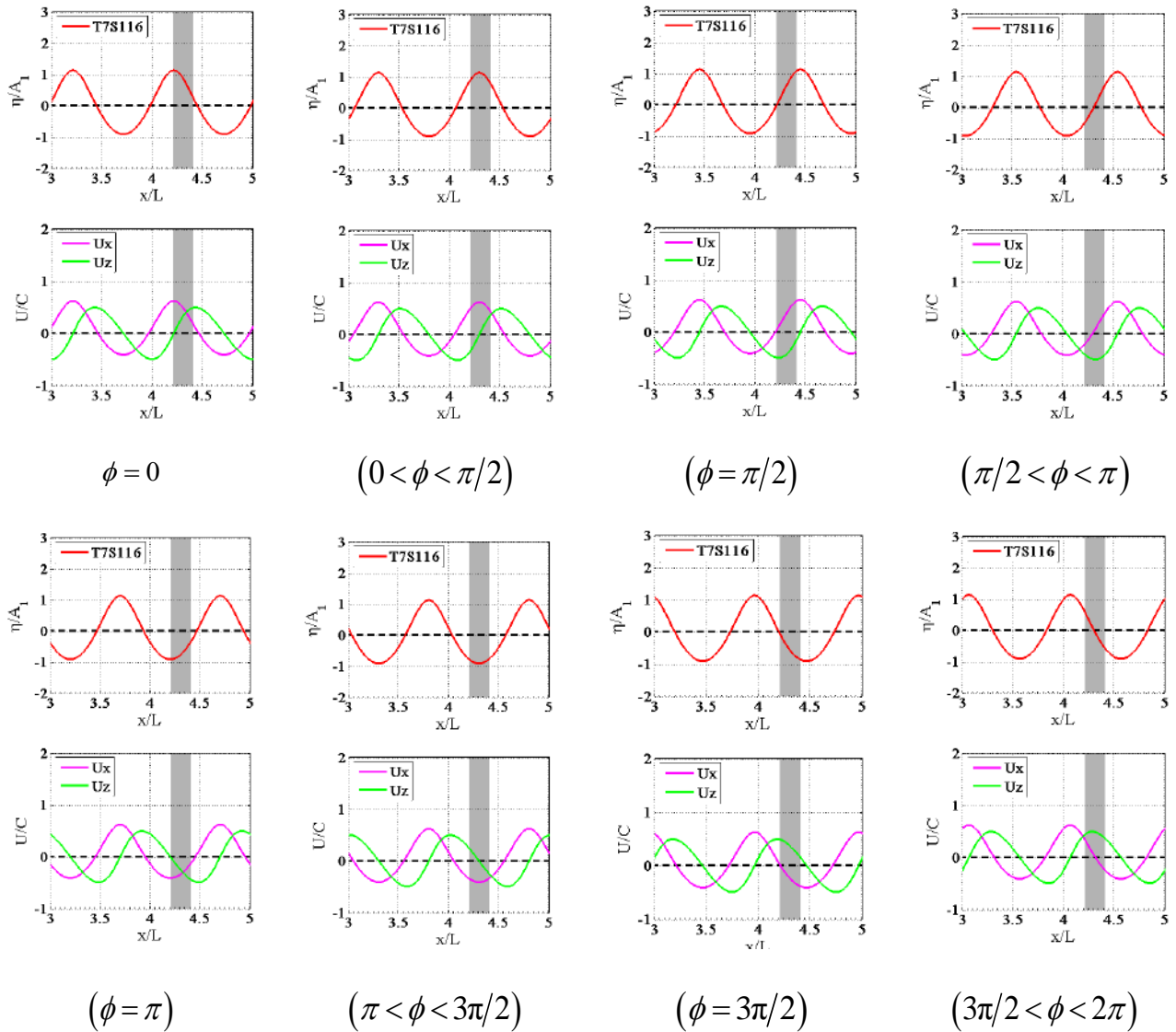


Fig 4.1. Wave elevation profile and corresponding velocity components at four given wave phases interacting with cylinder front point

The observation based on physical experiments reported by **Swan et al. [2005]**, reveals that there are two distinct and notable high-frequency scattered wave fields around the cylinder which are identified as **Type1** and **Type2** waves. The first scattered wavefield which is referred to as **Type1** is associated with the run-up and wash-back process on the surface of the cylinder. This process creates a disturbance on the free surface which is reflected radially outwards. The height of this disturbance is damped radially through wave dispersion and dissipation and leads to concentric and symmetric wave field. In each regular incident wave

cycle, there is two wave scattering of Type1, one scattered from front stagnation point in an upstream direction and one from back stagnation point in a downstream direction which are caused by the interaction of incident wave crest and trough, respectively.

The incident wave passes the front stagnation point and wrapping around the cylinder is divided into two distinct semi-circular wavefronts at both sides which are known as lateral edge waves. These waves move in both parallel and opposite direction of the incident wave. Formation of edge waves has been discussed in a series of papers by Chaplin et al. [1997]; Chaplin et al. [1999], Chaplin [2001], Rainey [1997] and Retzler et al. [2000]. These researchers mainly observed edge waves during vertical oscillation of a cylinder in still water or in the case of passage of steep waves by fixed vertical and surface piercing cylinders. The edge waves traveling around the cylinder circumference in the downstream direction, reach the back stagnation point. They collide and then merge completely along the centerline of the cylinder parallel to the incident wave to form a notable mound of water and leading to non-concentric and symmetric wave pattern. This violent and highly non-linear free-surface motion is defined as wave scattering **Type2**. If the incident wave period is sufficiently long, these two edge waves can circulate around the cylinder and travel in an upstream direction against the incident flow direction. Afterward, they collide and merge for the second time along the centerline of the cylinder at front stagnation point to form another wave scattering Type2. The edge waves are appeared to be trapped on the free surface cylinder interface where may be related (in part) to the Coanda effect, Swan et al. [2015].

In order to investigate the changes in the free surface elevation during the wave-cylinder interaction, the spatial contour of the free surface evolution around the cylinder, for the given wave phases by the top and side views are analyzed, see Fig.4.2&4.3. In all of these figures, the wave advances in a positive direction from the left to right. The interaction of long-crested incident wave velocity components, (u, w) , mainly horizontal component, with front stagnation point during the passage of wave trough, $(\phi = \pi)$ from the previous wave cycle until the arrival of wave zero-down crossing, $(\phi = \pi/2)$, raise the water level in the form of a thin vertical jet along the cylinder. This leads to wave run-up in the form of wave scattering Type1, see Fig.4.2 & Fig.4.3(e). In the context of non-breaking incident waves, there is no wave impact but very large run-up velocities due to the interaction of wave scattering Type1 with the cylinder, Swan et al. [2015]. After the water level reaches its maximum height with

the arrival of the wave crest, where it is known as green water level for non-breaking incident waves, Ramirez. [2013], it runs down and washes back, mainly at the upstream direction, see Fig.4.2(d)&4.3(e).

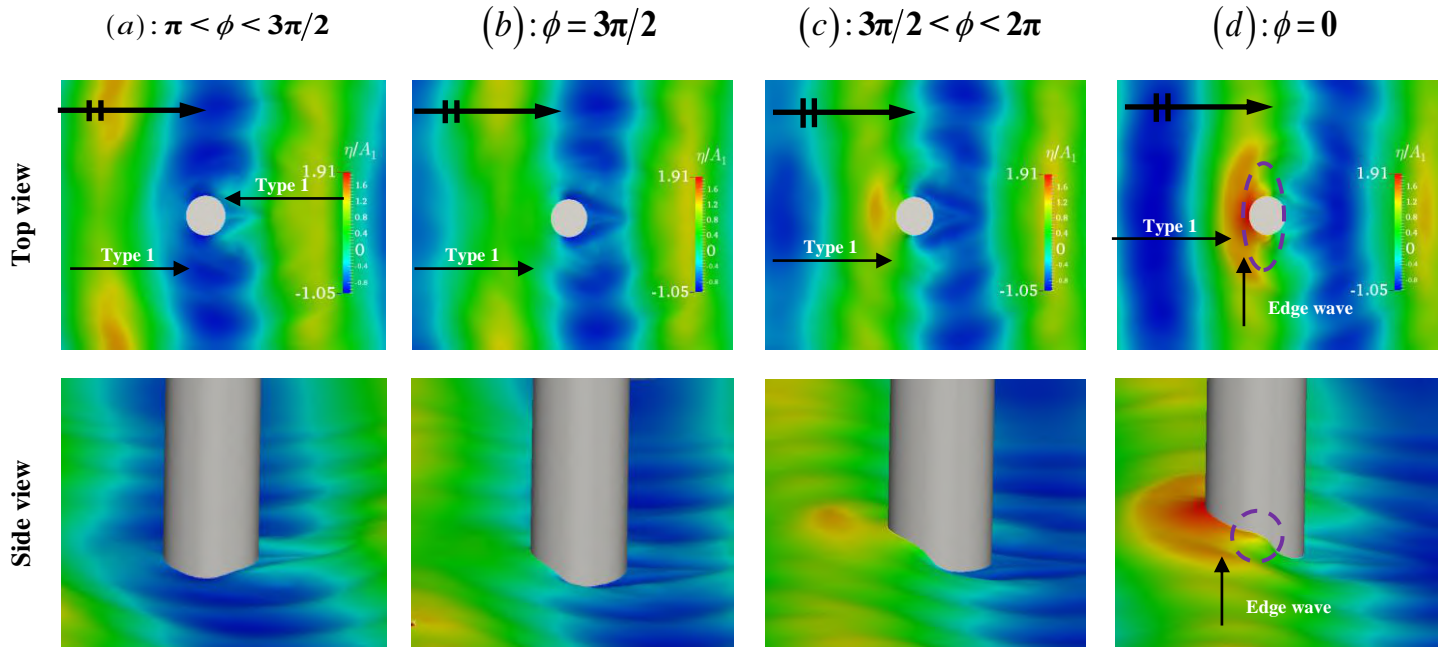


Fig 4.2. Spatial contours of the free surface elevation around the cylinder, wave condition $T=7s$, $H/L=1/16$

As the incident wave wraps around both sides of the cylinder, $(0 \leq \phi \leq \pi/2)$, see Fig.4.3(e), the resultant lateral edge waves are headed in the downstream direction. Reaching the back stagnation point, $(\phi = \pi/2)$, see Fig.4.3(f), they collide and merge to form a notable mound of water that reaches its maximum height following the arrival of the wave crest, see Fig.4.3(g), and build the second reduced run-up comparing to the front face. Since this scattering occurs in the vicinity of the wave crest, the corresponding wave field is steepened and subjected to horizontal incident wave velocity. The resultant disturbance by wave scattering Type2 involves unsteady, wave breaking/bubbly wake flow. During the passage of wave crest and the arrival of zero down crossing, $(\pi/2 \leq \phi \leq \pi)$, at the back face, some part of the disturbance (the tail) are swept away in a spiral fashion and eventually get damped at some distance from the cylinder, see Fig.4.3(g&h). The rest of disturbances close the cylinder begin to pass through one another to form another pair of semi-circular lateral edge waves which initiates wave scattering Type2 in the upstream direction. As a future interesting study, the effect of disturbances in Fig.4.3(h), which propagating a way in downstream direction can be investigated in the case of a two-cylinder arrangement in tandem. This disturbance may

steepen the incident wave interacting with the back cylinder located in the shadow region of the front cylinder and can affect the corresponding wave amplification, based on the leg spacing.

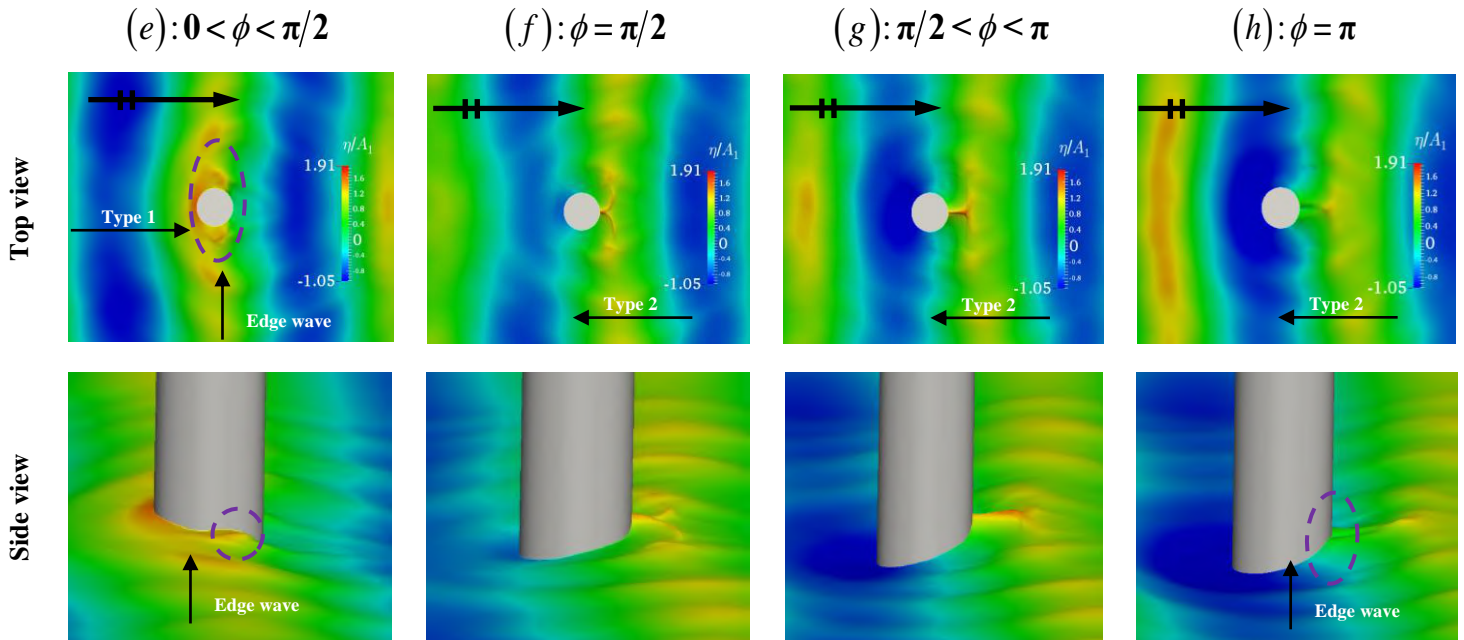


Fig 4.3. Continued, spatial contours of the free surface elevation around the cylinder, wave condition $T= 7s$, $H/L=1/16$

With the arrival of the incident wave trough at the front face of the cylinder, ($\phi = \pi$), there are favorable wave-induced fluid velocities by the trough in opposite direction of the incoming wave. Hence, these lateral edge waves begin to propagate around cylinder from back to front face. As the incident waves advance, these edge waves are steepened subjecting to the negative fluid velocity with respect to the direction of wave propagation, see Fig.4.3(h). Afterward, as the wave trough reaches the back face of the cylinder, the negative horizontal fluid velocity leads to the second wave scattering of Type1 which is scattered in the downstream direction, see Fig.4.2(a&b). In the present analysis for the reference case, as it is seen in Fig.4.2(a), the lateral edge waves can eventually reach the shoulder point of the cylinder. Therefore there is no formation of wave scattering of Type 2 at the front stagnation point. After that following the passage of wave zero up-crossing, ($\phi = 3\pi/2$), at the front point, the lateral edge waves are driven back around the cylinder in the downstream direction, see Fig.4.2(b). In regular waves, the formation of the mentioned wave scattering and run-up around the cylinder becomes repetitive, Swan et al. [2015].

4.2- Effect of wavelength on wave Run-Up

In this section, the influence of a change in wavelength under moderate steep wave condition on wave scattering and related wave amplification around the cylinder is investigated. The extension that the lateral edge waves can travel around the cylinder in upstream direction is associated to (a): the local flow energy at back of the cylinder, (b): the amount of edge wave energy reduction during interaction with cylinder circumference and incident wave, (c): the incident wavelength or period and the cylinder circumference which defines the propagation time before arrival of zero-up crossing at front stagnation point.

Increasing the incident wavelength from short ($T=7s$) to long wave ($T=15s$), primarily, the formation of wave scattering Type 2 in front of the cylinder is observed. As it is seen in the spatial contour of wave elevation, see Fig.4.4 (b&c), there is a partially and fully developed wave scattering Type2 pattern for cases of ($T=9s$) and ($T=15s$), respectively. Afterward, the lateral edge waves which have already reached the front of the cylinder, pass through each other during the passage of incident wave phase between the trough and zero-up crossing at the front stagnation point. Then, they are driven around the cylinder in a downstream direction with the arrival of wave zero-up crossing. The rest of disturbances by wave scattering Type2 is scattered in the upstream direction and merged along the centerline of the cylinder and subjected to positive velocity components by the next wave cycle. Thus, there is a wave-wave interaction (scattered, incident) which is known as the classical local short-long wave interaction, Longuet-Higgins [1960]. This can enhance the wave kinematics and steepen the next incoming wave and contribute considerably in the wave scattering Type1 and eventually increase the run-up height at the front point of the cylinder for long wave cases, see Fig.4.4 (c).

The energy reduction for the scattered waves in the upstream direction is less than the waves scattering in the downstream direction. The arrival of wave crest and formation of wave scattering Type1 at cylinder front point is shown in Fig.4.5. As it is seen, the edge waves have reached the shoulder point for short wave case ($T=7s$) and about back corner point for the intermediate wave case ($T=9s$), see Fig.4.5(b). For long wave case ($T=15s$), the edge waves have already reached the back point, contributing in a mound of water and partially formation of wave scattering Type2 at the back of the cylinder, see Fig.4.5(c).

During the arrival of wave crest at back point of the cylinder, a fully developed wave scattering Type2 is observed for all cases, see Fig.4.6. For short wave case ($T=7s$) the

collision of edge waves and interaction with cylinder leads in higher and steeper run-up at back point due to large diffraction, see Fig.4.6(a). However, reduction in diffraction for longer wave cases ($T=9s$ and $T=15s$) causes the wave run-up height and steepness reduction, as well. Taking into account the contribution of edge waves from previous wave cycle and vortex formation, there is strong local flow at the back of cylinder which is more apparent for long wave case ($T=15s$), see Fig.4.6(c). Changing the wavelength from short to long, the energy of local flow at back and the time for traveling of edge waves in upstream direction are increased while the edge wave energy reduction is reduced due to less wave-cylinder interaction. This can cause the occurrence of the mentioned fully developed wave scattering Type 2 at front of the cylinder.

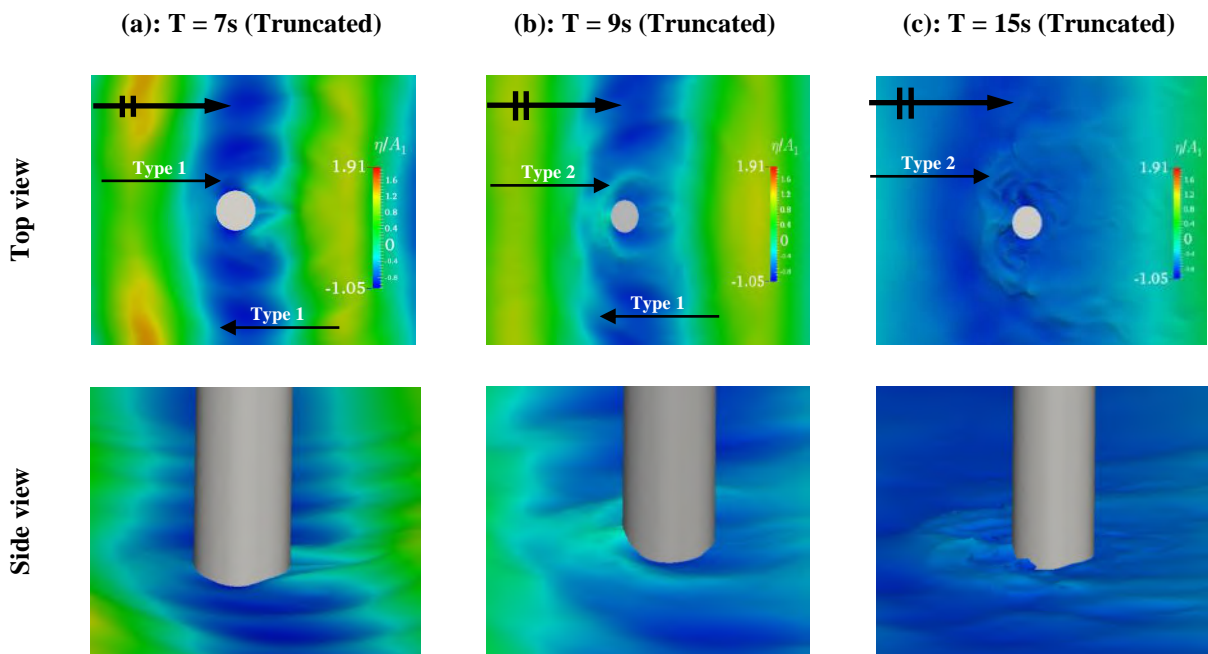


Fig 4.4. Spatial contours of the free surface elevation around cylinder under variation of the wavelength for moderate steep waves, before the arrival of wave zero up crossing at back point

According to the literature review, wave run-up is known as an high-order nonlinear wave transformation. Hence, harmonic analysis can provide important information on non-linear contribution to wave scattering and amplification around the cylinder. Fig.4.7, illustrates the comparison of normalized mean value and harmonics of surface elevations in terms of wave probes location (x/D), for different wavelengths. The time histories of wave elevation at given wave probes (on-body) are presented in Fig.4.8 which can provide necessary information to analysis the corresponding harmonics. For short wave case, the notable diffraction causes large wave run-up height. The arrival of the wave crest and corresponding

wave scattering Type2 results in peak value at front face. Consequently, the value of 1st harmonics at the front stagnation point is about 1.7 where according to linear diffraction theory, increasing wave diffraction, it can asymptotically reach factor 2, see Fig.4.7(b). As it is seen there is a reduction in 1st harmonics from the front to the back corner points. Therefore there is a minimum value at depression point located at the back-corner point. This can be related to the energy reduction of the aforementioned lateral edge waves caused by the run-up/wash-down process alongside with energy dissipation due to local wave breaking around cylinder circumference. Afterward, the collision of lateral edge waves at cylinder back stagnation point raises the water level and results in the second run-up which is characterized by high frequency and steep waves.

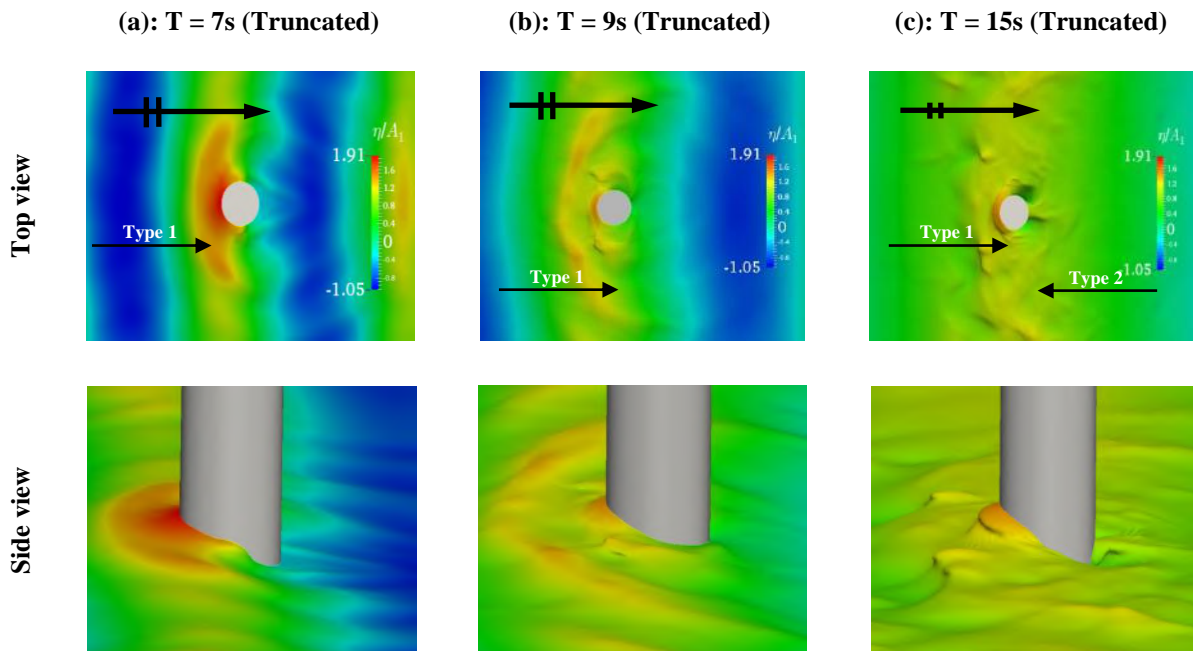


Fig 4.5. Spatial contours of the free surface elevation around cylinder under variation of the wavelength for moderate steep waves, the arrival of a wave crest at the front point

In long wave case as the change in incoming wave velocity is smooth, interaction with cylinder causes a small disturbance at the surrounding wave field. Therefore, based on the linear diffraction theory the 1st harmonic value of one due to small diffraction is expected. However, as it is seen the 1st harmonic pattern is the same as short wave case and the value at front and back points are about 1.2 and 1, respectively, see Fig.4.7(b). The 1st harmonic at the front point is related to the aforementioned short-long wave interaction. Systematic increasing of wavelength from short to intermediate and long waves, the 1st harmonic pattern remains constant and the amplification factor at front point reduces from,1.7 to1.3 and finally

1.2 where all of them are important in the viewpoint of air gap design, see Fig.4.7(b). For long wave although the increment value is small but taking into account the wave steepness of ($H/L=1/16$), see Table 3.1, the wave height is already large, therefore even this small increment can cause notable run-up at front point of the cylinder. In the case of 1st harmonics by back point, the edge waves from previous incident wave cycle are driven in downstream with the arrival of zero up crossing. Then, these lateral edge waves with the arrival of the crest in combination with attached vortexes at the back of the cylinder, raise the water level and although the diffraction is small eventually it results in a 1st harmonic value close to short wave case, see Fig.4.7(b).

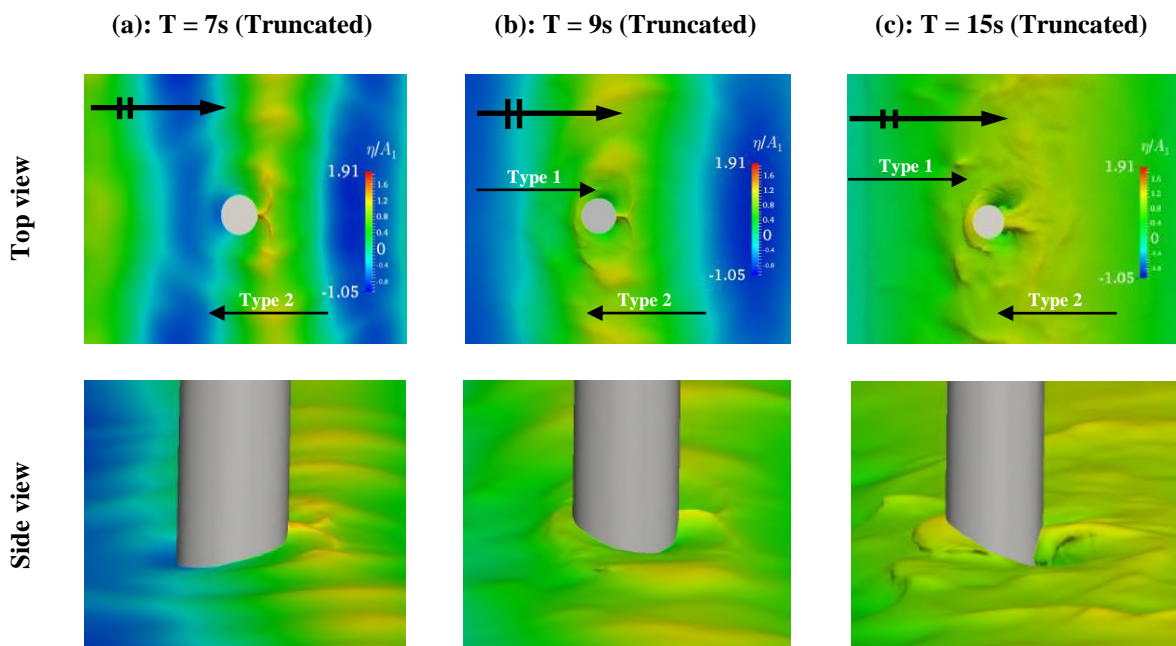


Fig 4.6. Spatial contours of the free surface elevation around cylinder under variation of wavelength for moderate steep waves ($H/L=1/16$), the arrival of wave crest at the back point

The 2nd harmonic pattern for short wave case, see Fig.4.7(c), shows three peak values at front, shoulder and back point of the cylinder. The peak at the front is related to wave scattering Type1 which is smaller than the other two peak values. Then as the diffraction is important in this case, the collision of lateral edge waves with the cylinder in the form of wave scattering Type2 results in steep run-up which is observed as a peak value at the back point, see Fig.4.8(a5). After that, the lateral edge waves are driven in the upstream direction and as the wave period is small, reaching the shoulder point, they interact with the wave trough, see Fig.4.8(a3). Thus, the peak value at the shoulder which is higher than the other two mentioned peaks is caused by strong edge wave interaction with a maximum value of the negative horizontal velocity of wave trough. As it is seen in Fig.4.7(c), the two depression

points at front corner and back corner are associated with the interaction of edge waves with velocity components of wave-induced flow by the phase close to passage of zero-down crossing and arrival of the trough at back corner and front corner, respectively, see Fig.4.8(a2&a4). The energy of edge waves reaching the front corner is less than back corner due to more interaction with the cylinder, therefore the 2nd harmonics at back corner is larger.

The 2nd harmonics for long wave case at Fig.4.7(c), indicate that the value at backward half of the cylinder is considerably smaller than the corresponding values for short wave case. There is a weak collision of lateral edge waves at the back stagnation point of the cylinder which leads to small steep waves. This is related to small diffraction in combination with energy dissipation due to the pair of attached vortices. Following the passage of the wave crest at the back of the cylinder, the lateral edge waves are driven in the upstream direction and finally reach the front of the cylinder. The lateral edge waves traveling in the upstream direction, they interact with the incident wave velocity components by the wave phase close to or at the arrival of zero-down crossing in the back corner and shoulder point of the cylinder, respectively. Therefore there is smaller interaction in comparison to short wave case. After that, as the edge waves pass the front corner point, there is considerable interaction with incident wave velocity components at phase close to the arrival of wave trough see Fig.4.8(c2). Eventually, the collision of the lateral edge waves in the form of wave scattering Type 2 and occurrence of the second run-up at front stagnation point leads to a peak value of 2nd harmonics of long wave case.

For the intermediate wave case the diffraction is still important, therefore the harmonic pattern by the front corner to the back stagnation point is similar to short wave case, see Fig.4.7(c). Increasing wave length from short to intermediate wave, a systematic decrease at back and back corner points is observed which is related to change in diffraction. As mentioned before, there is a partially developed wave scattering Type2 at front of the cylinder for the intermediate wave case, see Fig.4.8(b1). Taking into account the importance of diffraction, in this case, the second reduced run up at front point leads to a peak value which is higher than the 2nd harmonics at the rest of the wave probes. The lateral edge waves from previous incoming wave cycle may contribute to wave scattering Type2 at the back of cylinder and formation of local flow which is stronger than short wave case. Although the diffraction is smaller for the intermediate wave case, the interaction of lateral edge waves

traveling in an upstream direction with incident wave velocity components still leads in large 2nd harmonics at the shoulder and front corner points, see Fig.4.8(b2&b3).

Increasing the wavelength from short to long wave, the mean value distribution is similar and the change in magnitude is very small. As it is seen in Fig.4.7(a), there is two positive peaks at front and back and two negative peaks at the shoulder and back corner points of the cylinder. The two positive peak values are related to the occurrence of wave scattering Type1 at front and occurrence of wave scattering Type2 at the back stagnation point. On the other hand, the negative peak values are caused by the interaction of lateral edge waves traveling in an upstream direction with incident waves. With regards to the harmonics higher than 1st, see Fig.4.7(c- e), it is noticed that changing the incident wavelength, the wave field around the cylinder is nonlinear up to 4th harmonics. The nonlinearity for short wave case is more apparent for backward half of the cylinder, especially at the back stagnation point. Increasing the incident wavelength, the nonlinearity is notable at forward half of the cylinder, particularly at the front stagnation point. Comparing the harmonics of the given incident wave conditions, the edge waves and the related wave scattering Type2 contribute more than wave scattering Type1 to the nonlinearity of wave amplification around the cylinder. The wave scattering Type1 contributes more to 1st harmonics rather than higher harmonics.

Furthermore, Fig.4.7 shows the results for truncated (draft(1.5D)) and bottom-mounted cylinders in deepwater under short and long waves condition. Comparing the results, the trend and value are identical for both cylinders for each mentioned case. This suggests that the physics of wave-structure interaction for the given truncated cylinder is the same as a bottom-mounted cylinder. Accordingly, increasing the draft more than (1.5D), the reflection by the underwater volume and also the vortices developing from the bottom of the truncated cylinder for both wave conditions, cannot affect the wave field and wave amplification around the cylinder.

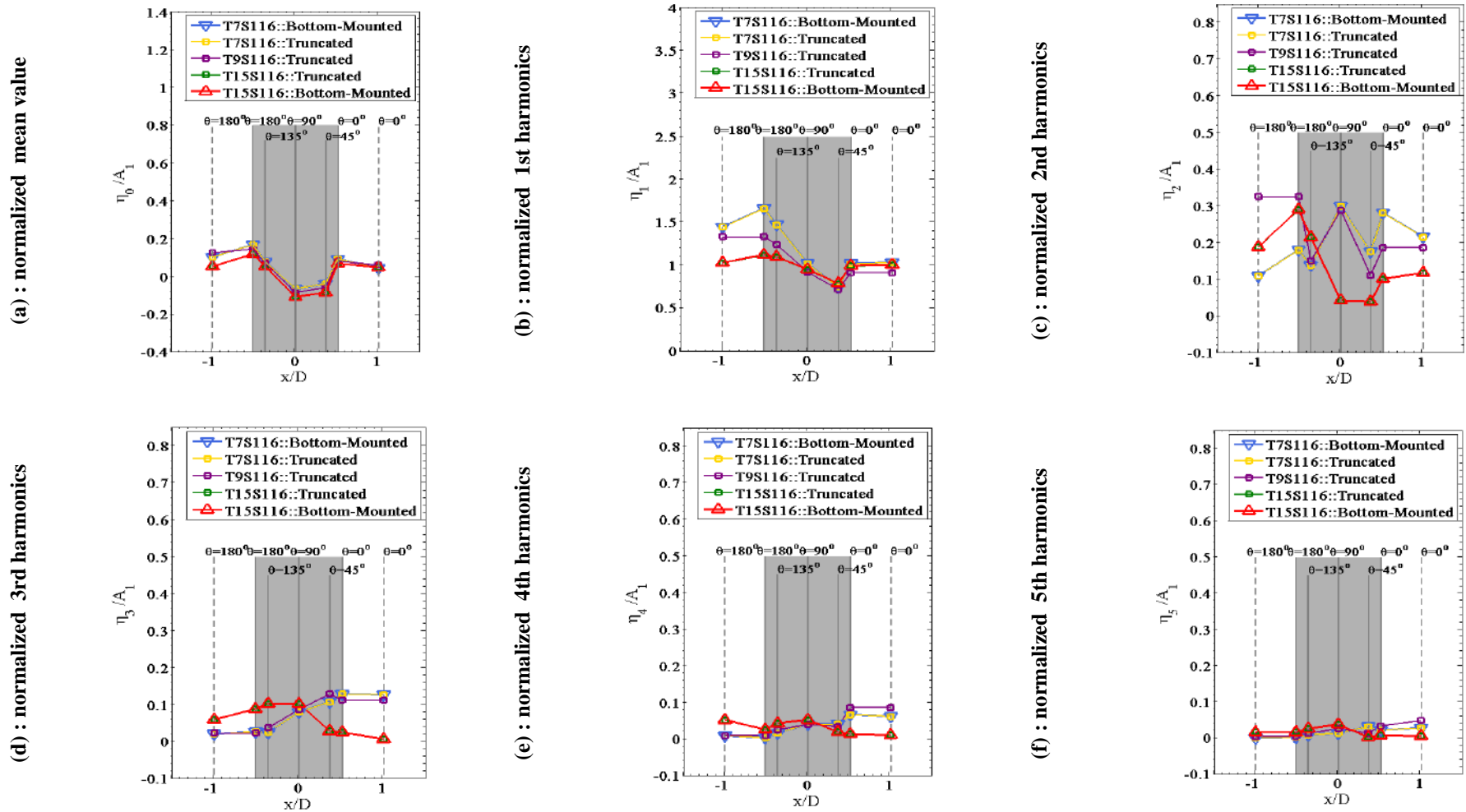


Fig 4.7. Comparison of normalized mean value and harmonics of wave run-up under variation of wavelength for moderate steep waves ($H/L=1/16$) (vertical solid line ($r/D=0.513$) and vertical dash line ($r/D=1.0$))

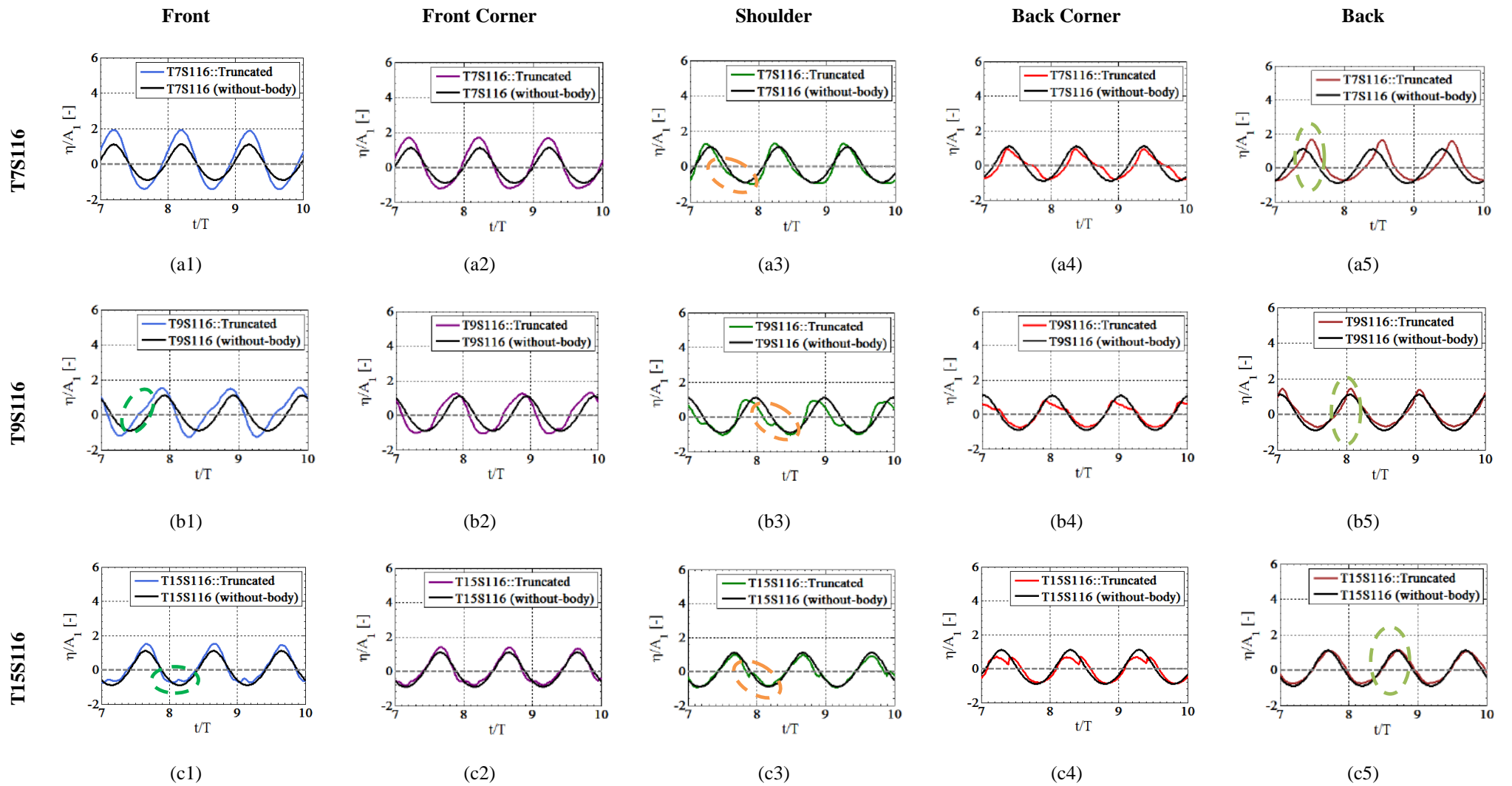


Fig 4.8. Normalized time history of wave elevations at given wave probes location around cylinder under variation of wavelength for moderate steep waves ($H/L=1/16$).

4.3- Effect of wave steepness on wave Run-Up

In the present analysis, keeping the wave diffraction identical in short and long waves separately, the influence of a change in wave steepness is studied. Fig. (4.9-4.12), show the spatial contour of wave evolution at the aforementioned four-wave phases interacting front point of the cylinder during one wave cycle for wave periods of ($T=7s$ and $15s$) with three wave steepness of ($H/L= 1/30, 1/16$ and $1/10$) by top and side view. As mentioned before, the scattering wave pattern due to the interaction of moderate steep wave with a cylinder for the reference case includes two wave scattering Type1 at the front and back point and one wave scattering Type2 at back point of the cylinder. Decreasing the incident wave steepness for short waves from moderate to a small steep wave of ($T=7s, H/L=1/30$), reduces the wave kinematics, see Fig.4.9(a&d) and Fig.4.10(a&d). Although the diffraction in short waves is notable, the wave steepness reduction decreases the wave kinematic and accordingly the energy and propagation speed of lateral edge waves moving around the cylinder. This results in a weak wave-wave and wave-cylinder interaction and consequently maintaining the wave scattering pattern, the wave field around cylinder undergoes weak disturbances. Comparison of the spatial contour of small and moderate incident wave-cylinder interaction, reveals that the lateral edge waves traveling in an upstream direction, weakly interact with opposite propagating incident wave. Accordingly, they can reach about back corner point while for moderate wave case they can reach the shoulder point before the arrival of zero up crossing at cylinder front point.

Increasing the incident wave steepness from moderate to high steep wave of ($T=7s, H/L=1/10$), enhances the wave kinematics and the energy and propagation speed of edge waves moving around the cylinder, as well. This augmentation, maintaining the wave scattering pattern, causes strong wave-wave and wave-cylinder interaction and consequently results in higher and steeper run-up. In addition, the wave field around cylinder undergoes strong disturbances alongside with notable local wave breaking which is known for regular high steep waves($H/L=1/10$), Fig.4.9(c&f) and Fig.4.10(c&f). In section.4.2, it was shown that there is a partially wave scattering Type 2 at front point of the cylinder for the wave condition of ($T=9s, H/L=1/16$). In the case of wave condition ($T=7s, H/L=1/10$), the highly nonlinear wave-cylinder interaction results in strong local flow at cylinder back, see Fig.4.9(f). The (KC) number for the wave conditions of ($T=9s, H/L=1/16$) and ($T=7s, H/L=1/10$) are close by value, Table 3.1. Thus, it is expected that the lateral edge waves in case of ($T=7s, H/L=1/10$) can reach the front point of the cylinder while as it is seen in

Fig.4.10(f), they can eventually reach about the front corner point. Afterward, a notable wave steepness on the wave field and wave amplification around the cylinder, primarily, is similar to short wave cases. Increasing the incident wave steepness from small to high steep wave enhances the wave kinematics and maintaining the wave scattering Type 1 and 2 pattern, results in higher and steeper run up, see Fig (4.11&4.12). In addition since the propagation time for lateral edge wave is sufficient, therefore, there is a fully developed wave scattering Type2 at front of cylinder even for the small steep wave of ($T=15s$, $H/L=1/30$) where undergoes weak wave-cylinder interaction, see Fig.4.11(a). Taking into account the wave evolution by both cases of ($T=7s$, $H/L=1/10$) and ($T=15s$, $H/L=1/30$), suggest that regardless of energy of local flow at cylinder back and amount of lateral edge wave energy reduction traveling upstream, the edge wave propagation time which is related to wave diffraction number play more important role, in occurrence of wave scattering Type2 at front of the cylinder.

In the case of long wave cases where diffraction is small, the effect of a change in wave steepness on the wave field and wave amplification around the cylinder, primarily, is similar to short wave cases. Increasing the incident wave steepness from small to high steep wave enhances the wave kinematics and maintaining the wave scattering Type 1 and 2 pattern, results in higher and steeper run up, see Fig (4.11&4.12). In addition since the propagation time for lateral edge wave is sufficient, therefore, there is a fully developed wave scattering Type2 at front of cylinder even for the small steep wave of ($T=15s$, $H/L=1/30$) where undergoes weak wave-cylinder interaction, see Fig.4.11(a). Taking into account the wave evolution by both cases of ($T=7s$, $H/L=1/10$) and ($T=15s$, $H/L=1/30$), suggest that regardless of energy of local flow at cylinder back and amount of lateral edge wave energy reduction traveling upstream, the edge wave propagation time which is related to wave diffraction number play more important role, in occurrence of wave scattering Type2 at front of the cylinder.

Fig.4.13, illustrates the comparison of normalized mean value and harmonics of surface elevations in terms of wave probes location (x/D) for wave periods ($T=7s$, $15s$) and different wave steepness, separately. For both short and long wave cases, the mean value distribution and the harmonic pattern are almost the same for all three wave steepness. In the case of 1st harmonics for short wave, increasing the wave steepness results in higher run-up at front point. As mentioned before there is a reduction from the front to the back corner point which is notable for high steep waves of ($T=7s$, $H/L=10$) and it is more related to notable local wave breaking caused by strong wave-structure interaction. However, this reduction for long waves is less due to small diffraction. Increasing wave steepness generally enhances the 2nd harmonic. In the case of high steep incident waves, the nonlinear interaction of edge waves at the back of the cylinder results in steep wave scattering strong local flow. Afterward, the strong interaction of the edge waves traveling in upstream with opposing high steep incident waves leads in higher 2nd harmonics at the wave probes from the back corner to front corner for both of short and long waves. For mean value also this strong interaction causes large negative mean values at the shoulder and back corner points. Taking into account the calculations based on a potential theory by Kriebel [1999] and Stansberg [2005], the

numerical results by the present Navier-Stokes solver, the second-order terms, for small steep waves of both long and short waves, confirm that, even the wave-wave and wave-cylinder interaction caused by linear incident wave, can lead to nonlinear wave field surrounding the cylinder which is labeled as weakly nonlinear wave amplification.

4.4-Effect of wavelength and steepness on inline wave force

The time series of the inline force, ($\mathbf{F_x}$), for cases of ($T=7s$ and $T=15s$, $H/L=1/16$) in addition to the free surface elevation at the front and back point of the cylinder are shown in Fig.4.14. Interaction of non-breaking regular waves with the given cylinder, no wave impact is observed. Four instants of time identical to aforementioned wave phase are considered, which are assigned by (a–d), respectively, to indicate the phasing of the various force reversals relative to the incident wave elevation. For both cases, upstream propagation of wave scattering Type1 during the interaction of incident wave phasing between zero up-crossing and the crest on the front point of the cylinder leads to a positive peak force in a downstream direction, time (a). Then, as the wave trough reaches the front point, the mound of water due to the propagation of wave scattering Type 2 in the downstream direction, results in a negative peak force in an upstream direction, time (b).

Increasing wavelength from short wave ($T=7s$) to long wave ($T=15s$), a secondary crest is observed in the inline force time history. This secondary crest is well-known as 'secondary loading cycle'. As soon as the edge waves which moving around the circumference of the cylinder in the upstream direction, collide at the front point, both wave scattering Type 2 and secondary load case are initiated, time (c), leading to positive (downstream) force on the cylinder. After that, when the second run-up in front points reaches its maxim level, the secondary load cycle becomes more apparent, time (c-d). As the edge waves driven back around the cylinder due to the arrival of the wave trough at back point, it is disappeared, time (d). Hence, the interaction of edge waves moving in upstream direction and the opposite incident wave is important for the creation of a secondary load cycle.

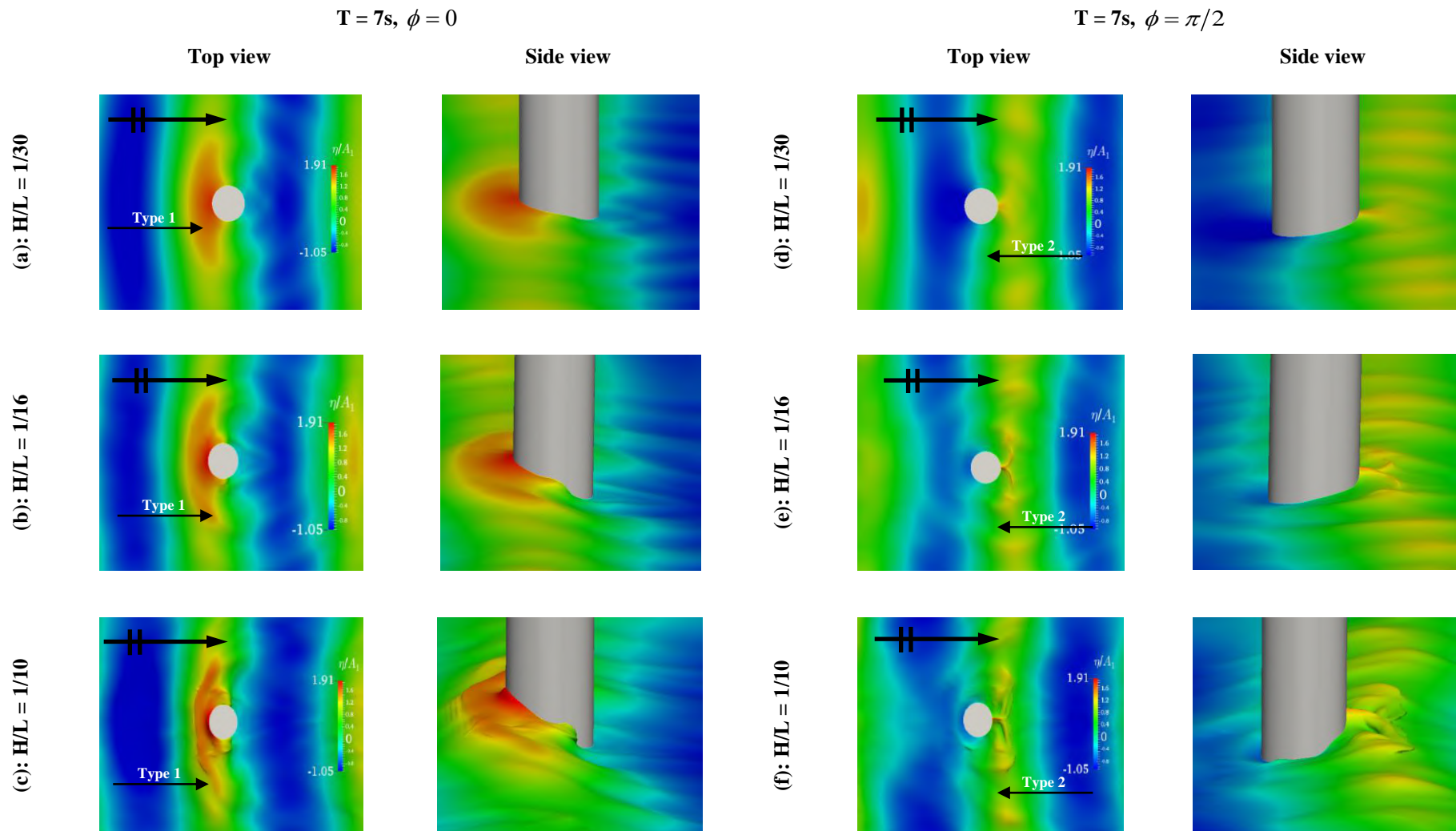


Fig 4.9. Spatial contours of the free surface elevation around cylinder under variation of wave steepness for short waves

$$T = 7s, \phi = \pi$$

$$T = 7s, \phi = 3\pi/2$$

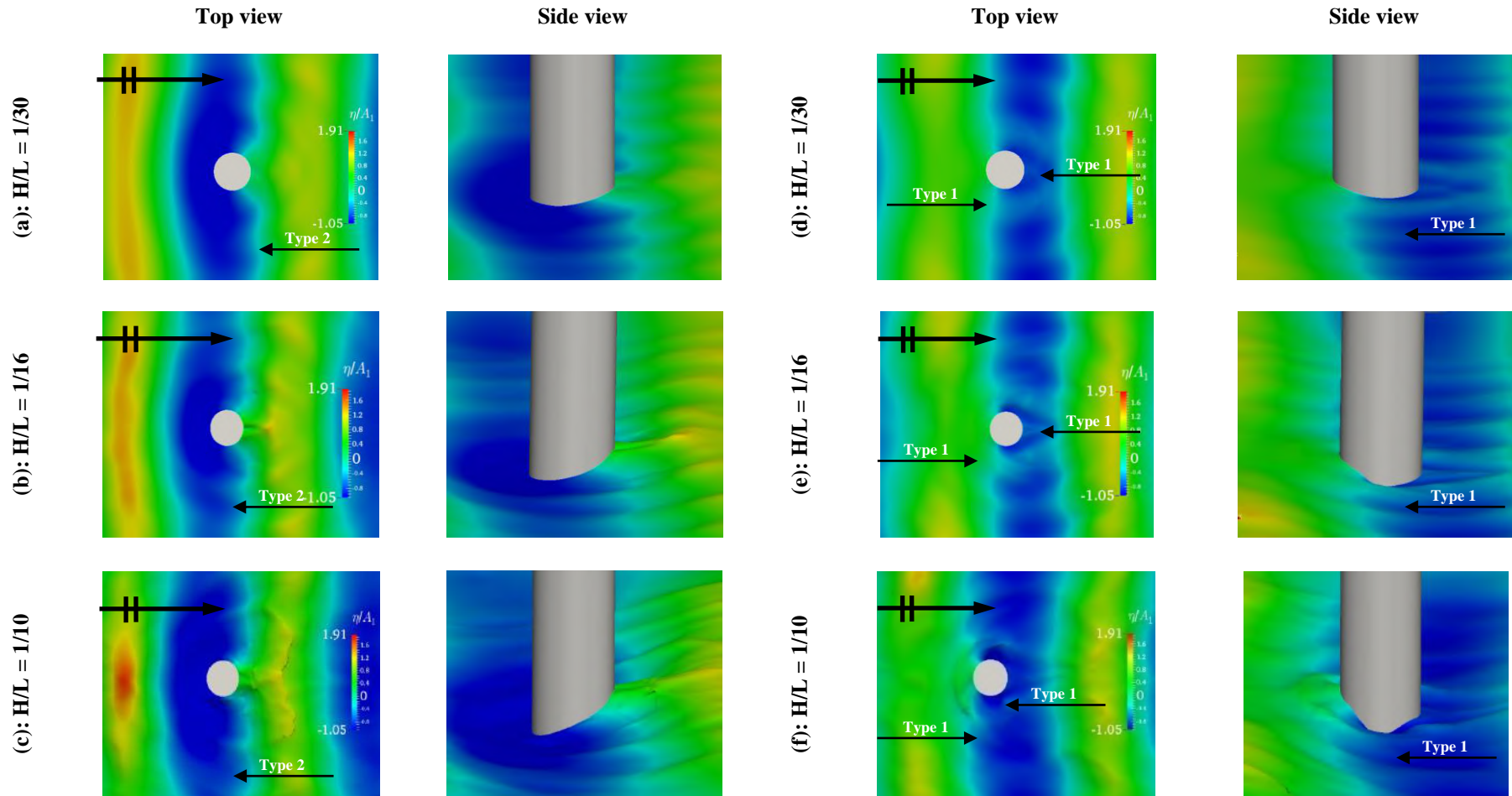


Fig 4.10. Spatial contours of the free surface elevation around cylinder under variation of wave steepness for short waves

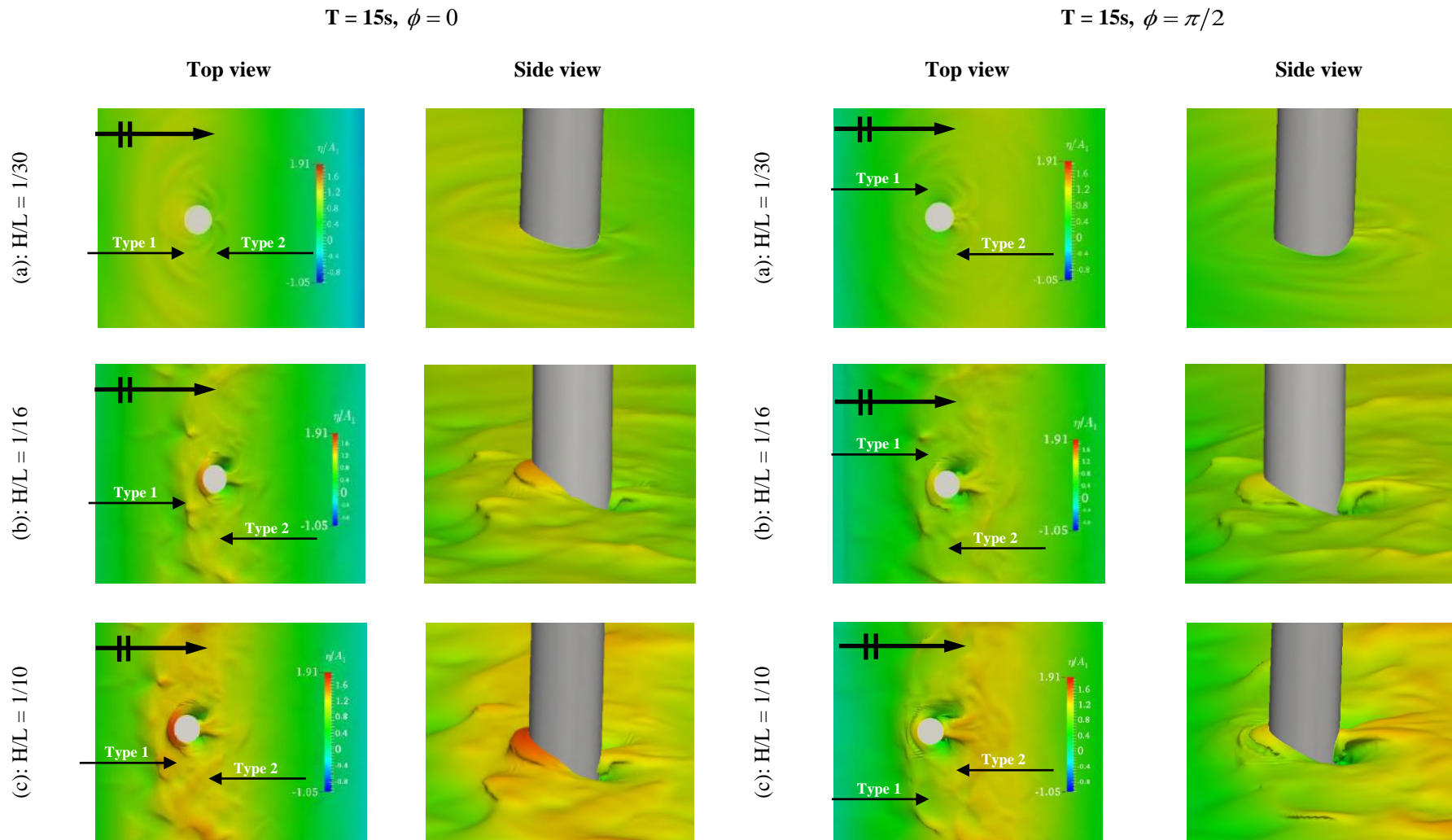


Fig 4.11. Spatial contours of the free surface elevation around cylinder under variation of wave steepness for long waves

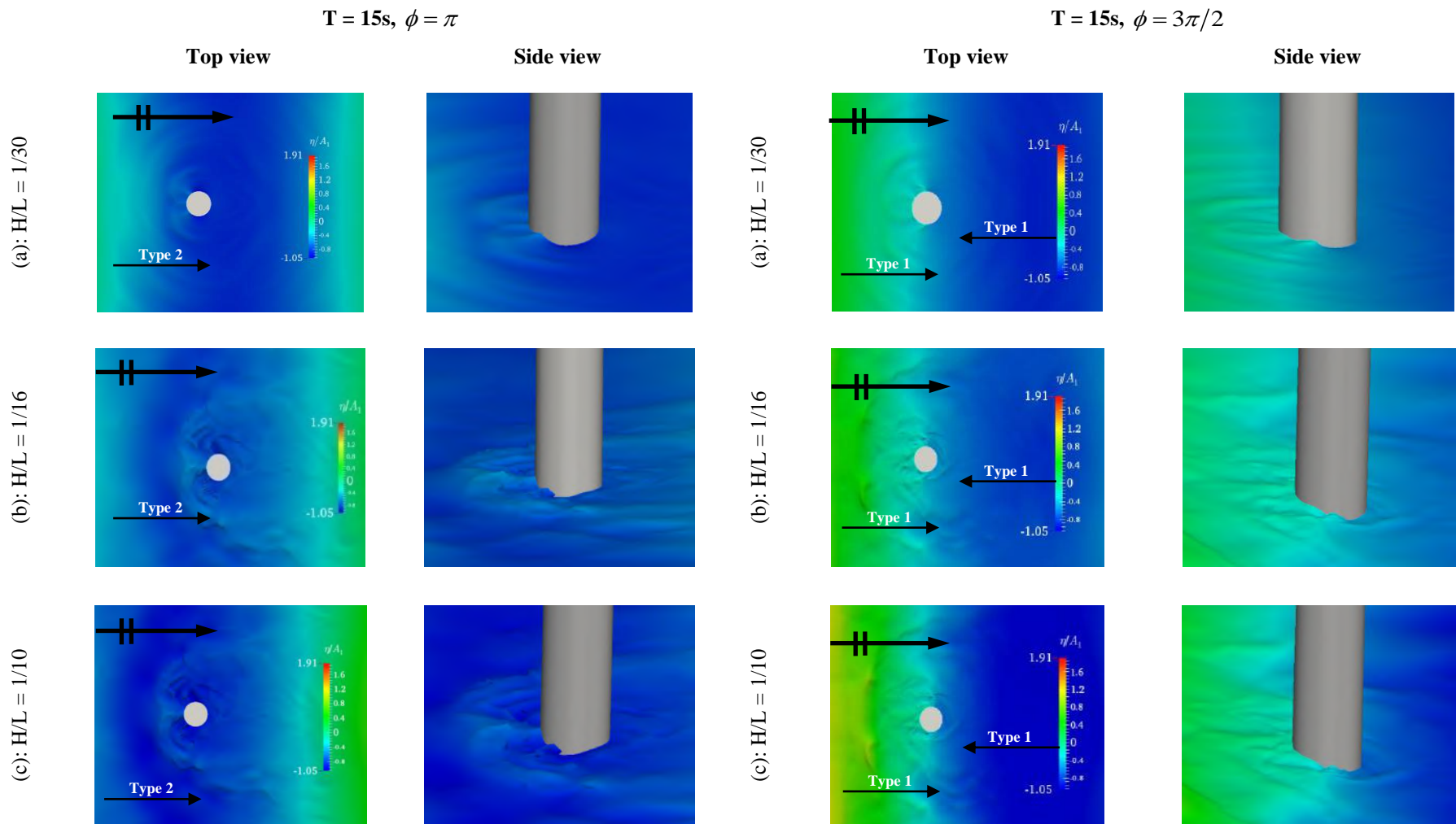


Fig 4.12. Spatial contours of the free surface elevation around cylinder under variation of wave steepness for long waves

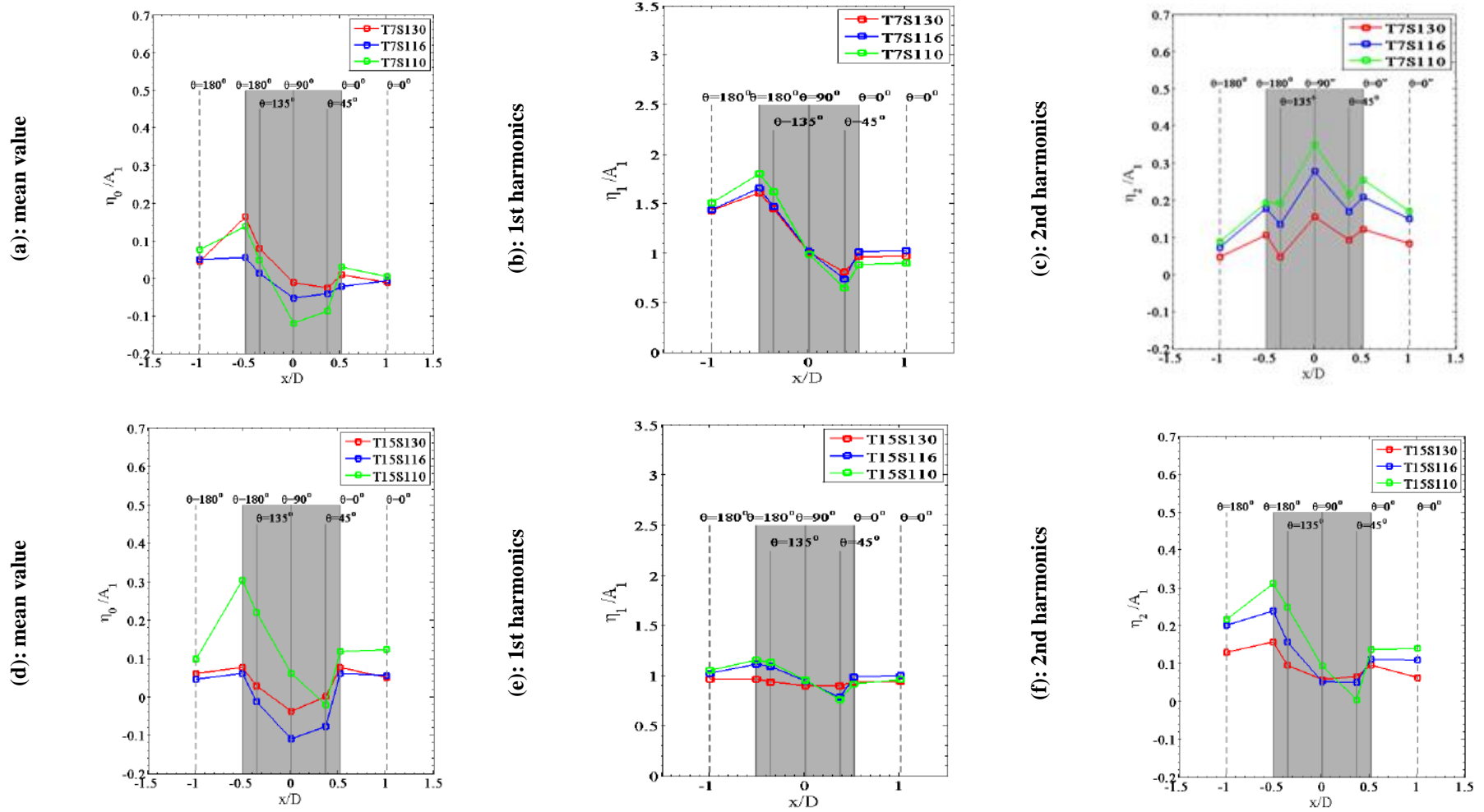


Fig 4.13. Comparison of normalized mean value and harmonics of wave run-up under variation of wave steepness for both short and long waves (vertical solid line ($r/D=0.513$) and vertical dash line ($r/D=1.0$))

Fig.4.15 illustrates the harmonic components of inline force for variation of wave length and wave steepness. It was noticed that for both short and long wave cases, from small to high steep waves the scattered wave field around the cylinder involves high harmonic wave run-up. However, it is seen that for short wave cases, the 1st harmonic of inline force is dominant and the higher harmonics are significantly small. Then increasing wavelength, the occurrence of the notable higher harmonic inline force experienced by cylinder becomes more evident. The physical origins of these harmonics are associated with the secondary load cycle which is due to scattering of high-frequency waves in the upstream direction. The occurrence of higher harmonic loading may in certain situations excite the structure at its natural frequencies and results in structural dynamic responses like Ringing which is known to be related to third-harmonic force, Paulsen.[2014]. Here, for long waves cases, even low steep waves ($H/L=1/30$), the harmonic loading involves at-least third harmonic where its magnitude is comparable with second-order harmonic and it increases with wave steepness. The nonlinearity in inline wave force is not as strong as surface elevation. This is because the local nonlinear effects are integrated out when computing the force, while the surface elevation shows the original local nonlinearity of wave run-up the cylinder.

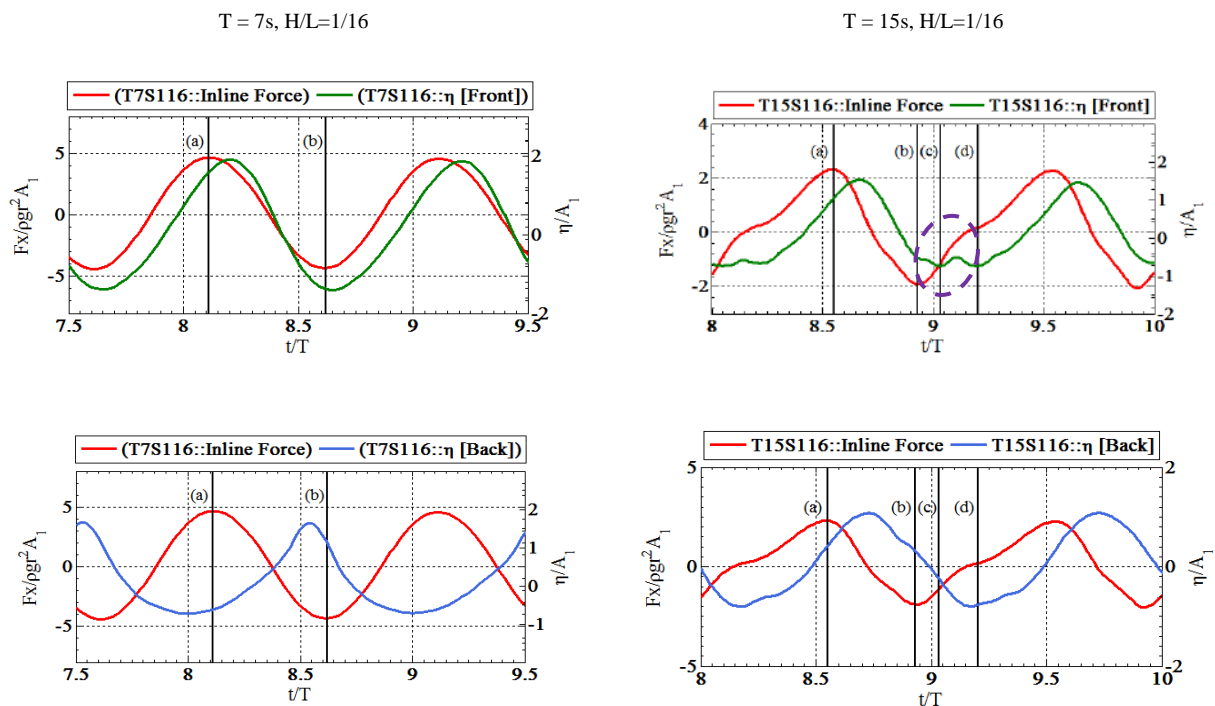


Fig 4.14. The inline force with free surface elevation time histories at the front and back point of the cylinder under wave condition of ($T=7s$ and $T=15s, H/L=1/16$)

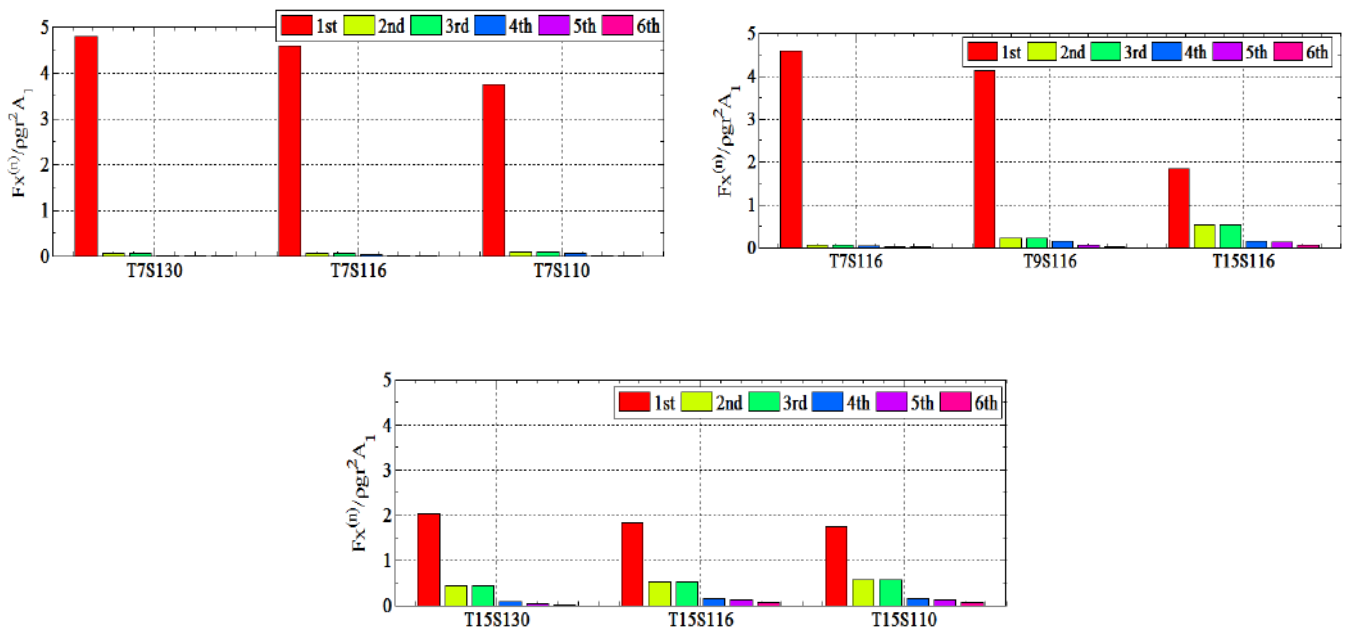


Fig 4.15. The first six harmonics of inline wave force under variation of wave steepness and wavelength.

4.5-Influence of potential flow, viscous and turbulence effects on wave Run-Up

The physics of the problem related to wave scattering and wave run-up around vertical, surface piercing cylinder generally involves potential flow, viscous and turbulence effects. In the case of potential flow effects, according to the literature review, the linear and second-order diffraction solutions are inappropriate for accurate estimation of nonlinear wave field and wave run-up around the cylinder. In addition, the importance of free surface elevation harmonics higher than second, particularly in the case of large non-dimensional parameters of wave diffraction and wave steepness is apparent. The classical (low-order) diffraction solutions are based on the assumption of very small steep incident waves (Airy wave, $H/L \ll 1$) and with regard to Stokes perturbation theory, the fully nonlinear free surface boundary condition is linearized around calm water line ($z=0$) using Taylor series expansion. Since the prescribed wave scattering Type 1&2 and also lateral edge waves involve high-frequency waves, they cannot be predicted correctly by classical (low-order) diffraction solutions with the aforementioned limited assumptions.

The fully nonlinear potential flow model can provide a reasonably accurate solution in this study to the extension where diffraction theory is valid. This model accounts non-breaking incident waves from small to high steepness and also the free surface boundary condition is treated fully nonlinear at the exact instantaneous location of the free surface, ($z = \eta$). There is

a study by Christou-[2009] where using fully nonlinear, multiple-flux Boundary Element Method, he did qualitative comparisons of the scattered wave-field between the numerical predictions and the laboratory observations of Swan et.al [2005], see Figs.4.16&4.17. He found that the proposed wave scattering Type 1&2 appear to be in good qualitative agreement with the laboratory observations and can be reasonably well modeled by a fully nonlinear potential flow solution. Hence, it is verified that, primarily, the high-order potential flow effects, contribute to the formation of the wave scattering Types 1&2 and lateral edge waves. In addition, it can be concluded that the viscous fluid or rotational flow is not the basic and initial requirements for these phenomena at the free surface. In addition to potential flow effects, the viscous and turbulent effects due to vortex formation and localized wave breaking also contribute to the physics of wave scattering and influence the intensity of wave evolution around the cylinder. Since these effects with their diffusive characteristics are not accounted by numerical models based on fully nonlinear potential flow theory and Euler equations, consequently, similar solutions are expected.

According to Table 3.1, as the (Re) number is in the order of (10^5 and 10^7) for both full and scale models, the flow regime around the cylinder is turbulent. Since the wave flow is a non-uniform oscillatory flow, the KC number governs the effect of (Re) number on the wave field surrounding the cylinder. Here, with regard to the given wave conditions, the (KC) number varies in the range of (0.5-7). For ($KC < 3$) the flow involves the inertia-dominated regime according to Sumer and Fredsøe-[2006]. Thus, as the flow does not travel far enough relative to the cylinder diameter to cause considerable boundary layer separation, the effect of the viscous vortex at back or front of the cylinder can be neglected, see vorticity contour of Fig.4.18(a&b). For ($3 < KC < 7$) the viscous effects and resultant boundary layer separation will be limited to at most developing a pair of attached and asymmetric vortexes for long wave cases, Sumer and Fredsøe-[2006]. It is worth to mention that no periodic vortex shedding or furthermore turbulent flow is expected due to insufficient time and space at the present (KC) number range. The incident progressive wave as a non-uniform oscillatory flow leads to an irregular pattern of the three-dimensional structure of the mentioned vortexes, see vorticity contour of Fig.4.18(c&d). The resultant vortex is swept in the up or downstream direction as the lateral edge waves travel around the cylinder. In the back of the cylinder, there is a return flow alongside the disturbances caused by wave scattering Type2 at the free surface which

enhances the momentum inside the boundary layer and contributing to the boundary layer separation induces some additional vortex, particularly for long wave cases.

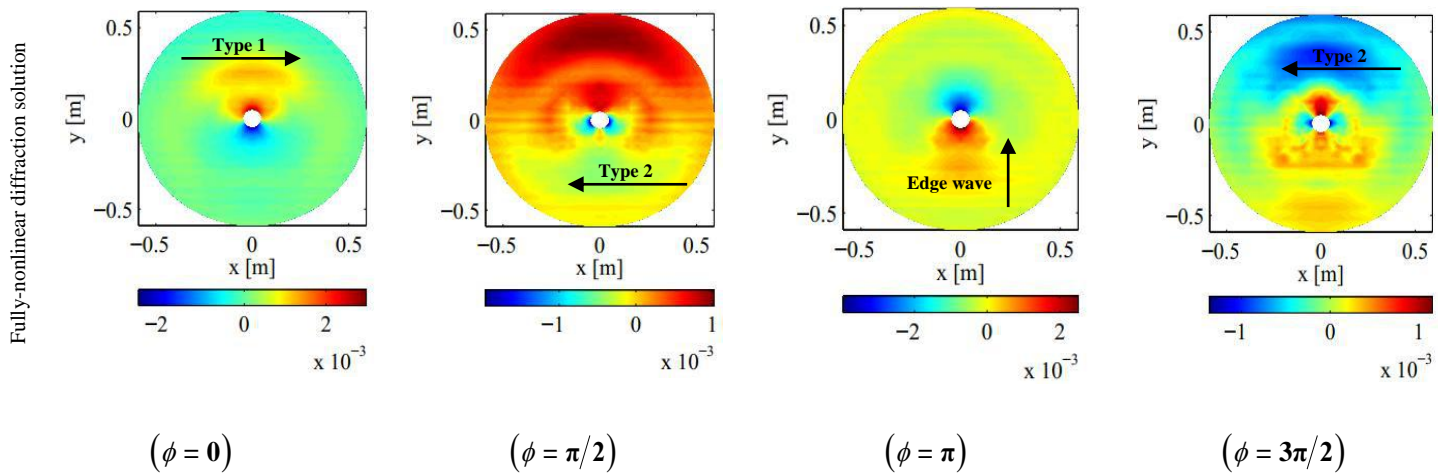


Fig 4.16. Numerical predictions of the scattered wave-field around a cylinder with a diameter of $D = 0.1\text{m}$. Christou-[2009]

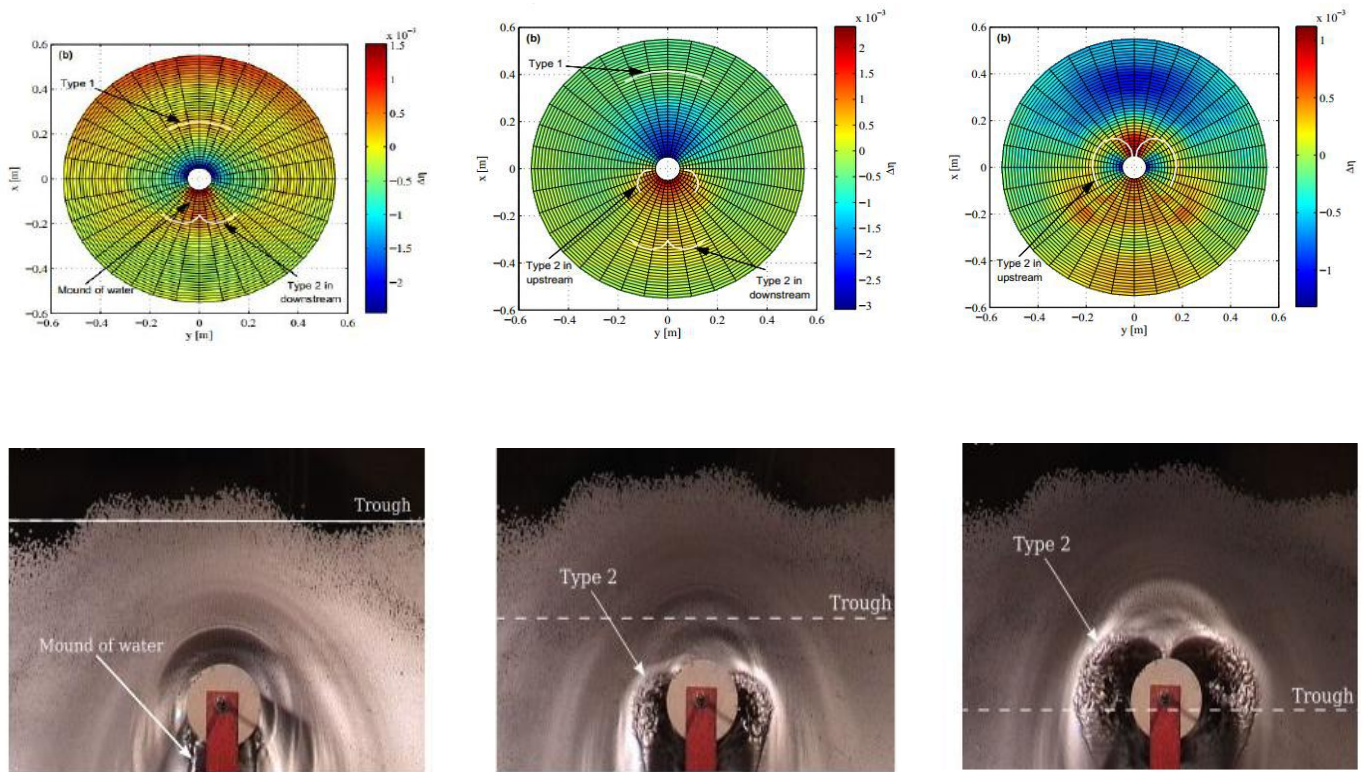


Fig 4.17. Qualitative comparisons of the scattered wave-field between the numerical predictions and the laboratory observations of Swan et al [2005] with a diameter of $D = 0.1\text{m}$, Christou-[2009]

The wave field around the cylinder also involves localized wave breaking and air entrainment during the wave-structure interaction that with regard to the assumption of non-breaking incident waves it is considered as the main cause of turbulence flow regime. The progressive lateral edge waves as they propagate in up or downstream direction, there is an energy and consequently vertical extension reduction. The primary cause of this is related to the energy transfer away from the cylinder during run up/down and wash in the radial direction which is accounted as potential flow effects. There is additional energy reduction which is caused by turbulence effects. The energy dissipation due to local wave breaking that occurs as the wave run-down mainly in the case of lateral edge waves and then both wave scattering Type 1&2 is accounted as turbulence effects. Increase in wave diffraction or wave steepness number, separately or together, results in more interaction and then more edge wave energy reduction.

The lateral edge waves energy reduction is more apparent in the 1st harmonic distribution of free surface elevation around the cylinder, see Fig.3.8. In the case of present CFD based Navier-Stokes solver with No-Turbulence ($\mu_t = 0$), as it is observed for both short and long cases under incident wave steepness of ($H/L=1/30$, $H/L=1/16$), there is a good agreement between numerical solution and experimental data. This suggests that the contribution of turbulence effects is not major for these wave steepnesses and the edge wave reduction is more due to potential flow effects and then the diffusion term in Navier-stokes equation with only fluid viscosity can reasonably account the turbulence effects. In the case of high steep waves, ($H/L=1/10$), local wave breaking is intense and turbulence effects are important, therefore in order to respect the physics of the problem, in URANS approach, utilization of turbulence model is necessary.

In the case of a change in wave diffraction number with constant wave steepness, as it decreases from short to long wave cases, the presence of a viscous vortex at the back of cylinder becomes more apparent. They reduce the energy of the lateral edge waves that reach the back of the cylinder and in parallel to the small diffraction effect, results in less wave run-up height and less steep waves at the back of the cylinder. On the other hand, they contribute to the mound of water and consequently increment of the resultant edge waves energy propagating in upstream to form wave scattering Type 2 at the front point. Decreasing the wave diffraction from short to long waves, the intensity of local wave breaking and consequently turbulence effect around the cylinder decreases. Therefore there is less energy

reduction of lateral edge waves which is apparent in the 1st harmonic pattern, see Fig.4.7, particularly at the back-corner point, ($\theta = 45^\circ$) where this reduction is more for short waves (large diffraction). Change the wave steepness while diffraction number is constant, there is no considerable change in KC number and consequently the intensity of vortexes at the back of the cylinder. On the other hand, as the wave steepness increases the local wave breaking and turbulence effects becomes important. As it is seen in Fig.4.13(b&e), for the 1st harmonics, there is more reduction for high steep wave ($H/L=1/10$) which is apparent at both back-corner and back point of the cylinder which eventually results in lower run-up height at the back of the cylinder.

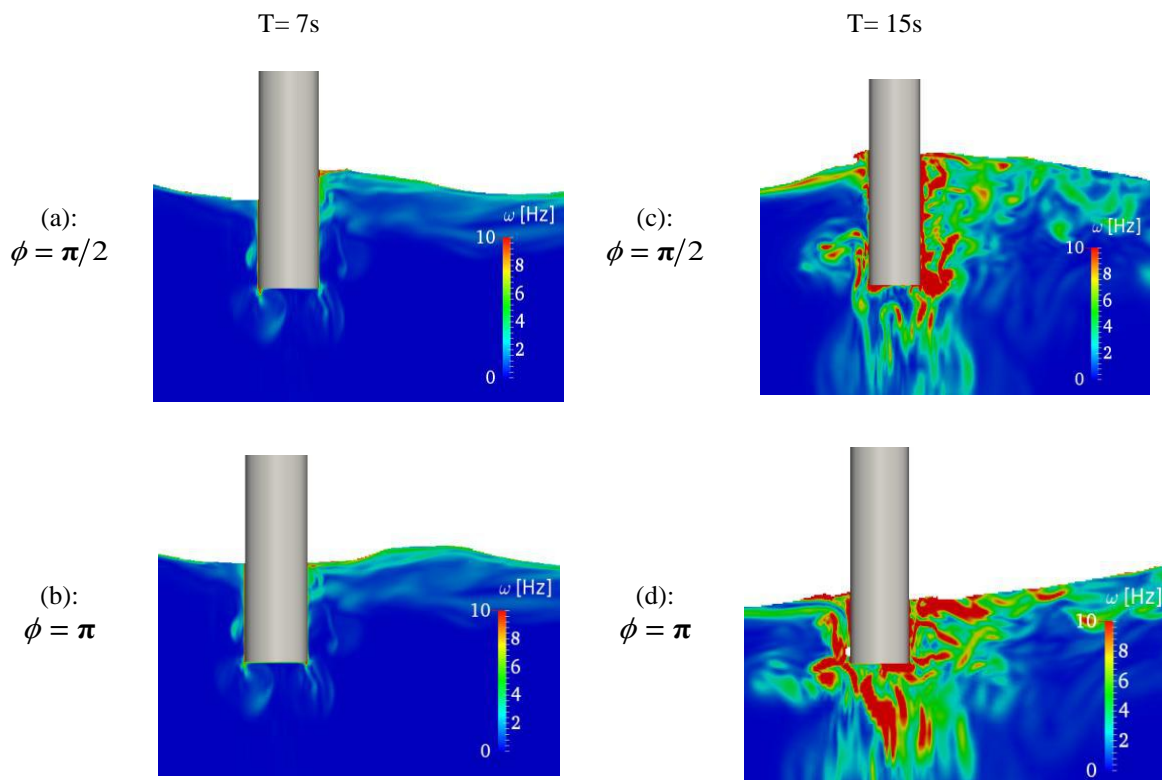


Fig 4.18. Vorticity magnitude contour along the centerline ($y = 0$) of the cylinder

4.6-Effect of submerged geometry on wave Run-Up

In this section, the influence of a change in underwater volume on the wave field surrounding the cylinder and corresponding wave run-up harmonics is investigated. Here, the change in underwater volume is associated to change in vertical surface-piercing cylinder draft, with or without attached substructure. In this regard, the simulations are conducted for four geometries which are illustrated in Fig.4.19. The geometries related to change in the draft without attached substructure include two cylinders of Truncated1 (draft 1.5D),

Truncated2 (draft 0.5D). Truncated cylinders, are used for buoyancy in a range of floating structures including semi-submersibles, spar buoys and Tension-Leg Platforms (TLPs) as well as floating offshore wind applications. The other two geometries of SubStr1 and SubStr2 are composed of a substructure and the two cylinders of Truncated1 and Truncated2, respectively. This attached substructure is a disk with circular cross-section and diameter of (3D) which can be taken as heave plate or part of the pontoon of offshore floating oil/gas platforms (Semi-submersibles, TLPs) and base column of floating platform based offshore wind turbines.

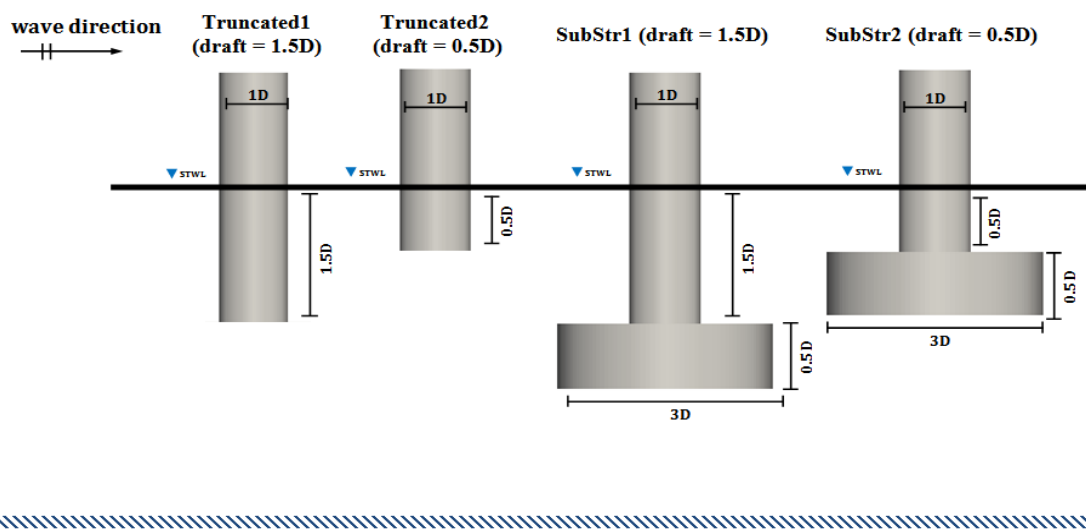


Fig 4.19. The geometries related to change in vertical cylinder draft, with or without attached substructure. under the wave condition of $(T=7s, H/L=1/16)$ in deep water

The wave condition of $(T=7s, H/L=1/16)$ is considered for the present study. As it is seen in Fig.4.19, the width of each cylinder at the intersection of STWL and the circular cross-section is the same for all of the geometries and equal to $(1D)$ which results in identical wave diffraction number. In the present analysis, the cylinder geometry of Truncated1 is taken as reference2 case. The spatial contour of wave field around the given geometries for the arrival of three wave phases of the crest, trough and zero up crossing at the front stagnation point of the cylinder is illustrated at Figs. (4.21-4.23) by the top and side view. Fig.4.20 shows the comparison of normalized mean value and harmonics of the wave elevation around the given geometries in terms of wave probes location (x/D) . Change in underwater volume as it can, primarily, affect the reflection, is important in the context of wave scattering and resultant wave amplification around the cylinder. Comparing the simulation results by cylinder of

Truncated1 and Truncated2 the wave scattering and also harmonic pattern are maintained. However, the reduction in the draft and consequently reflection by underwater volume for cylinder of Truncated2 lead in the reduction of both wave elevation and corresponding harmonics at the given wave probes, see Figs. (4.21-4.23) (a&b). On the contrary, as mentioned in section 4.2, in the case of cylinder of Truncated1 and also increasing the draft more than $(1.5D)$, the excess reflection by underwater volume and also the developed vorticity from the cylinder bottom, cannot reach the free surface and affect the wave scattering and related wave run-up around the cylinder.

For SubStr1 in comparison to the reference2 case where they both have an identical draft, the effect of attached substructure is apparent. As it is seen in Figs. (4.21-4.23) (c) and also in Fig.4.20, the attached substructure enhances the surrounding wave field and related harmonics. Taking to account the identical results by Bottom-Mounted and Truncated1 cylinders, there is a weak wave-substructure interaction for the case of SubStr1 at a draft of $(1.5D)$ which leads in small change while maintaining the trend for the mean value and first five harmonics in comparison to the reference2 case, see Fig.4.20. The wave field around SubStr1 experiences locally shallow water due to the presence of attached substructure. In shallow water, as we know, the waves are non-dispersive and the propagation speed depends on the local depth. Therefore as it is seen in Figs. (4.21-4.23) (c), there is a reduction in wave scattering propagation velocity which is more evident by steeper crest and flatter trough at the circular extension that is affected by attached substructure.

The effect of attached substructure on wave run-up which is similar to the effect of the cone-shaped foundation is also involved wave upwelling. De Vos et al. [2007], showed that the shape of the foundation substantially affects the maximum run-up level where for the cone-shaped foundation it leads to increasing the expected run-up value. During the interaction of wave passing the cylinder with the substructure, a reflection of water particles in an upward direction results in a local free surface amplification which is known as wave upwelling effect, Taylor-[1989]. With regard to the assumption of identical diffraction number and incident wave condition, wave upwelling locally steepens the wave scattering and contribute to wave amplification around the vertical cylinder. It was explained in section 4.2 that increasing the wave steepness enhances the wave kinematics and results in higher and steeper run-up which is also accompanied by a notable local wave breaking around the cylinder.

For the cylinder of Truncated2, it was shown that there is a small reflection by underwater volume due to smaller draft comparing to the reference2 case. In the case of SubStr2 which is a combination of cylinder Truncated2 and the attached substructure, this small reflection is augmented by the wave upwelling. Thus, there is significant enhancement by wave scattering and run-up, see Figs. (4.18-4.20) (d) and also corresponding harmonics, see Fig.4.20. Comparing the reference2 case and SubStr2, the significant increment for 1st harmonics is observed at Fig.4.20. This increment is about 10% and 20% at front and back stagnation point, respectively. In addition, there is a considerable reduction from front corner to back corner in comparison to the other cases for 1st harmonics. This is caused by energy reduction of lateral edge waves which in this case it is more related to the notable local wave breaking/dissipation. For SubStr2, the collision of lateral edge waves at back stagnation point in combination with wave upwelling results in considerably strong local flow and higher and steeper run-up which is more evident at the spatial contour of Fig.4.22(d). It was explained before that, the interaction of wave trough at back stagnation point leads in the reduced run-up in the form of wave scattering Type1. As it is seen in Fig. (4.21), this run-up is less evident for cylinder Truncated 1 and Truncated 2 while it is more evident in the case of SubStr1 and SubStr2. Accordingly, as the presence of substructure becomes apparent, the harmonics higher than 1 and also mean value at back stagnation point are increased.

During the movement of the lateral edge waves in the upstream direction, there is strong and nonlinear interaction with opposing incident wave at or about the trough which results in large 2nd and 3rd harmonics and also mean value at the back corner, shoulder and front corner points, see Fig.4.20. Considering the harmonics higher than first for all given geometries except SubStr2, the nonlinearity is more notable at half backward part while in the case of SubStr2, the nonlinearity at front stagnation point is also significant which is evident in the 2nd harmonics and mean value. This is related to the occurrence of the second run-up at this point, see Fig 4.22(d). The edge waves traveling in an upstream direction can pass the shoulder point but eventually can reach the forward corner point before the arrival of the zero-up crossing. This is associated to the considerable reduction of edge waves energy cause by strong interaction with the vertical cylinder and also insufficient propagation time as a result of small propagation speed and also incident short wave condition. Therefore occurrence of this second run-up at the front point is related to the wave scattering Type1 which is caused by the interaction of some point about the incident wave trough and the attached substructure.

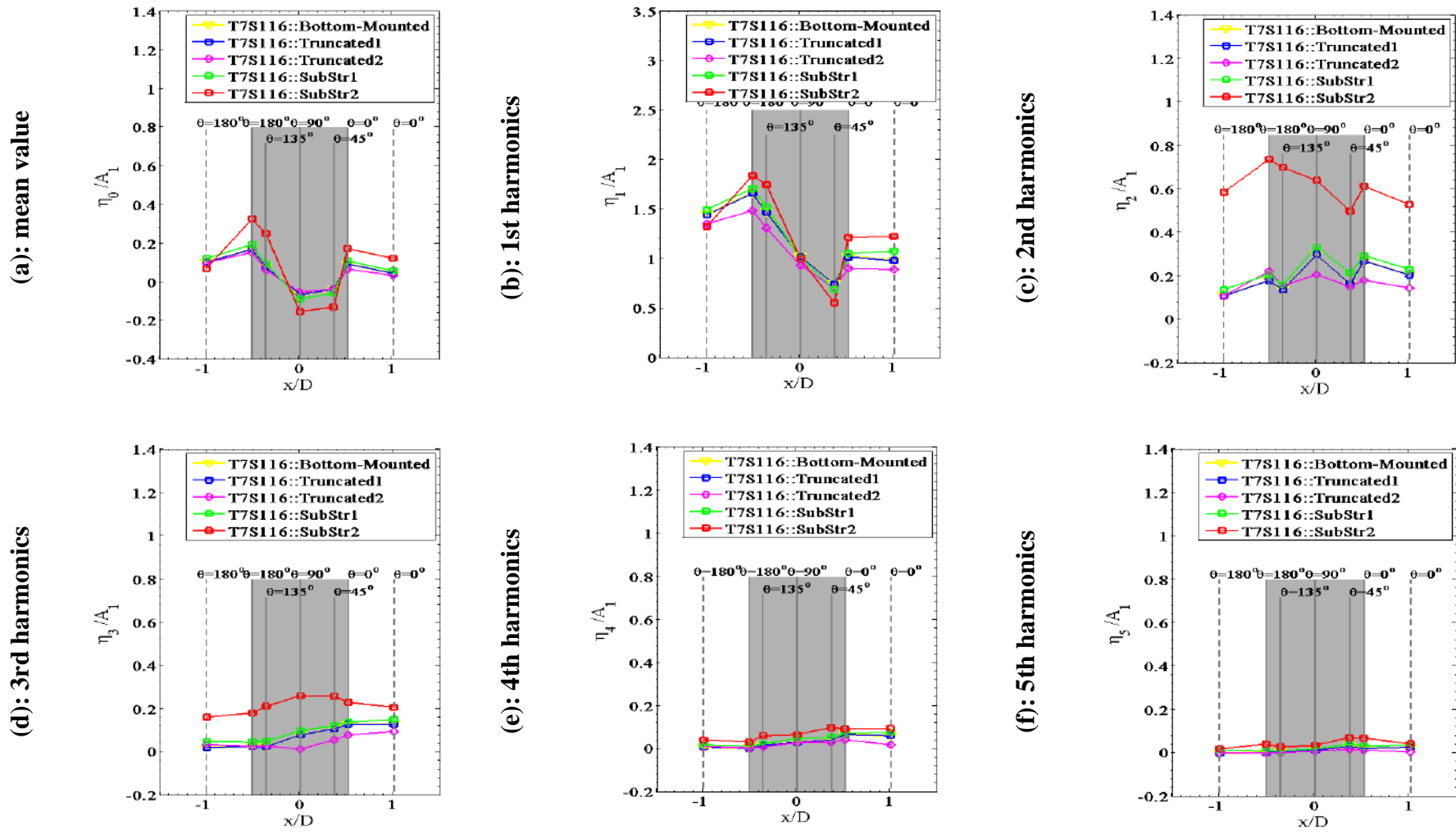


Fig 4.20. Comparison of normalized mean value and harmonics of wave run-up around the vertical cylinder under wave condition of (T=7s, H/L=1/16), (vertical solid line (r/D=0.513) and vertical dash line (r/D=1.0))

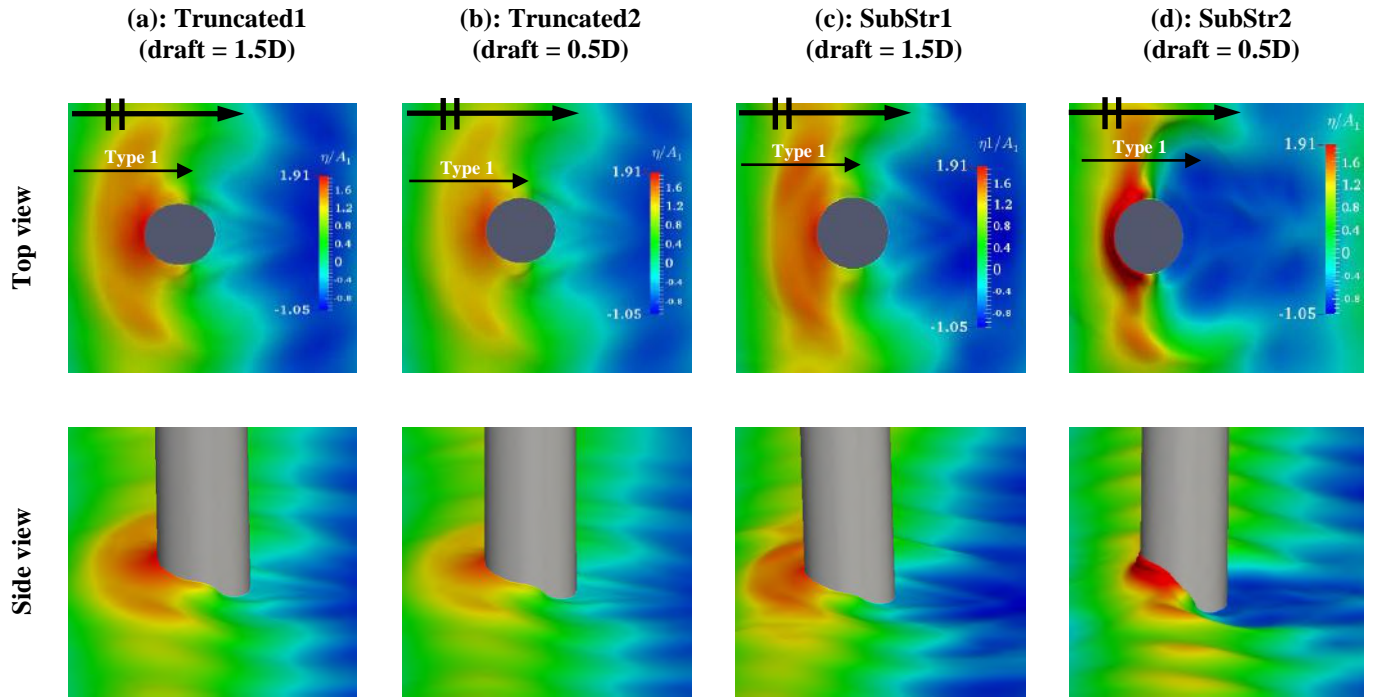


Fig 4.21. Spatial contours of the free surface elevation around the vertical cylinder under wave condition of ($T=7s$, $H/L=1/16$), with the arrival of wave crest at the front point

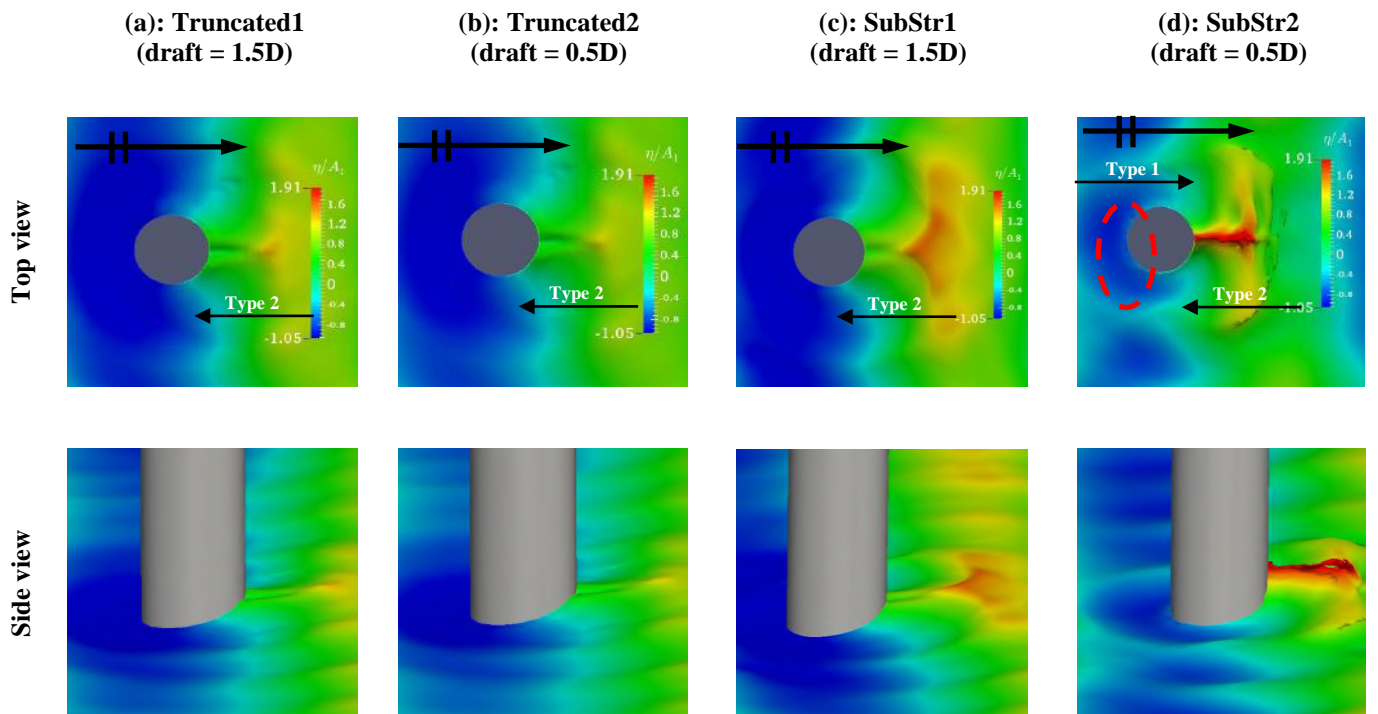


Fig 4.22. Spatial contours of the free surface elevation around the vertical cylinder under wave condition of ($T=7s$, $H/L=1/16$), with the arrival of wave trough at front point

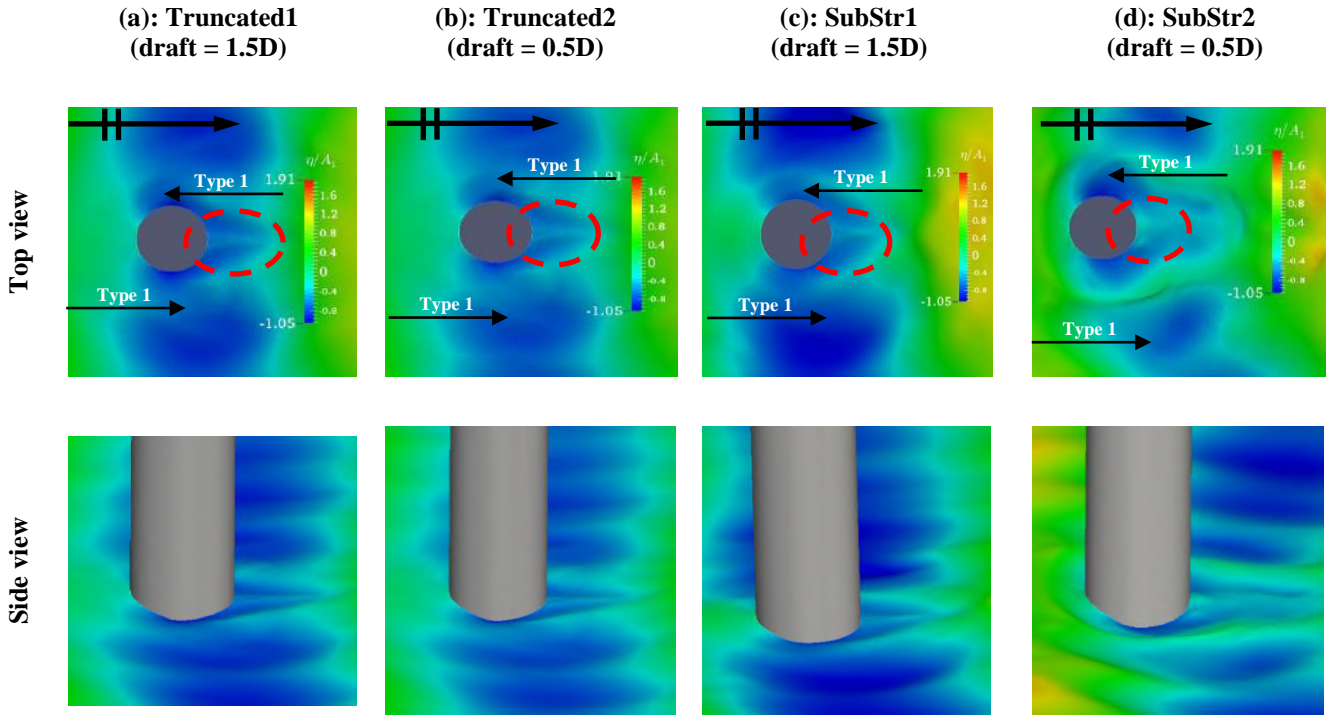


Fig 4.23. Spatial contours of the free surface elevation around the vertical cylinder under wave condition of ($T=7s$, $H/L=1/16$), with the arrival of the wave zero up crossing at the front point

4.7-Effect of cylinder cross-section on wave Run-Up

The purpose of this section is to study the influence of a change in cross-section on the wave field and wave amplification around the cylinder and also corresponding harmonics, taking into account the aforementioned wave scattering Type1&2. The change in cross-section is identified by the corner ratio ($r_c/R=0$) which is defined as the ratio of corner radius (r_c), to the half cylinder width (R). In this regard, with the assumption of truncated and vertical surface piercing cylinders, five cross-sections varying within the range of ($0 \leq r_c/R \leq 1$) being selected for the purpose of this study. These cross-sections include circular ($r_c/R=1$) and four non-circular with corner ratio which varies from round ($r_c/R=0.75$) to sharp ($r_c/R=0$), see Fig.4.24. The examples for such cross-sections are the columns deepwater offshore structures such as of conventional and extended Tension Leg Platforms(TLPs) and spars platforms. In the present study, the corresponding simulations are conducted under the wave condition of ($T=7s$, $H/L=1/16$). As it is seen in Fig.4.24, the width at the intersection of still waterline and each cross-section is equal to (1D). Hence, considering the definition of

wave diffraction number, all of the given cross-sections undergoes nominally identical diffraction.

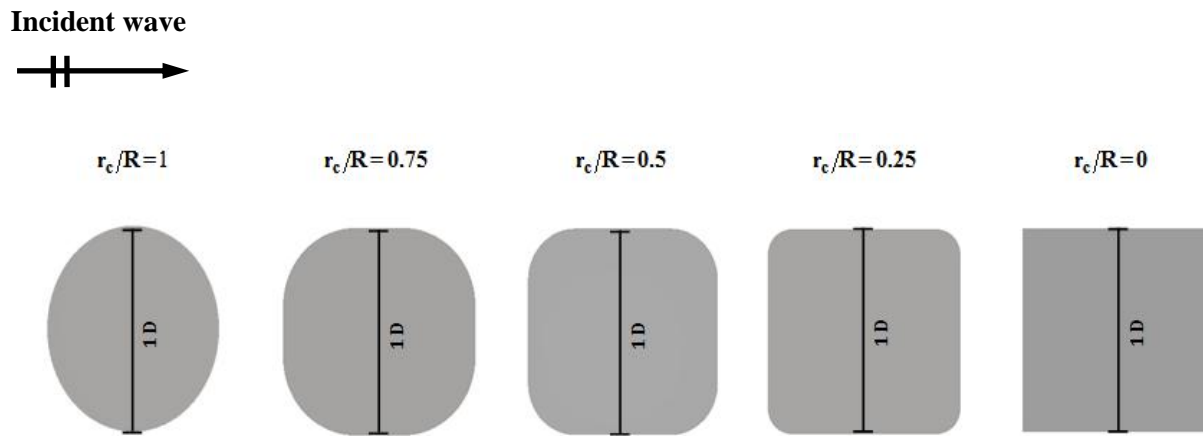


Fig 4.24. The geometric variation of the cross-section for truncated cylinders corresponding to five given value of corner ratio.

Systematic reduction of corner ratio, the cylinder circumference increases. This causes more wave-cylinder interaction and the assumption of an identical incident wave condition, it leads to larger diffraction. Accordingly, as the diffraction increases, the edge waves experience more energy reduction where, here, it is more related to the energy damp caused by run-up/wash down process. Changing the cross-section from circular to square with sharp corners, the presence and influence of corner on the wave field around the cylinder becomes more evident. Corner effect is related to the formation of induced edge waves due to the interaction of corner with the incident wave horizontal velocity. These induced edge waves are also accompanied by developing attached vortexes under present wave condition.

Figs (4.25-4.29), show the spatial contour of wave evolution around the given cross-section by the top and side view. Fig.4.25 illustrates the maximum run-up due to the interaction of incident wave crest and front of the cylinder in the form of wave scattering Type1 for all given cross-sections. As it is observed the maximum run-up height is enhanced following systematic reduction of corner ratio. This increment may be related to the number of stagnation points at front of the cylinder which increases as corner ratio reduces. At these stagnation points, more water particles are brought to rest in front of the cylinder. This increases the dynamic pressure and raises the water level and consequently, the cylinder undergoes the so-called breakwater effect, Repalle et al. [2012], which eventually leads in the higher run-up in front of the cylinder. Moreover, initiation of induced edge waves at both

front and back corners in the downstream direction is observed in Fig.4.25, for cases of $(r_c/R=0.5)$, $(r_c/R=0.25)$ and $(r_c/R=0)$.

The lateral edge waves propagate downstream, they collide and devolve along the cylinder centerline as wave scattering Type2 to form the second reduced run-up at the back of the cylinder, see Fig.4.26. Then, this second run-up is enhanced by the arrival of the wave crest. However, changing the cross-section from circular to square with sharp corners, there is a notable reduction in both run-up height and steepness at the back of the cylinder. This is caused by the weak edge waves collision at cylinder back which is related to notable energy reduction due to large diffraction and may also be due to attached vortexes. The induced edge waves by the front corner points cannot propagate furthermore in downstream and contribute in the run-up at cylinder back due to the mentioned lateral edge waves energy reduction.

In Fig.4.27, it is seen that following the passage of zero-down crossing by the cylinder back that the lateral edge waves are driven in upstream. However due to the corner effect in the cases related to $(r_c/R=0.5)$, $(r_c/R=0.25)$ and $(r_c/R=0)$, the interaction of negative horizontal velocity with corners leads in induced edge waves by both back corners and front corners. The resultant induced edge waves at front corners developing and propagating toward the cylinder centerline to initiate occurrence of wave scattering Type2 at front of the cylinder for the related cases. The induced edge waves by back corner points cannot reach the front of the cylinder due to notable energy reduction. In addition, as it was shown in section 4.1 for a cylinder with a circular cross-section, the lateral edge waves pass the shoulder can eventually reach the front corner points before the arrival of zero-up crossing at front of the cylinder. Consequently, with the assumption of identical wave condition, the lateral edge waves for the other cross-sections where diffraction is larger, cannot reach the front of the cylinder, as well.

Interaction of negative horizontal velocity, following the passage of zero-down crossing at cylinder back, initiates wave scattering Type1 for all given cases. In the same way, the interaction of positive vertical velocity following the passage of wave trough initiates wave scattering Type1 at front of the cylinder for all given cases. Fig.4.28(c-e), indicate the occurrence of developed wave scattering Type2, for cases related to $(r_c/R=0.5)$, $(r_c/R=0.25)$ and $(r_c/R=0)$. This is caused by the run-up due to the collision of induced

edge waves at some point between incident wave phases of the trough and zero-up crossing by at cylinder front. Then as the wave passes the cylinder, the occurrence of wave scattering Type1 at both front and then at the back of cylinder becomes more apparent. This is evident, particularly as the number of stagnation point due to corner effects increases, See Fig.4.29. Additionally, the third interaction of induced edge waves with back corner points with the arrival of a wave trough at the back of cylinder is observed in Fig.4.29(c-e) for cases related to $(r_c/R = 0.5)$, $(r_c/R = 0.25)$ and $(r_c/R = 0)$.

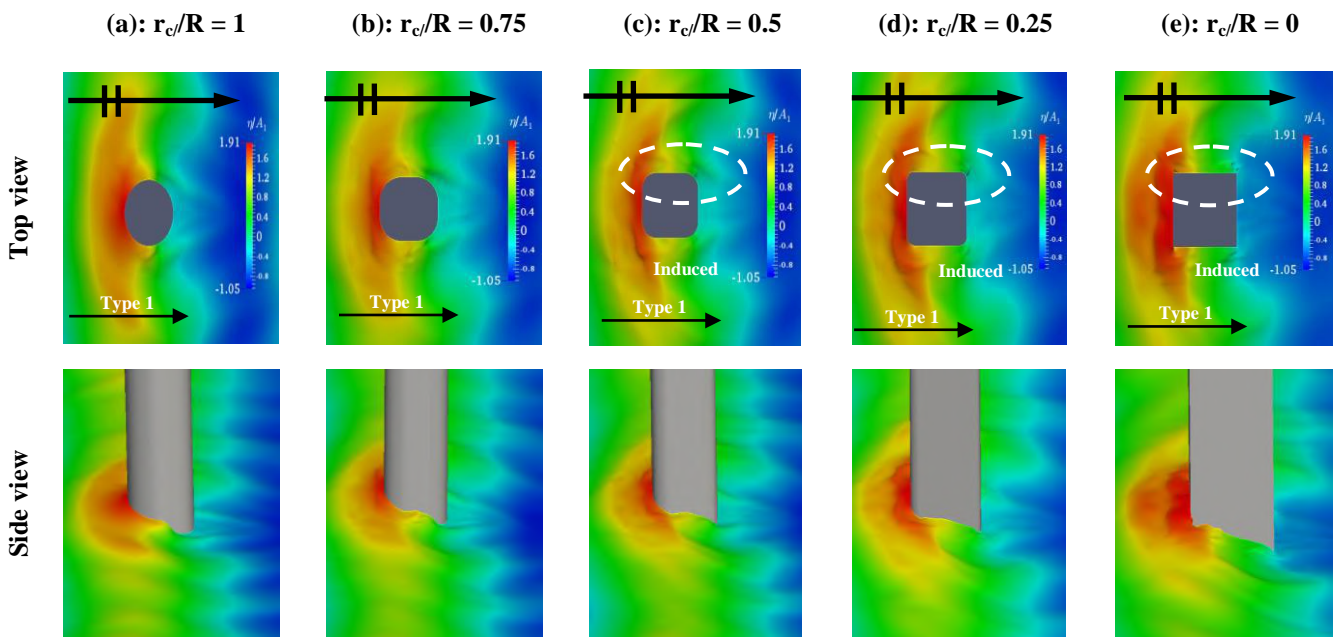


Fig 4.25. Spatial contours of the free surface elevation around the cylinder for cross-section variation under wave condition of $(T=7s, H/L=1/16)$, with the arrival of wave crest at the front point

The comparison of normalized mean value and harmonics of the wave elevation around the given cross-section in terms of wave probes location (x/D) is presented in Fig.4.30. For the 1st harmonics, changing the corner ratio, the trend for all simulation is the same but there is a systematic change in value. It was shown that decreasing the corner ratio, run-up height increases where similarly it is observed as an increment in 1st harmonics at front point of the cylinder, see Fig.4.30(b). This increment is about 14% comparing the 1st harmonics for the cases of $(r_c/R = 1)$ and $(r_c/R = 0)$. The reduction from the front to back corner point is more apparent for $(r_c/R = 0)$ which consequently results in lower value at the back of the cylinder comparing to the other cases.

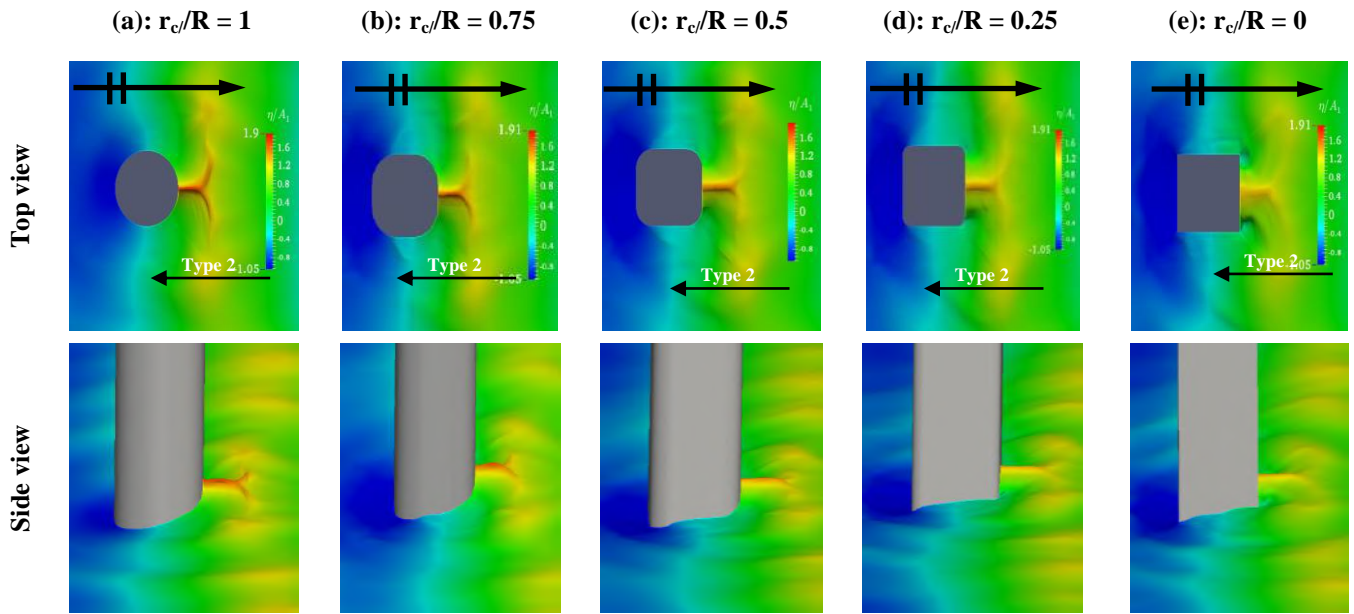


Fig 4.26. Spatial contours of the free surface elevation around the cylinder under wave condition of ($T=7s$, $H/L=1/16$), with the arrival of wave crest at the back point

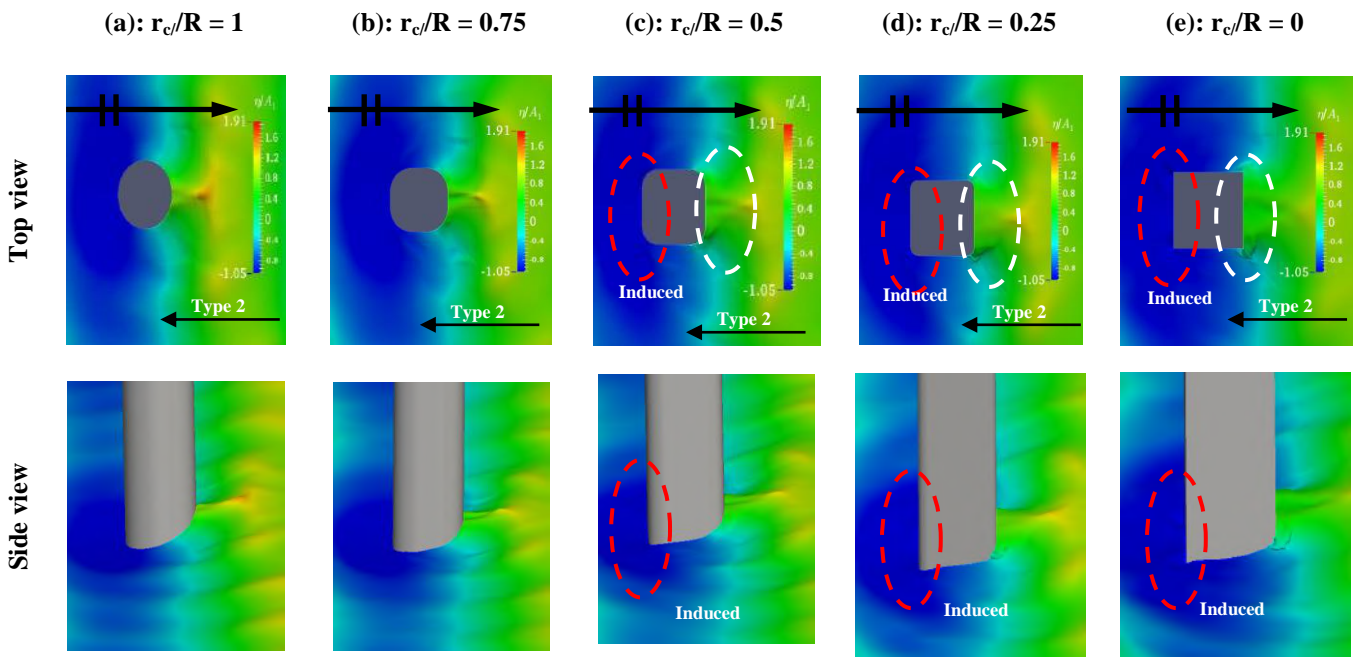


Fig 4.27. Spatial contours of the free surface elevation around the cylinder under wave condition of ($T=7s$, $H/L=1/16$), with the arrival of wave trough at front point

For 2nd harmonics, the harmonic pattern varies while there is still systematic change in value. In the case of front point, there is an increment by 2nd harmonics from ($r_c/R=1$) to ($r_c/R=0$), see Fig.4.30(c). This is related to the occurrence of a second run-up at this point

and it is evident in the case of $(r_c/R=0.5)$, $(r_c/R=0.25)$ and $(r_c/R=0)$, see Fig.4.28(c-e). This increment is also considerable by 3rd harmonics at this point, see Fig. 4.30(d). The same as 1st harmonics, the systematic reduction of corner ratio, the 2nd harmonics at back point reduces which is also observed at given higher harmonics. In the case of a circular cross-section, the energy of lateral edge waves is more than the other cases. Consequently, there is strong edge wave collision which results in steeper and higher run-up at back point. In the case of shoulder point as it seen there is notable peak value by 2nd harmonics for the case of $(r_c/R=1)$ which is caused by the interaction of wave trough and lateral edge waves traveling in the upstream direction. As the corner ratio and consequently energy of the lateral edge waves reduces, there is also a reduction in 2nd harmonics at shoulder point. This is related to the weak interaction of edge waves with opposing incident wave as it occurs at some point before the arrival of wave trough at shoulder point. As the corner effect becomes important, considerable 2nd and 3rd harmonics are observed at both back corner and front corner points. The harmonic values for the back corner point are higher which is related to the formation and interaction of induced edge waves at these points. As it was shown this occurs three times for back corner points while two times for front corner points.

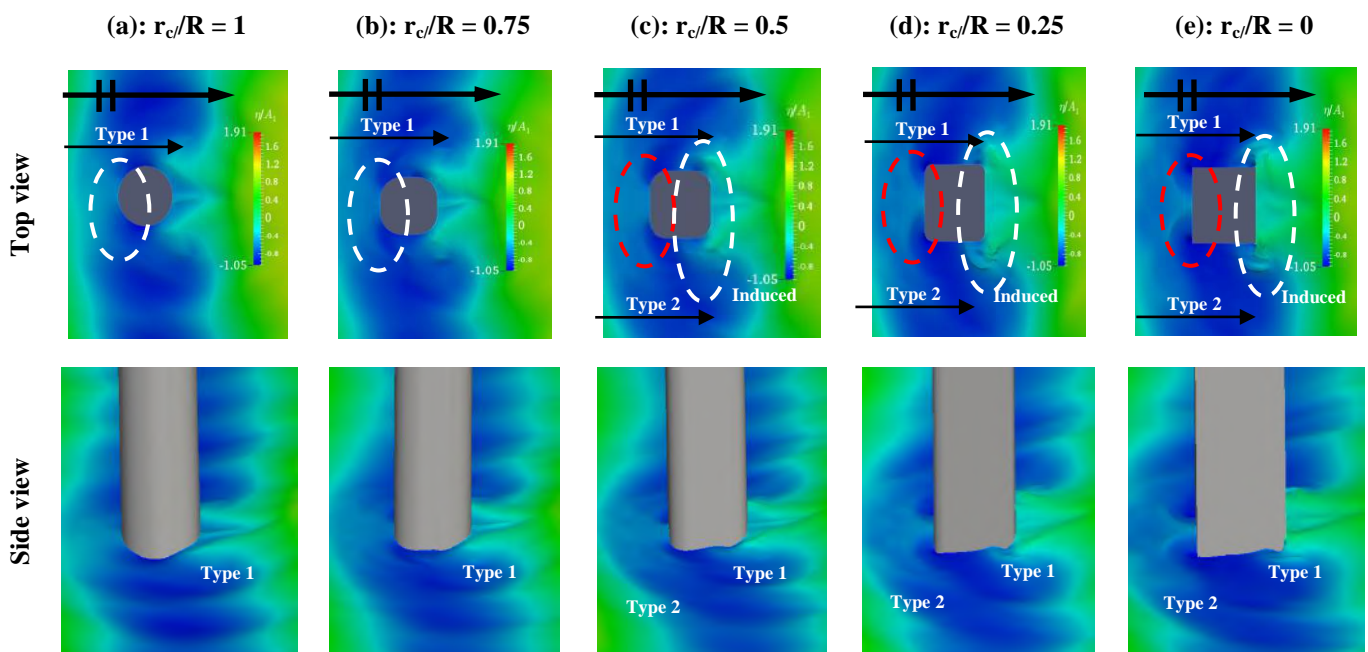


Fig 4.28. Spatial contours of the free surface elevation around the cylinder under wave condition of $(T=7s, H/L=1/16)$, with the phase between the arrival of the wave trough and zero up crossing at the front point

For mean value, primarily, systematic change in value is observed, see Fig.4.30 (a). Reducing the corner ratio, there is an increment which is related to higher run-up and also the occurrence of the second run-up at front of the cylinder, see Fig.4.28. On the other hand, reduction of wave run-up at back point reduces the mean value at this point. In the case of shoulder point, the stronger wave-wave interaction causes negative peak value for the case of ($r_c/R=1$) and for the back corner point, strong interaction with induced edge waves leads in larger negative mean value. The 4th harmonic trend is the same for all cases, see Fig.4.30 (e). It was explained in section 4.2 that for the cylinder with circular cross-section under short incident waves, nonlinearity is notable at backward half of the cylinder. However, reducing the corner ration, there is a considerable reduction in 4th harmonics. This suggests that the nonlinearity of wave field around the cylinder for the cases that corner effect is important, involves at least 3rd harmonics which is evident in all wave probes rather than back point and mainly the corner points.

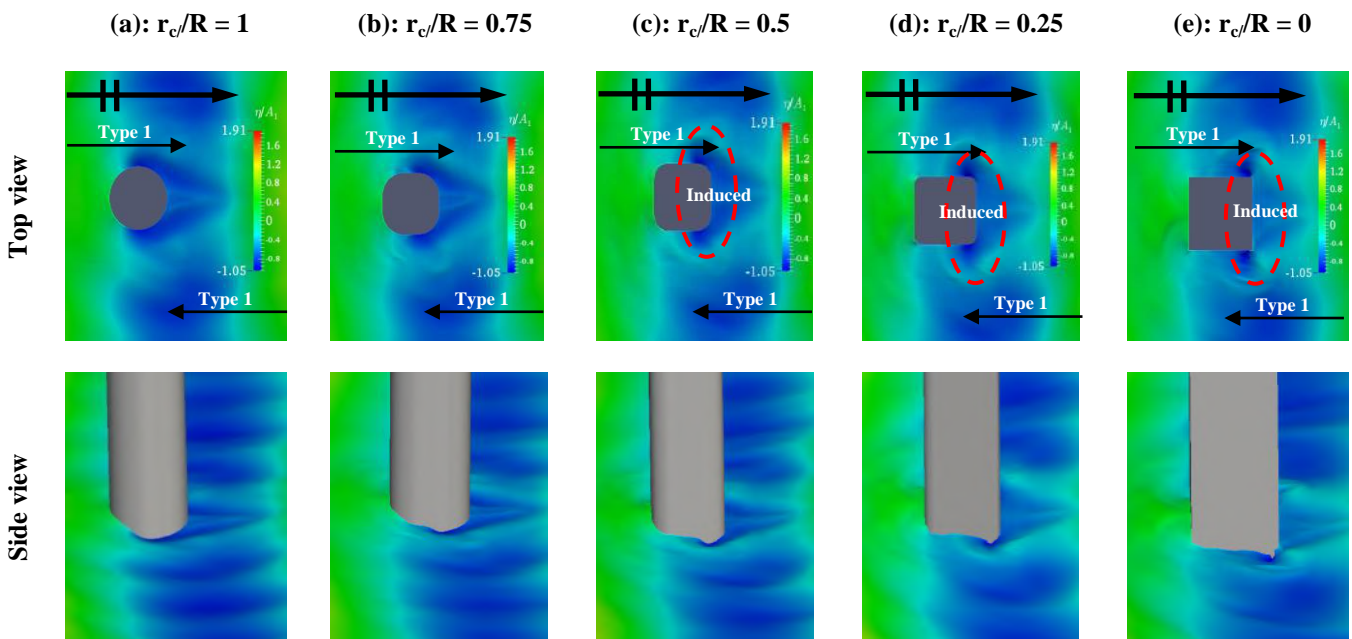


Fig 4.29. Spatial contours of the free surface elevation around the cylinder under wave condition of ($T=7s$, $H/L=1/16$), with the arrival of wave zero up crossing at the front point

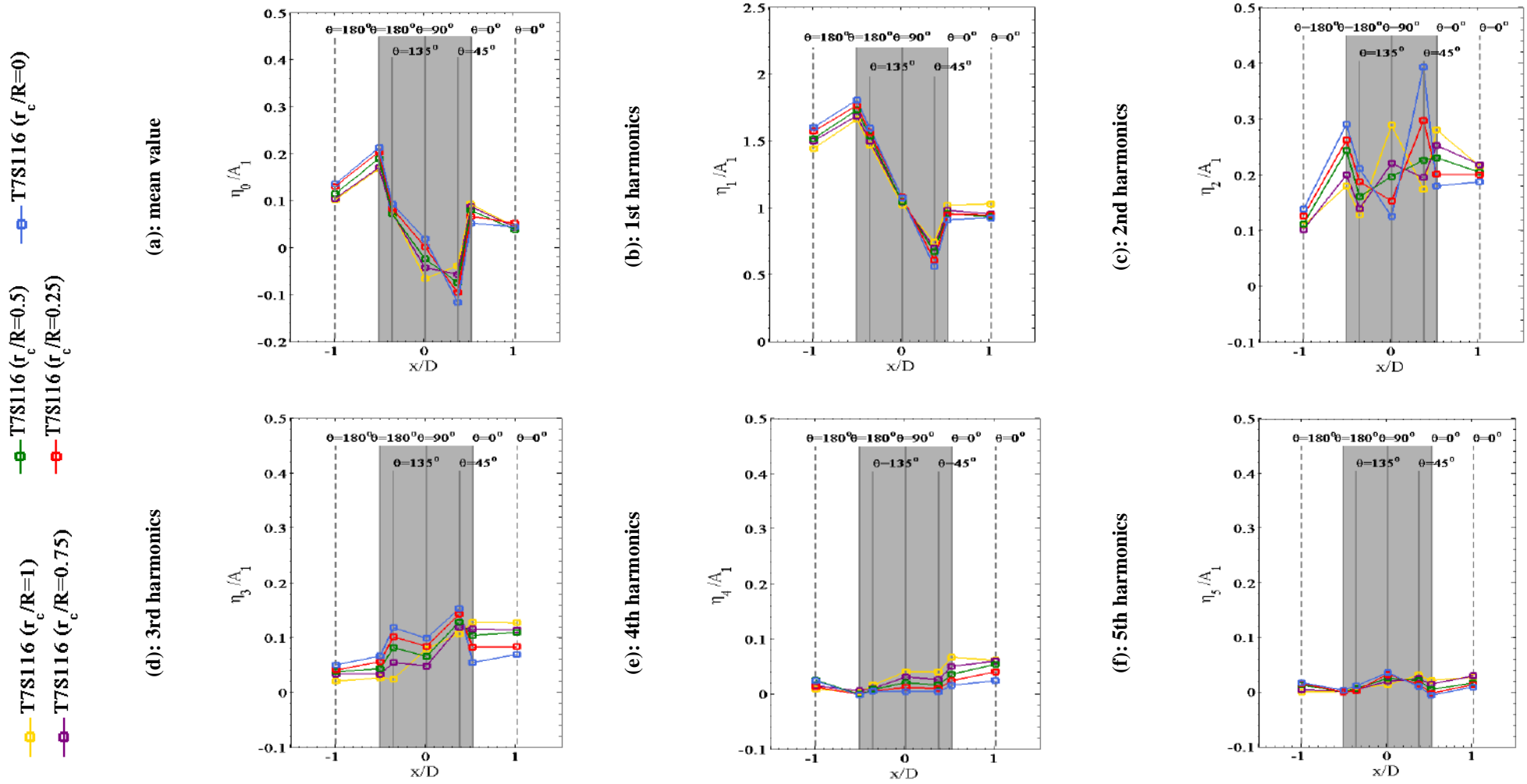


Fig 4.30. Comparison of mean value and harmonics of wave run-up for cross-section variation under wave condition of ($T=7s$, $H/L=1/16$)
 (vertical solid line ($r/D=0.513$) and vertical dash line ($r/D=1.0$))

Chapter 5

Conclusion Remarks and Future work

5.1 Conclusion

In this work, with regard to the benchmark experiment provided by ITTC (OEC) [2013], the physics of nonlinear wave scattering and wave run-up around a single fixed cylinder was studied. The physics of the problem involved in the interaction of a vertical surface piercing cylinder with surface gravity, regular and non-breaking incident waves which are propagating over a flat bed in an unbounded domain in deep water. The analysis was performed with two numerical approaches using Navier–Stokes model and Potential-flow model. A grid-space and time step refinement study were carried out to find optimum mesh arrangement that can correctly represent the wave field around the cylinder. It was found the mesh-setup B is a fair choice that can provide sufficiently satisfactory results for both wave elevation and wave loads. Similarly, it was found that the mesh resolution by mesh set-up of B3Fs3 seems sufficient for the potential-flow model. For validation purpose, a comparison with experimental data which was provided by ITTC (OEC) [2013] was performed. A good agreement under small and moderate steep incident waves of ($H/L=1/30$, $1/16$) for both short and long wave was obtained for Navier–Stokes model, while in the case of Potential-flow model, there is a small difference between numerical calculations and experiments just for simulations under small steepness incident waves of ($H/L=1/30$).

Taking into account the numerical simulation of the physical mechanism of wave scattering around the cylinder by main approach of Navier–Stokes model, the first part of the thesis was related to the investigation of the importance of the aforementioned high-frequency wave scattering and also lateral edge waves on nonlinear wave field and also inline wave force over a range of wave steepnesses and wavelengths. Then the Influence of potential flow, viscous and turbulence effects on wave run-up was explored. Afterward, in the

second part of the thesis, the effects of the change in cylinder submerged geometry and finally, change in cross-section on the wave field around the cylinder was studied.

Study the effect of a change in wavelength and wave steepness, generally, it was noticed that the scattered wave field around the cylinder involves in high harmonic wave amplification. The numerical results of spatial contour and harmonic components of wave evolution around the cylinder, in general, reveal that interaction of wave scattering Type2 in combination with edge waves with both cylinder and incident wave, contribute more to the nonlinearity of wave run-up around the cylinder. The effect wave scattering Type1 is more evident in 1st harmonics. It was also concluded that the extension that the lateral edge waves can travel around the cylinder in upstream direction is associated with (a): the local flow energy at back of the cylinder, (b): the amount of edge wave energy reduction during interaction with cylinder circumference and incident wave, (c): the incident wavelength or period and cylinder circumference which generally defines the propagation time around cylinder before arrival of zero-up crossing at front stagnation point. For short wave cases, there is no wave scattering Type2 for short wave case due to weak local flow at cylinder back and more edge wave energy reduction as a result of large diffraction and insufficient propagation time. On the contrary, for long wave cases, the strong local flow at cylinder back, less edge wave energy reduction due to small diffraction and sufficient propagation time provided the mentioned fully developed wave scattering Type 2 at front of the cylinder.

In section 4.1, it was shown that for the reference case of truncated, circular cylinder under wave condition of ($T=7s$, $H/L=1/16$), there are two of wave scattering Type1 at both front and back of cylinder while in this case there is just one wave scattering Type2 at the back of the cylinder. Subsequently, with regard to the change in wavelength under moderate steep wave condition, primarily, the formation of wave scattering Type2 at in front of the cylinder was observed where there are a partially and fully developed wave scattering Type2 pattern for cases of ($T=9s$) and ($T=15s$), respectively. For the occurrence of wave scattering Type2 at front of the cylinder , it was also shown that some part of the related disturbances is driven around the cylinder in a downstream direction with the arrival of wave zero up-crossing, contributing in a mound of water and partially formation of wave scattering Type2 at the back of the cylinder. The rest of the disturbances are scattered in the upstream direction where leads in wave-wave interaction. This can enhance the wave kinematics and steepen the next incoming wave and contribute considerably in the wave scattering Type1 and eventually increase the run-up height at the front point of the cylinder for long wave cases.

Systematic increasing of wavelength from short to intermediate and long waves, the 1st harmonic pattern remains constant and the amplification factor at front point reduces from 1.7 to 1.3 and finally 1.2 where all of them are important in the viewpoint of air gap design. For long wave although the increment value is small but taking into account the wave steepness of ($H/L=1/16$), see Table 3.1, the wave height is already large, therefore even this small increment can cause notable run-up at front point of the cylinder. For long wave cases, there is a weak collision of lateral edge waves at the back stagnation point of the cylinder which leads in small steep waves. This is related to small diffraction in combination with energy dissipation due to the pair of attached vortices. Varying the wavelength, strong nonlinearity was observed at the backward part in short waves and forward part of the cylinder in long waves. The nonlinearity for short wave case is more apparent for backward half of the cylinder, especially at the back stagnation point. Increasing the incident wavelength, the nonlinearity is notable at forward half of the cylinder, particularly at the front stagnation point. With regards to the harmonics higher than 1st, it was noticed that changing the incident wavelength, the wave field around the cylinder is nonlinear up to 4th harmonics.

Comparing the results for truncated (draft(1.5D)) and bottom-mounted cylinders in deepwater under short and long waves condition suggests that the physics of wave-structure interaction for the given truncated cylinder is the same as a bottom-mounted cylinder. Accordingly, increasing the draft more than (1.5D), the reflection by the underwater volume and also the vortices developing from the bottom of the truncated cylinder for both wave conditions, cannot affect the wave field and wave amplification around the cylinder during one wave cycle interaction.

In section 4.3, it was shown that increasing the incident wave steepness from small to high steep wave for both short and long wave cases, enhances the wave kinematics and maintaining the wave scattering Type1&2 pattern, results in higher and steeper run up. In addition, it was noticed that the wave diffraction number is more important than the strength of local flow at cylinder back for wave scattering Type2 formation at front point of the cylinder. Taking to account the numerical results for the second-order terms, for small steep waves ($H/L=1/30$) of both long and short waves, it was confirmed that, even the wave-wave and wave-structure interaction caused by the linear incident wave, can lead in weakly nonlinear wave amplification around the cylinder. It is shown that for short wave cases, the 1st harmonic of inline force is dominant and the higher harmonics are significantly small. Then increasing wavelength, the occurrence of the notable higher harmonic inline force

experienced by cylinder becomes more evident. The physical origins of these harmonics are associated to the secondary load cycle which is due to scattering of high-frequency waves in the upstream direction. For long waves cases, even low steep waves ($H/L=1/30$), the harmonic loading involves in at-least third harmonic where its magnitude is comparable with second-order harmonic and it increases with wave steepness.

The physics of the problem related to wave scattering and wave run-up around vertical, surface piercing cylinder generally involves in potential flow, viscous and turbulence effects. In the case of potential flow effects, according to the literature review, the linear and second-order diffraction solutions are inappropriate for accurate estimation of nonlinear wave field and wave run-up around the cylinder. The fully nonlinear potential flow model can provide a reasonably accurate solution in this study to the extension where diffraction theory is valid. Christou-[2009] using a fully nonlinear Boundary Element Method, found that the proposed wave scattering Type 1&2 appear to be in good qualitative agreement with the laboratory observations. Hence, it is verified that, primarily, the high-order potential flow effects, contribute to the formation of the wave scattering Types 1&2 and lateral edge waves. In addition, it can be concluded that the viscous fluid or rotational flow is not the basic and initial requirements for these phenomena at the free surface.

The wave field around the cylinder is turbulent due to localized wave breaking. The progressive lateral edge waves as they propagate in up or downstream direction, there is an energy and consequently vertical extension reduction. The primary cause of this is related to the potential flow effects and there is additional energy reduction which is caused by turbulence effects. Increase in wave diffraction or wave steepness number, separately or together, results in more interaction and then more edge wave energy reduction. The lateral edge waves energy reduction is more apparent in the 1st harmonic distribution of free surface elevation around the cylinder. It is observed the contribution of turbulence effects is not major for wave steepnesses of ($H/L=1/30$, $1/16$) and the edge wave reduction is more due to potential flow effects and then the diffusion term in Navier-stokes equation with only fluid viscosity can reasonably account the turbulence effects. In the case of high steep waves, ($H/L=1/10$), local wave breaking is intense and turbulence effects are important.

In another study, the influence of a change in underwater volume on the wave field surrounding the cylinder and corresponding wave run-up harmonics was investigated. Change in underwater volume as it can, primarily, affect the reflection. Comparing the

simulation results by a cylinder of Truncated1 and Truncated2 the wave scattering and also harmonic pattern are maintained. However, the reduction in the draft and consequently reflection by underwear volume for a cylinder of Truncated2 lead in the reduction of both wave elevation and corresponding harmonics at the given wave probes. On the contrary, in the case of the cylinder of Truncated1 and also increasing the draft more than $(1.5D)$, the excess reflection by underwater volume and also the developed vorticity from the cylinder bottom, cannot reach the free surface and affect the wave scattering and related wave run-up around the cylinder.

For SubStr1 in comparison to the reference2 case where they both have an identical draft, the effect of attached substructure is apparent. It was shown that the attached substructure enhances the surrounding wave field and related harmonics. Taking to account the draft of $(1.5D)$ for SubStr1, it caused small change while maintaining the trend for the mean value and first five harmonics in comparison to the reference case. The wave field around SubStr1 experiences locally shallow water due to the presence of attached substructure. Therefore as it was observed, there is a reduction in wave scattering propagation velocity which is more evident by steeper crest and flatter trough at the circular extension that is affected by attached substructure. The effect of attached substructure was also involved in wave upwelling. Following the assumption of identical diffraction number and incident wave condition, wave upwelling locally steepens the wave scattering and contribute to wave amplification around the vertical cylinder which is also accompanied by notable local wave breaking around the cylinder. In the case of SubStr2, the small reflection due to a small draft of the vertical cylinder was augmented by the wave upwelling. Thus, it caused significant enhancement by wave scattering and run-up and also corresponding harmonics. For SubStr2, the collision of lateral edge waves at back stagnation point in combination with wave upwelling resulted in considerably strong local flow and higher and steeper run-up. It was mentioned that for reference case, nonlinearity is more notable at half backward part while in the case of SubStr2, the nonlinearity at front stagnation point was also significant. This was related to the occurrence of the second run-up at this point in the form of the wave scattering Type1. This run-up was caused by the interaction of some point about the incident wave trough and the attached substructure.

The last objective was to study the influence of a change in cross-section (corner-ratio) on the wave scattering and wave amplification around the cylinder and also corresponding harmonics. Systematic reduction of corner ratio, it resulted in larger diffraction. Accordingly,

the edge waves traveling experienced more energy reduction. Changing the cross-section from circular to square with sharp corners, the presence and influence of corner on the wave field around the cylinder became more evident. Corner effect is related to the formation of induced edge waves which are also accompanied by developing attached vortices. As it was observed, the maximum run-up height was enhanced following the systematic reduction of corner ratio. This increment may be related to the number of stagnation points at front of the cylinder which increases as corner ratio reduces. However, changing the cross-section from circular to square with sharp corners, there was a notable reduction in both run-up height and steepness at the back of the cylinder. It was observed that the interaction of negative horizontal velocity, at cylinder back, initiated wave scattering Type1 for all given cases. In the same way, the interaction of positive vertical velocity following the passage of wave trough initiated wave scattering Type1 at front of the cylinder for all given cases. In the front of the cylinder for cases related to $(r_c/R = 0.5)$, $(r_c/R = 0.25)$ and $(r_c/R = 0)$ occurrence of developed wave scattering Type2 was observed. This related to the run-up due to the collision of induced edge waves at some point between incident wave phases of the trough and zero-up crossing by at cylinder front. As the corner effect becomes important, considerable 2nd and 3rd harmonics were observed at both back corner and front corner points. The harmonic values for the back corner point were higher. It was also shown that the nonlinearity of wave field around the cylinder for the cases that corner effect is important, involves up to 3rd harmonics.

5.2- Future work

In this work, the effect of different wave condition on the wave field around a single cylinder was studied. The same analysis can be performed with the addition of current with various values and direction and also wave-current interaction, to see how the wave scattering and also wave amplification around the cylinder is affected. The edge waves, primarily, was observed during vertical oscillation of a cylinder in still water or in the case of passage of steep waves by fixed vertical and surface piercing cylinders. Therefore It can be interesting to investigate the effects of wave/current and their interaction on the wave field around a cylinder with heave motion. In another study, the effect of adjacent cylinders on the wave scattering and nonlinearity around the objective cylinder in different numbers, layouts, and leg spacing can be investigated. It was shown that there is the disturbance which scattered in downstream from the back of the cylinder. If there is two cylinder arrangement in tandem, this disturbance may contribute to wave run-up height and steepness of the second cylinder through affecting the incident wave steepness reaching that cylinder.

Chapter 6

Bibliography

- [1] Alfonsi G., 2015. Numerical simulations of wave-induced flow fields around the large-diameter surface-piercing vertical circular cylinder. *Computation*, vol. 3 (3), pp. 386-426.
- [2] Brackbill J.U., Kothe D.B., and Zemach, C. (1992) A Continuum Method for Modeling Surface Tension. *JOURNAL OF COMPUTATIONAL PHYSICS*.
- [3] Buchmann, B., Skourup, J., Cheung, K., 1997. Run-up on a Structure Due to Waves and Current. *Proceeding of the Seventh International Offshore and Polar Engineering Conference*.
- [4] Buchmann, B., Ferrant, P., Skourup, J., 1998. Run-up on a body in waves and current, fully non-linear and finite order calculations. *13th International Workshop on Water Waves and Floating Bodies 1*, pp. 9–1
- [5] Bai, W., Eatock Taylor, R., 2007. Numerical simulation of fully nonlinear regular and focused wave diffraction around a vertical cylinder using domain decomposition. *Appl. Ocean Res.* 29, 55–71.
- [6] Berberović, E., van Hinsberg, N.P., Jakirlić, S., Roisman, I.V., Tropea, C., 2009. Drop impact onto a liquid layer of finite thickness: dynamics of the cavity evolution. *Phys. Rev. E* 79, 1–13.
- [7] Bøckmann A, Pâkozdi C, Kristiansen T, Jang H, Kim J. An experimental and computational development of a benchmark solution for the validation of numerical wave tanks. In: *Proc ASME 33rd Int Conf Ocean*. 2014
- [8] Bihs H., Alagan Chella M., Kamath A., Arntsen Ø.A. (2017) Numerical Investigation of Focused Waves and their Interaction with a Vertical Cylinder using REEF3D, *Journal of Offshore Mechanics and Arctic Engineering*, Vol. 139, Issue 4.
- [9] Chakrabarti, S. K. 1987. *Hydrodynamics of Offshore Structures*. Computational Mechanics, Southampton, UK.
- [10] Chaplin, J. R., Rainey, R. C. T. & Yemm, R. W. 1997. The ringing of a vertical cylinder in waves. *Journal of Fluid Mechanics*, 250: 119{147}.

- [11] Chaplin, J. R., Rainey, R. C. T. & Retzler, C. H. 1999. Waves generated by vertical cylinder moving in still water. Proc. 14th Intl. Workshop on Water Waves and Floating Bodies, University of Michigan, April 11-14, pages 21{24}.
- [12] Chaplin, J. R. 2001. The bow wave of a vertical surface piercing cylinder in steady current. Proc. 16th Intl. Workshop on Water Waves and Floating Bodies pages 13{16}.
- [13] Chen, L. F., Zang, J., Hillis, A. J., Morgan, G. C. J., and Plummer, A. R., 2014. "Numerical investigation of wave-structure interaction using OpenFOAM". Ocean Engineering, 88, pp. 91-109.
- [14] Cao, H. J., Wan, D. C. (2017) Benchmark computations of wave run-up on a single cylinder and four cylinders by the naoe-FOAM-SJTU solver, Applied Ocean Research. 65, 327-337.
- [15] Christou M, 2009, Fully Nonlinear Computations of Waves and Wave-structure Interaction. Thesis dissertation, Imperial College London.
- [16] De Vos, L., Frigaard, P., De Rouck, J., 2007. Wave run-up on cylindrical and cone-shaped foundations for offshore wind turbines. Coast. Eng. 54, 17-29
- [17] Danmeier DG, Seah RKM, Finnigan T, Roddier D, Aubault A, Vache M, et al. Validation of wave run-up calculation methods for a gravity-based structure. In: Proc ASME 27th Int Conf Offshore Mech and Arctic Eng. 2008.
- [18] Devolder, B., Rauwoens, P., Troch, P., 2017. Application of a buoyancy-modified $k-\omega$ SST turbulence model to simulate wave run-up around a monopile subjected to regular waves using OpenFOAM. Coastal Engineering 125 (2017) 81-94.
- [19] Dianat, M., M. Skarysz, and A. Garmory, A Coupled Level Set and Volume of a Fluid method for automotive exterior water management applications. International Journal of Multiphase Flow, 2017. 91: p. 19 -38.
- [20] Havelock TH. The pressure of water waves upon a fixed obstacle. Proc R Soc Lond A 1940;175:409-21.
- [21] Higuera, P., Lara, J.L., Losada, I.J., 2013a. Realistic wave generation and active wave absorption for Navier-Stokes models application to OpenFOAM. Coastal Eng. 71, 102-118.
- [22] Hirt, C.W., Nichols, B.D., 1981. Volume of fluid (VOF) method for the dynamics of free boundaries. J. Comput. Phys. 39 (1), 201-225.
- [23] Hirsch, C. (1991). Numerical computation of internal and external flows: John Wiley & Sons.
- [24] Isaacson, M.d.S.Q., Cheung, K., 1993. The time-domain solution for wave-current interaction with a two-dimensional body. Applied Ocean research 15 (1), 39-52.
- [25] Isaacson, M.d.S.Q., Cheung, K., 1994. Correction factors for non-linear run-up and wave force on a large cylinder. Canadian Journal of Civil Engineering 21, 762-769.
- [26] ITTC OEC Workshop on VIV and Wave Run-up held in Nantes, France October 17-18, 2013.
- [27] Jasak, H. (1996). Error analysis and estimation for the finite volume method with applications to fluid flows, Ph.D. thesis. Imperial College of Science, Technology, and Medicine, UK.

- [28] Jacobsen, N.G., Fuhrman, D.R., Fredsøe, J., 2012. A wave generation toolbox for the open-source CFD library: OpenFoams. *Int. J. Numer. Methods Fluids* 70, 1073–1088.
- [29] Kriebel, D., 1990. Nonlinear wave diffraction by the vertical circular cylinder. Part 1: Diffraction theory. *Ocean Engineering* 17, 345–377.
- [30] Kriebel, D., 1992. Non-linear wave interaction with a vertical circular cylinder. Part II: wave run-up. *Ocean Engineering* 19 (1), 75–99.
- [31] Kristiansen T, Baarholm RJ, Stansberg CT. Validation of second-order analysis in predicting diffracted wave elevation around a vertical cylinder. *Proceedings of the 14th ISOPE conference, Toulon, France; 2004.*
- [32] Kim, J., Jaiman, R., Cosgrove, S., O’Sullivan, J., 2011. Numerical wave tank analysis of wave run-up on a truncated vertical cylinder. In *ASME 30th International Conference on Ocean, Offshore and Arctic Engineering (OMAE), Rotterdam, The Netherlands, 2011.*
- [33] Kamath A., Alagan Chella M., Bihs H., Arntsen Ø.A. (2015). CFD Investigations of Wave Interaction with a Pair of Large Tandem Cylinders, *Ocean Engineering*, Vol. 108, pp. 738-748,
- [34] Kamath A., Bihs H., Alagan Chella M., Arntsen Ø.A. (2016). Upstream and Downstream Cylinder Influence on the Hydrodynamics of a Four Cylinder Group, *Journal of Waterway, Port, Coastal, and Ocean Engineering*, Vol. 142 (4).
- [35] Longuet-Higgins MS, Stewart RW. 1960 Changes in the form of short gravity waves on long waves and tidal currents. *J. Fluid Mech.* 8, 565–583.
- [36] Le Mehaute, B., 1976. *An Introduction to Hydrodynamics and Water Waves.* Springer, Singapore.
- [37] Lin, Y., Chen, J., Lu, P., 2017. A CFD model for simulating wave run-ups and wave loads in case of different wind turbine foundations influenced by nonlinear waves. *Ocean Engineering* 129 (2017) 428–440.
- [38] MacCamy RC, Fuchs RA. Wave forces on piles: A diffraction theory. *Beach Erosion Board Office of the Chief Engineers, Department of the Army, Technical Memorandum no. 69; 1954* 1–17
- [39] Muzaferija, s., Peric, m., 1997. computation of free-surface flows using the finite-volume method and moving grids. *numerical heat transfer, part b: fundamentals. volume 32, 1997 - issue 4*
- [40] Morris-Thomas MT. An investigation into wave run-up on a vertical surface piercing cylinder in monochromatic waves, Ph.D. Thesis, The University of Western Australia; 2003.
- [41] Morris-Thomas MT, Thiagarajan KP. The run-up on a cylinder in progressive surface gravity waves: harmonic components. *Appl Ocean Res* 2004;26:98–113.
- [42] Niedzwecki JM, Duggal AS. Wave runup and forces on cylinders in regular and random waves. *J Waterway, Port, Coastal, Ocean Eng* 1992;118(6):615–34.

- [43] Nielsen FG. Comparative study on airgap under floating platforms and run-up along platform columns. *J Mar Struct* 2003;16:97–134.
- [44] Ning, D. Z., Zang, J., Liu, S. X., Eatock Taylor, R., Teng, B., and Taylor, P. H., 2009. “Free-surface evolution and wave kinematics for nonlinear uni-directional focused wave groups”. *Ocean Engineering*, 36, pp. 1226—1243.
- [45] OpenCFD Ltd (2012). OpenFOAM: The open source computational fluid dynamics (CFD) toolbox. <https://openfoam.org/release/2-2-0/>
- [46] OpenCFD Ltd (2014). OpenFOAM: The open source computational fluid dynamics (CFD) toolbox. <https://openfoam.org/release/2-2-0/>
- [47] Patankar, S.V. Numerical heat transfer and fluid flow. Hemisphere Publishing Corporation, Washington, DC, 1980.
- [48] Peng, A., Wellens, P., Raaijmakers, T., 2012. 3-D numerical modeling of wave run-up on monopiles. In *Proceeding of 31st International Conference on Ocean, Offshore and Arctic Engineering (OMAE)*, Rio de Janeiro, Brazil
- [49] Paulsen, B.T., 2013. Efficient computations of wave loads on offshore structures. Ph.d. The Technical University of Denmark.
- [50] Paulsen, B.T., Bredmose, H., Bingham, H.B., Jacobsen, N.G., 2014. The forcing of a bottom mounted circular cylinder by steep regular water waves at finite depth, *J. Fluid Mech.* (2014) vol. 755, pp. 1–34.
- [51] Rainey, R.C.T., 1997. Violent surface motions around vertical cylinders in large, steep waves - is this the result of the step change in relative acceleration? *Proc. 12th Intl. Workshop on Water Waves and Floating Bodies*, Marseilles, France, pages 215{218}.
- [52] Roache, P.J., 1998. *Verification and Validation in Computational Science and Engineering*. Hermosa Publishers, Albuquerque.
- [53] Retzler, C. H., Chaplin, J. R. & Rainey, R. C. T. 2000. The transient motion of a vertical cylinder: Measurements and computations of the free-surface. *Proceedings of the Fifteenth International Workshop on Water Waves and Floating Bodies*, University of Michigan, April 11-14, pages 154{157}.
- [54] Rusche, H. (2002), *Computational fluid dynamics of dispersed two-phase flows at high phase fractions*, Ph.D. thesis, Imperial College London (University of London).
- [55] Ramirez, J., Frigaard, P., Lykke Andersen, T., and Christensen, E., 2011. “Numerical modeling of wave run-up: regular waves”. In *Twenty-first International Offshore and Polar Engineering Conference: ISOPE*.
- [56] Ramirez, J., Frigaard, P., Lykke Andersen, T., De Vos, L., 2013. Large-scale model test investigation on wave run-up in irregular waves at slender piles. *Coast. Eng.* 72, 69–79.
- [57] Repalle, Thiagarajan, Morris-Thomas. CFD simulation of wave run-up on a spar cylinder 16th Australasian Fluid Mechanics Conference, Crown Plaza, Gold Coast, Australia (2007), pp. 1091-1094

- [58] Roenby J, Bredmose H, Jasak H. 2016 A computational method for sharp interface advection. *R. Soc. open sci.* 3: 160405.
- [59] Roenby J, Pedersen, R., Eltard-Larsen, B., Bredmose, H., & Jasak, H. (2017). A New Volume-Of-Fluid Method in OpenFOAM. Paper presented at VII International Conference on Computational Methods in Marine Engineering (MARINE 2017), Nantes, France.
- [60] Skjelbreia, L., Hendrickson, J..A. Fifth order gravity wave theory Proc. 7th Coastal Engng Conf., The Hague (1960), pp. 184-196.
- [61] Stern F, Wilson RV, Coleman HW, Paterson EG. A comprehensive approach to verification and validation of CFD simulations-Part 1: methodology and procedures. *ASME J Fluids Eng* 2001;123:793–802
- [62] Stansberg CT, Nielsen FG. Nonlinear wave–structure interaction on floating production systems. Proceedings of the 11th ISOPE conference, Stavanger, Norway, vol. IV; 2001. p. 363–72.
- [63] Stansberg CT, Braaten H. Nonlinear wave disturbance around a vertical circular column. Paper no. 28620. Proceedings of the 21st OMAE Conference, Oslo, Norway; 2002.
- [64] Stansberg, C.T., Kristiansen, T., 2005. Non-linear scattering of steep surface waves around vertical columns. *Appl. Ocean Res.* 27 (2), 65–80.
- [65] Swan C, Masterton S, Sheikh R, Cavalletti A. Wave forcing and wave scattering from a vertical surface-piercing cylinder. Paper no. 67158. Proceedings of the 24th OMAE conference, Halkidiki, Greece; 2005.
- [66] Sumer, b. m. & Fredsø, j. 2006 hydrodynamics around cylindrical structures. world scientific.
- [67] Swan C, Sheikh R. The interaction between steep waves and a surface piercing column. *Phil Trans R Soc A* 2015;373(2033),
- [68] Sun, L., Zang, J., Chen, L., Taylor, R. E., Taylor, P. H. (2016) Regular waves onto a truncated circular column: A comparison of experiments and simulations, *Applied Ocean Research* 59, 650-662.
- [69] Eatock Taylor R, Sincock P. Wave upwelling effects in TLP and semisubmersible structures. *Ocean Eng* 1989;16(3):281–306
- [70] Weller, H. (2002), Derivation, modeling and solution of the conditionally averaged two-phase flow equations, Tech. rep., OpenCFD Ltd.
- [71] Weller, H.G.(2008). A new approach to VOF-based interface capturing methods for incompressible and compressible flow. Technical Report TR/HGW/04, OpenCFD Ltd., 2008.
- [72] Yoon, S.-H., Kim, D.-H., Sadat-Hosseini, H., Yang, J., and Stern, F., 2016. “High-fidelity CFD simulation of wave run-up for single/multiple surface-piercing cylinders in regular head waves”. *Applied Ocean Research*, 59, pp. 687–708.